SCUOLA NORMALE SUPERIORE - PISA

Anno Accademico 2007-08

Perfezionamento in Fisica

Pisa, 13 ottobre, 2007

Quantum Phase transitions in Hubbard lattices

Candidato
Matteo Rizzi

Relatore
Prof. Rosario Fazio

0

Contents

Introduction

The quest for a complete explanation of apparently basic natural phenomena, such as heat and electric conduction, magnetism, phase transitions, is one of the most intriguing challenges in physics. Apart from detailed description of single experiments on particular samples and materials, physicists are interested in understanding the underlying microscopic mechanisms in a more general way. A satisfactory theory should explain a wide spread of phenomena avoiding, as far as possible, the introduction of *ad hoc* parameters.

Single particle properties can be studied basically in every external situation, by using the appropriate equation of motion. Since one is considering microscopic world, a quantum description is necessary. Whatever complicate is the external potential one is dealing with, the task consists in solving the Schrödinger problem, i.e. a single linear differential equation, and obtaining a wavefunction that describes all the physics. Whereas a closed analytical solution is available only in peculiar cases, nonetheless it is possible to find accurate numerical approximations. The only limiting factor is given by hardware resources.

Unfortunately the many body problem one has to tackle in describing the real world, is much more complicated. Indeed interactions couple the single particle equations and, even in classical mechanics, a general solution for the three-body problem is not available. Moreover, to describe macroscopic ensembles of (free) particles one has to introduce statistical mechanics and thermodynamics. Coming to the quantum context, a generic many-body state is described by a *global* wavefunction. *The problem to be tackled is highly non-trivial since strong correlations make it non-separable, even in*

first approximations. Furthermore, undistinguishable quantum particles have to obey (anti)symmetry requirements on the *global* wavefunction. Bosons (integer spin) must be in a symmetric superposition under permutations, whereas fermions (half-integer spin) have to be in an antisymmetric one. Even numerical simulations of such systems is an extremely hard task, since they require a number of resources (time and memory) that generally grows exponentially with the number of constituents.

Furthermore there is a wide gap between general (non ad-hoc) theoretical predictions and real experiments carried out on samples available in nature. Indeed, theoreticians make predictions on ideal toy models where all the coupling parameters are known and perfectly tunable; experimentalists have to deal with systems where the true Hamiltonian is unknown and not all the couplings values are reachable. Thus considerable efforts have always been spent towards *Hamiltonian engineering.*

Perhaps one of the first steps in this direction was the experimental implementation of a Josephson junctions array, i.e. small islands of superconducting materials arranged on a regular lattice and linked by thin oxide layers. All the couplings depend only on islands dimensions and layer thickness, though a *different sample* is necessary for each coupling chosen. These systems have been intensively studied [1] as ideal model systems to explore a wealth of classical phenomena [2, 3] such as phase transitions, frustration effects, classical vortex dynamics and chaos. One of the most spectacular result was probably the experimental observation [4, 5] of the Berezinskii-Kosterlitz-Thouless transition [6, 7]. Indeed, well below the BCS transition temperature, and in the classical limit, Josephson arrays are experimental realization of the XY model. Moreover it is quite easy to frustrate this systems by means of external magnetic fields and this opens the way to intriguing phenomena such as localization without disorder. The onset of Aharanov-Bohm cages [8], i.e. domains where particles are localized, and its influence on the Mott-Superfluid phase diagram will be analyzed in Chapters 2-3. Quantum MonteCarlo numerical techniques [9] are used, aside with analytical approaches. In particular, in Ch. 2 we focus our attention to the condensation of pairs of Cooper pairs as the basic mechanism for superfluidity. The possible existence

of a new intermediate phase between the insulator and the superconductor is one of the main results of Ch. 2. Many other aspects of the phase diagram in particular lattice geometries are examined there.

More recently, since the first experimental realizations of Bose-Einstein condensation [10, 11], quantum degenerate cold atomic gases have attracted physicists as ideal benchmark systems for theoretical quantum statistical phenomena (for a review see [12, 13]). Atomic physics experiments with quantum degenerate Bose and Fermi gases are characterized by two distinguishing features: a detailed microscopic understanding of the Hamiltonian of the systems realized in the laboratory, and a complete control of the system parameters via external fields. In particular, atoms can be trapped and their motion controlled in magnetic and optical traps, allowing, for instance, the realization of quantum gases with different dimensionality at effectively zero temperature. In addition, atoms have many internal states which can be manipulated using laser light and can be employed as a probe of the gas properties. Their collisional properties can be tuned with magnetic and optical Feshbach resonances. More recently the use of far-off-resonance optical traps, has opened the exciting possibility to study quantum magnetism by means of spinor condensates (for a review, see [14]).

In particular, as first pointed out in Ref. [15], strongly interacting systems can be realized with cold neutral atomic gases in optical lattices [16, 17, 18], i.e. periodic arrays of microtraps generated by standing wave laser light fields. This leads to Hubbard type lattice models, where atomic physics provides a whole toolbox to engineer various types of Hamiltonians for 1D, 2D and 3D Bose and Fermi systems which can be controlled by varying external field parameters in a time dependent way. In addition, atomic physics provides systematic ways of loading these lattices with atoms, offering a chance of exploring partial filling effects. This has paved the way to the simulation of complex quantum systems of condensed matter physics, such as high–T_c superconductors, Hall systems, and superfluid ^{4}He, by means of atomic systems with perfectly controllable physical parameters [19]. A prominent example is the Mott insulator-superfluid quantum phase transition with cold bosonic atoms, as first observed in the seminal experiment by I. Bloch and

collaborators [16, 17]. Cold atoms have been also successfully trapped in low-dimensional geometries. A ^{87}Rb gas has been used to realize experimentally a Tonks-Girardeau gas [20, 21]. In recent years a number of theoretical studies have addressed properties of ultra-cold atomic gases by transferring ideas and methods previously developed in the context of solid-state and many-body physics. These gaseous systems allow clean and controlled observations of many physical phenomena that are relevant in condensed matter and are believed to be relevant in astrophysical contexts (for a review on perspectives see Cirac and Zoller [22, 23, 13, 24, 25]).

In Chapter 4 of this thesis we focus our investigations on spinor bosons loaded in one-dimensional optical lattices. Numerical results obtained with a Density Matrix Renormalization Group approach [26, 27] are presented; details about our implementation of the code are given in App.B. We determined quantitatively the influence of spin interaction on the Mott-Superfluid transition, highlighting parity effects. We furthermore discussed the magnetic properties of the insulating phase with filling one, apparently closing a long debated question about it.

Not only bosons can be loaded in optical lattices but also fermionic atoms, mainly via sympathetic cooling [28]. The preparation of two-component Fermi gases in a quasi-$1D$ geometry [29] provides a unique possibility to experimentally study phenomena predicted a long time ago for electrons in $1D$. Spin-charge separation in Luttinger liquids is a paradigmatic example [30]. In Chapter 5, we study fermions with spin degree of freedom and attractive on-site interactions. The spin-spin interactions in a Fermi-Hubbard model may generate an antiparallel-spin pairing as in a conventional superconductor, although long-range phase coherence is absent in a $1D$ system (Luther-Emery liquid). Moreover, if the fermionic population is polarized, the existence of two distinct Fermi surfaces will lead to the creation of pairs with a momentum equal to the mutual distance between them (i.e. $\mathbf{k}$ and $-\mathbf{k}+\mathbf{q}$, $\mathbf{q} = \Delta\mathbf{k_F}$). Such a phase, where the superconducting order parameter is spatially-dependent, is known as Fulde-Ferrel-Larkin-Ovchivnikov (FFLO) state.

The possibility of simultaneously cooling bosonic and fermionic atoms

opens up the fascinating possibility of studying the interplay between different statistics. Such mixed systems occur frequently in nature, for example each time bosons act as force carriers between fermions. However investigations in real condensed matter systems (e.g. $^3He -^4 He$ mixtures) have always been very difficult due to the complicated nature of interactions. Experimental realizations of mixtures in ultracold gases [31, 32, 33, 34] gave almost unrestricted access to all parameters and thus greatly excited the community. In Chapter 6 a phase diagram for bose-fermi mixtures away from commensurate filling is drawn. According to mean-field the two species can either be mixed (conserving their individual characters) or phase separated when interactions are too strong. Our results highlight the existence of a novel intermediate phase where individual species can not be addressed but only composite particles do make sense.

More generally, we expect that cold atoms in optical lattices will be employed in the coming years as a general quantum simulator of lattice models. This would permit an experimental insight into phase diagrams for certain classes of (toy) models (such as high-T_c superconductivity) and for parameter regimes, where no rigorous theoretical approaches exist. In addition, new theoretical challenges appear in this context, e.g. the study of time-dependent phenomena. Besides the condensed matter aspects, the engineered Hubbard models have direct application in quantum computing, where the controlled interactions can be used to create entanglement with high fidelity [35].

Chapter 1

The Hubbard Model

This first Chapter is devoted to the introduction of the Hubbard models (HM), which are one of the simplest but more powerful theoretical tools to describe all the crucial features of many-body systems. Indeed, these lattice models take into account all the basic processes: localization, hopping and correlations.

A lattice can be schematized as a sequence of potential wells labelled by i, and **localization** is related to the single-particle bound states in such wells. The corresponding contribution in the many body Hamiltonian is thus proportional to the site population, i.e. it is a sort of position dependent chemical potential ε_i:

$$\mathcal{H}_\varepsilon = \sum_i \varepsilon_i \widehat{n}_i \tag{1.1}$$

On the other hand, the kinetic energy allows the bosons to delocalize. In the lattice Hamiltonian language it corresponds to hopping contributions that destroy a particle on site i and create another one on site j. The leading term in the tight-binding approximation (useful for most of the physical situations) is the nearest neighbour contribution. Indeed, hopping coefficients t_{ij} are proportional to the overlap between wavefunctions on sites i and j and thus exponentially smaller with growing distance $|i-j|$. The kinetic term always preserves internal degrees of freedom (labelled by σ), and thus can be written

(here c could be b for bosons or f for fermions) as:

$$\mathcal{H}_t = -\frac{t}{2}\sum_{<ij>}\sum_{\sigma}(\widehat{c}^{\dagger}_{i,\sigma}\,\widehat{c}_{j,\sigma} + \widehat{c}^{\dagger}_{j,\sigma}\,\widehat{c}_{i,\sigma}) \tag{1.2}$$

Finally, many body systems are characterized by correlations and interaction between particles. The lowest order term is the on-site two-body interaction, $\widehat{c}^{\dagger}_{i,\sigma}\,\widehat{c}^{\dagger}_{i,\sigma'}\,\widehat{c}_{i,\sigma'}\,\widehat{c}_{i,\sigma}$ that will read bilinear in the local populations. The explicit form will depend on the particles' statistics considered, see Sec. 1.2 - 1.3.

$$\mathcal{H}_U = \frac{1}{2}\sum_{i}\sum_{\sigma,\sigma'} U_{\sigma,\sigma'}\,\widehat{c}^{\dagger}_{i,\sigma}\,\widehat{c}^{\dagger}_{i,\sigma'}\,\widehat{c}_{i,\sigma'}\,\widehat{c}_{i,\sigma} \tag{1.3}$$

The coefficient U is related to the appropriate microscopic model for interactions. In the case of long-range interactions, this term will be generalized to a non local one $U_{i,j}\,\widehat{n}_i\,\widehat{n}_j$.

The Bose-Hubbard model [36] has been used to study a variety of strongly correlated systems as superconducting films [37], Josephson junction arrays [1] and optical lattices [15]. It predicts the existence of a zero-temperature phase transition from an insulating to a superfluid state which, by now, has received ample experimental confirmation [16, 17].

In the following sections we will examine first some experimental implementations, showing how things can be effectively reduced to an Hubbard-like description (Sec. 1.1).Subsequently we resume briefly some of the most interesting phenomena predicted by the HMs in both bosonic (Sec. 1.2) and fermionic (1.3) systems. Original results as well as more detailed description of such a phenomenology is demanded to Chapters 2 - 6.

1.1 Experimental implementation

Physicists usually exploit Hubbard-like models as toy models to catch the basic physics of a complex system existent in nature (as is usually done in solid state physics for metals, crystals, etc.) where the Hubbard parameters are not known (and moreover, not easily tunable). On the contrary, we stress the point that both of the proposed systems are artificially made and have

few and easily tunable parameters. This makes them ideal systems to check experimentally theoretical predictions.

The *first* system is based on Josephson junctions arrays (JJA), i.e. on systems where small islands of superconducting material constitute the lattice sites and the links are made of thin oxide layers. All the couplings depend only on islands dimensions and layer thickness, though a *different sample* is necessary for each coupling chosen. In Sec. 1.1.1 we discuss also a slightly different version of the model that is more appropriate to high occupation numbers.

Cold atoms in optical lattices are the *second* proposed systems. They are particularly fascinating for theoretical physicists because they are almost completely free of disorder, and the couplings parameters are tunable *on the same sample* by means only of the laser intensity. Recently, Feshbach resonances have opened also the possibility of tuning even the inter-particle interactions.

1.1.1 Josephson junctions and Quantum Phase model

A Josephson junction is made up by two superconductive electrodes connected by a weak link, which can be a constriction of the superconductive material (S-c-S) or a thin layer of a normal metal (S-N-S) or an insulator (S-I-S). Experiments on JJAs are performed well below the BCS critical temperature and thus each island is in the superconducting state. Since all islands are assumed to be identical, the only important dynamical variable is the phase φ_i of the superconducting order parameter in each island. The local value of the phase is not observable, but the difference across a link leads to the well known Josephson effect. It consists on a supercurrent

$$I_s = I_c \sin(\varphi_{1,2})$$

that flows between electrodes without potential difference $V_{1,2} = 0$, up to a critical value I_c. If one thinks about putting such junctions in a lattice, novel effects can come from the electrostatic energy that tries to localize particles and have the smoothest charge distribution.

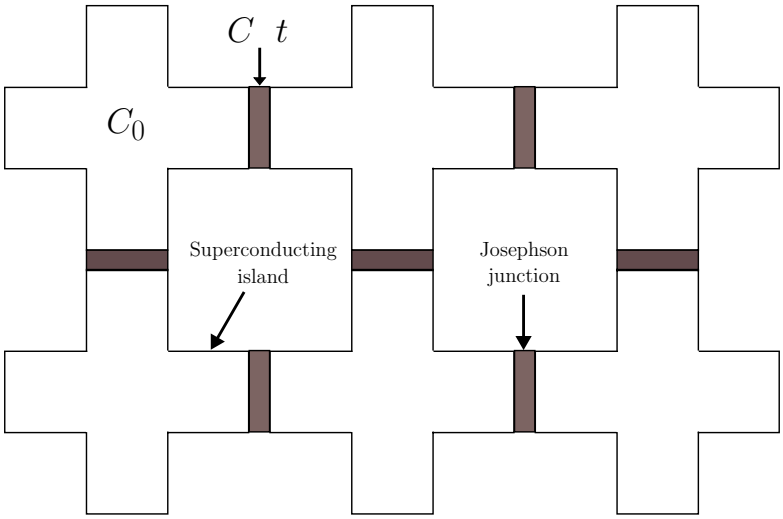

Figure 1.1: Sketch of a Josephson junction array. All the important parameters are highlighted.

Since the first realization of Josephson junction arrays [38, 39], these systems have been intensively studied as ideal model systems to explore a wealth of classical phenomena [2, 3] such as phase transitions, frustration effects, classical vortex dynamics and chaos. One of the most spectacular result was probably the experimental observation [4, 5] of the Berezinskii-Kosterlitz-Thouless transition (BKT) [6, 7]. Indeed, well below the BCS transition temperature, and in the classical limit, JJAs are experimental realization of the XY model. For sufficiently small (submicron) and highly resistive (normal state resistance $R_N > R_Q = h/4e^2$) junctions quantum effect start to play an important role. In addition to the Josephson energy, which controls the Cooper pair tunnelling between neighbouring grains, also the charging energy $e^2/2C$ (C is the geometrical junction capacitance) becomes important.

The Hamiltonian of a JJA will consist of two parts that accounts for electrostatic interaction between Cooper pairs and for the Josephson tunnelling between neighbouring islands, respectively.
The charging energy is proportional to the inverse capacitance matrix of the lattice. It can be evaluated by assuming that each island has a capacitance to

the ground C_0 and each junction a geometrical capacitance C (see Fig.1.1):

$$\mathcal{U} = 4e^2\mathcal{C}^{-1} \qquad \mathcal{C} = (C_0 + z_i C)\,\mathbb{I} - C\,\mathcal{T}\ . \tag{1.4}$$

where $\mathcal{T}$ is the connection matrix. We remark that both the connection and the capacitance matrices depend only on the distance between the cells (and on the eventual base index of both sites). An estimate of the range of the electrostatic interaction is given by [40] $\lambda \approx \sqrt{C/C_0}$. The charge frustration n_0, that we assume to be uniform, can be induced by an external (uniform) gate voltage $\mu = V_0 = n_0 8U_0$, since $\sum_j C_{i,j} = C_0\ \forall i$ and thus $4e^2 \sum_j C^{-1}_{i,j} = 4e^2/C_0 = 8U_0\ \forall i$.
On the other hand, the free energy stored in a junction is proportional to the phase difference $\varphi_{i,j}$ across it. Indeed, recalling that the phase evolves with the potential difference according to

$$\mathrm{d}\varphi_{i,j}/\mathrm{d}t = (2\pi c/\Phi_0)\,V_{i,j}\ ,$$

the work needed to change it by an external source is

$$F = \int I_s\,V\,\mathrm{d}t \propto \int \sin(\varphi_{i,j})\mathrm{d}\varphi_{i,j}\ \sim \cos(\varphi_i - \varphi_j - A_{i,j})\ . \tag{1.5}$$

The shift $A_{i,j}$ in the phase difference is given by the integral of the external gauge potential across the link. The intensity of the coupling $\tilde{t}$ is related to microscopic description by $\tilde{t} = (I_c\,\Phi_0)/(2\pi\,c)$ where the critical current of the junction is given by the Ambegaokar-Baratoff formula $I_c(T) = (\pi\Delta(T)\tanh(\Delta(T)/(2k_BT)))/(2eR_n)$. The normal resistance R_n and the gap value $\Delta(T)$ are material dependent.

Putting together the expressions in Eqs. (1.4-1.5), one obtains the so-called Quantum Phase Model:

$$\begin{aligned}\mathcal{H} \ &= \ \frac{1}{2}\sum_{ij}(n_i - n_0)\,U_{i,j}\,(n_j - n_0) \\ &\quad -\tilde{t}\sum_{i,j} T_{i,j}\,\cos(\varphi_i - \varphi_j - A_{i,j})\ .\end{aligned} \tag{1.6}$$

Such an Hamiltonian can be read as the large occupation number expansion of a Bose Hubbard Hamiltonian. Indeed, Eq. (1.6) can be rewritten as

$$\mathcal{H} = \frac{1}{2}\sum_{ij} n_i\,U_{i,j}\,n_j - \mu\sum_i n_i - \overline{n}\,t\sum_{<i,j>}\cos(\varphi_i - \varphi_j - A_{i,j})\ .$$

where $\overline{n}$ is the average occupation number, and n_i assumes the meaning of extra Cooper pairs number on island i. The correspondence between the Josephson term and the standard hopping one of Eq. (1.2), is constructed by introducing the phase operator $\widehat{\varphi}_i$ in approximating the boson annihilation operator $\widehat{b}_i \simeq \sqrt{\overline{n}}\ \exp[-\imath\widehat{\varphi}_i]$. The density n_i and phase φ_i operators are canonically conjugate on each site

$$\left[\widehat{n}_i, e^{\pm\imath\widehat{\varphi}_j}\right] = \pm\delta_{i,j}\, e^{\pm\imath\widehat{\varphi}_i}\,. \tag{1.7}$$

1.1.2 Cold atoms in optical lattices

Almost all interesting many body effects are, more or less directly, consequences of the fundamental statistics to which elementary particles must obey. These effects are the more evident the lower is the temperature under investigation: thermal effects becomes irrelevant, and ground-state properties make the game. *On the other hand, cooling down samples becomes more and more difficult the lower is T since scattering processes are suppressed by it.*

Among the ultracold phenomena, Bose-Einstein condensation has always played a preeminent role since its original prediction in the Twenties. It consists on the collapse of a boson gas into a macroscopic quantum state when cooled under a critical temperature depending on the density. A useful interpretation relies on the quantum interference between particles when the deBroglie thermal wavelength is comparable to the mean interatomic distance in the sample. The quest for experimental evidence of the BEC has culminated in 1995 when C.E. Wieman and E.A. Cornell claimed for condensation in a sample of ^{87}Rb magnetically confined and W.Ketterle did for ^{23}Na too [10, 11]. High purity and easy optical detection of the samples have made BE condensates ideal candidates to investigate fundamental issues on interacting quantum systems (see e.g. the reviews [13, 12]).

The sophisticated cooling and trapping techniques developed in such a quest have paved the way to what can be considered at all levels a new field of physics, i.e. the study of ultracold atomic gases properties. Even fermions can be part of the game, due to the possibility of sympathetic cooling (and

other experimental tools). Moreover a rich variety of trapping configurations, both of magnetic and optical nature, is available in the laboratories. Finally, exploiting the existence of Feshbach resonances, tunability of the scattering length has become reality. What is open in front of both theorists and experimentalists is an intriguing playground that widen from dilute spinless bosons to boson-fermion mixtures, from BEC-BCS crossover to exotic superfluid phases in polarized fermionic samples.

Recently, usage of a standing wave from couples of counterpropagating (and blue detuned) laser beams has given the possibility of creating an optical lattice with several wells inside an harmonic trap [41, 42, 43, 44]. This opens new perspectives in the study of discrete systems [15], being a noteworthy advantage of atomic gases over condensed matter (such as solids or liquids) the fact that experimental parameters are highly controllable. The experimental test of the superconductor-insulator transition [16, 17] (see Sec.1.2) has probably been the most spectacular example of these novel possibilities. Atoms can be enhanced well into regimes of strong correlation, even in the dilute limit. The transition to a strong coupling regime can be realized by increasing the depth of the lattice potential wells, a quantity that is directly proportional to the intensity of the laser light. This is an experimental parameter that can be controlled with great accuracy. For this reason, besides the fundamental interest for the investigation of quantum phase transitions and other basic quantum phenomena, optical lattices have become an important practical tool for applications, ranging from laser cooling to quantum control and information processing, and quantum computation.

The following part of the present paragraph is devoted to the derivation of an effective description of such nearly periodic cold systems in terms of an Hubbard Hamiltonian (Eqs.(1.1)-(1.3)), following the work of Jaksch *et al.* [15]. The connection between the Hubbard coefficients U, t, and ε with the (few and tunable) microscopic parameters, is explicitly shown for spinless bosons, being other cases (such as spinful bosons or fermions) analogous.

The starting point is the second quantized Hamiltonian, that reads

$$\begin{aligned}\widehat{\mathcal{H}} &= \int \mathrm{d}\mathbf{x}\, \widehat{\Psi}^\dagger(\mathbf{x}) \left[-\frac{\hbar^2}{2M}\nabla^2_{\mathbf{x}} + V_{ext}(\mathbf{x}) \right] \widehat{\Psi}(\mathbf{x}) \\ &\quad + \frac{1}{2}\int \mathrm{d}\mathbf{x} \int \mathrm{d}\mathbf{x}'\, \widehat{\Psi}^\dagger(\mathbf{x})\widehat{\Psi}^\dagger(\mathbf{x}') V_{2b}(\mathbf{x}-\mathbf{x}')\widehat{\Psi}(\mathbf{x}')\widehat{\Psi}(\mathbf{x}) \qquad (1.8)\end{aligned}$$

where $V_{ext}(\mathbf{x})$ is an external applied potential and $V_{2b}(\mathbf{x}-\mathbf{x}')$ accounts for two-body interactions. In a usual axial symmetric magneto-optic harmonic trap the external potential is given by a slowly varying harmonic trap and a rapidly oscillating term that constitutes the lattice (laser wavelength is $2d$).

$$\begin{aligned}V_{ext}(\mathbf{x}) &= \frac{M}{2}\left(\omega_\parallel^2 x^2 + \omega_\perp^2 r^2\right) \qquad (1.9)\\ &\quad + V_0 \sin^2\left(\frac{\pi\, x}{d}\right) \qquad (1.10)\end{aligned}$$

The ratio $\Omega = \omega_\parallel/\omega_\perp$ is inversely proportional to the ratio between the mean square sizes in the two directions. Transverse radius is estimated by the so called "oscillator length" $l_\perp = (\hbar/M\omega_\perp)^{1/2}$. The lattice structure defines a "recoil" momentum $k_R = \pi/d$ and an energy $E_R = (\hbar k_R)^2/2M$. Two basic assumptions are crucial in what follows [15, 45]: first one is that the atoms are confined to the lowest Bloch band of the periodic potential, the other is the dilute gas approximation, i.e. the assumption that binary collisions occur much more frequently than higher order ones.

Diluteness condition is fulfilled when the mean distance between particles is much larger than the typical range of the interatomic forces. The latter could be estimated with the s-wave scattering length a (effective radius of an hard-spheres' gas with the same scattering distribution at small energies). We highlight that, due to particle statistics, only certain channels will be open for such an interaction: in fermionic gases, e.g., only the *singlet* channel (i.e. the antisymmetric one) will enter the game. Under typical experimental conditions, the diluteness parameter $\sqrt{n\,a^3}$ is very small indeed ($\approx 10^{-3}$) and the interatomic forces could be modelled by contact interactions of the form

$$V_{2b}(\mathbf{r},\mathbf{r}') = g\,\delta(\mathbf{r}-\mathbf{r}') \quad \text{with} \quad g = \frac{4\,\pi\,\hbar^2\,a}{M} \qquad (1.11)$$

Positive a indicates repulsion, negative ones attraction: in experiments both cases are met, and Feshbach resonances now allows to tune its value in a

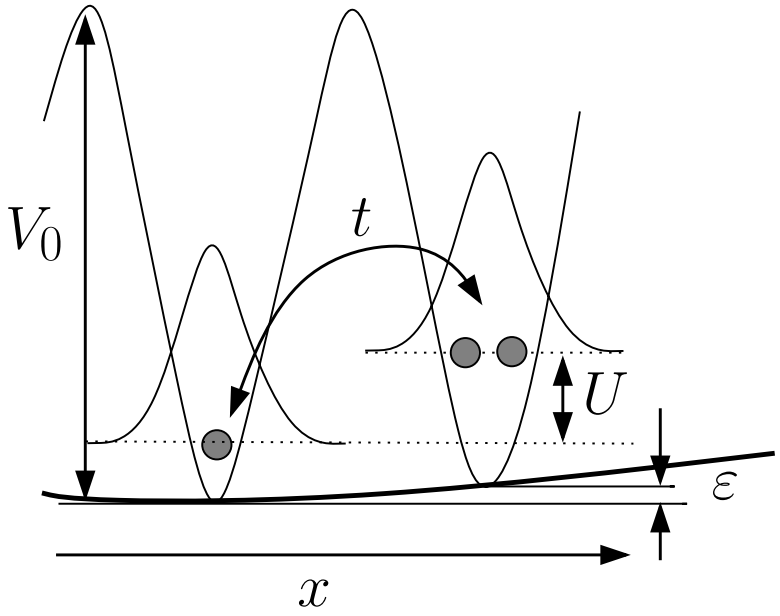

Figure 1.2: Pictorial representation of the Bose-Hubbard terms in an optical lattice. V_0 is the intensity of the laser potential, U the interaction between particles on the same site and t the hopping amplitude through a barrier. The offset ε_i is due to the external shallow trapping potential V_{ext}.

single sample. It is worth to stress that in optical lattices particles are not weakly interacting, as would be the case for alkali atoms in a single trap. Indeed, the more localized is the wavefunction the more important are the correlation effects, and tight lattice wells achieve this aim.

In the presence of a strong optical lattice and a sufficiently shallow external confinement in the x direction, one can employ the well known tight binding approximation. The field operators can be expanded in terms of the single–particle Wannier functions localized at each lattice site $x_i = id$. Single band approximation is satisfied in one-dimensional arrays if the radial waist $l_\perp$ of the system is negligible with respect to the lattice spacing d. Thus the excited bands are much more higher in energy than any other term that will appear in the Hamiltonian. In the harmonic approximation, the Wannier functions $w(\mathbf{r})$ factorize in the product of harmonic oscillator states in each direction, with the trapping potential almost constant between adjacent

lattice sites. We then have

$$\hat{\Psi}(\mathbf{r}) \;=\; \sum_i \widehat{c}_i \, w_x(x - x_i) \, w_y(y) \, w_z(z) \,, \tag{1.12}$$

where $\widehat{c}_i$ are the annihilation operators at the $i-$th site. Substituting this ansatz in Eq.1.8 one obtains the coefficients of the Hubbard Hamiltonian 1.18 in terms of superposition integrals of the Wannier functions (and their derivatives). Constant parts of the external potential, i.e. zero-point energies due to harmonic approximation $\omega_\parallel(\Omega + 1/2)\widehat{N}$, are neglected henceforth. Using the recoil energy as scale unit ($\tilde{E} = E/E_R$), and performing some simplifications they read:

$$\tilde{U} = \sqrt{\frac{8}{\pi^3}} \, \frac{a \, d}{(\ell_\perp)^2} \, \tilde{V}_0^{1/4} \tag{1.13}$$

$$\tilde{\varepsilon}^{(i)} = \frac{i^2}{\pi^2 (\ell_\parallel / d)^4} \tag{1.14}$$

$$\tilde{t} = \left(\frac{\pi^2}{4} - 1 \right) \tilde{V}_0 \, \exp\left[-\frac{\pi^2}{4} \sqrt{\tilde{V}_0} \right] \tag{1.15}$$

We stress the point that, apart from the external confining potential, both t and U can be tuned by means only of the laser intensity V_0. This is one of the key points that explain the popularity of optical lattices.

While the techniques for manipulating trapped ultracold atoms are fairly advanced and have already enabled a broad range of astonishing systems, such as a superfluid, a Mott insulator [16, 17, 46] or a strongly interacting Fermi gas [47] to be realized, the subsequent analysis of their properties turned out to be a challenging task. Indeed it is crucial to have tools at hand that can accurately describe the engineered state, i.e. extracting the correlation functions. Usual experimental detection is based on releasing the trap, waiting some time of flight and then imaging the sample to see the density profile. Such a quantity, after a long enough t, becomes proportional to the momentum distribution in the interacting system [48]:

$$\langle n(\mathbf{r})_t \rangle \propto \frac{m}{\hbar t} \langle n_{\mathbf{q}(\mathbf{r})} \rangle \qquad \mathbf{q}(\mathbf{r}) = \frac{m\mathbf{r}}{\hbar t} \tag{1.16}$$

Moreover, a recent proposal [49] suggested measuring the shot-noise in these images as a universal probe of correlations. The noise in the image-by-image statistics is governed by higher order correlations of the initial state

$$G_{\sigma,\sigma'}(\mathbf{r},\mathbf{r}') = \langle n_{\mathbf{q}(\mathbf{r})} n_{\mathbf{q}(\mathbf{r}')} \rangle - \langle n_{\mathbf{q}(\mathbf{r})} \rangle \langle n_{\mathbf{q}(\mathbf{r}')} \rangle \ . \tag{1.17}$$

Altman *et al.* showed that the shot-noise retains very distinctive fingerprints of the presence of a particular order. This quantity has already been measured experimentally on several occasions [50, 51, 52, 53].

1.2 Bose Hubbard generalities

Specializing what said in the introduction to the present Chapter (and in particular Eq.(1.3)) to the bosonic case, the Bose-Hubbard Hamiltonian reads as

$$\begin{aligned} \mathcal{H}_{BH} &= \mathcal{H}_t + \mathcal{H}_\varepsilon + \mathcal{H}_U \\ &= -\frac{t}{2} \sum_{<ij>} (\widehat{b}_i^\dagger \widehat{b}_j + \widehat{b}_j^\dagger \widehat{b}_i) + \sum_i \varepsilon_i \widehat{n}_i + \frac{1}{2} \sum_i U\, \widehat{n}_i \, (\widehat{n}_i - 1) \end{aligned} \tag{1.18}$$

In absence of the hopping term, a uniform chemical potential $\varepsilon_i = \mu$ fixes the particle number on each site to be equal to its integer part plus one. Once μ is fixed, the Hamiltonian we are considering is thus characterized by two energy scales: an on-site repulsion energy between the bosons U and an hopping energy t which allows bosons to delocalize. At zero temperature and in the limit $U \gg t$ bosons are localized because of the strong local interactions. There is a gap in the spectrum for adding (subtracting) a particle, *hence* the compressibility vanishes. This phase is named the Mott insulator. In the opposite limit, $U \ll t$, bosons are delocalized and hence are in a superfluid phase. There is a direct transition between the Mott insulator and the superfluid state at a critical value of the ratio t/U. Such value $(t/U)_c$ depends on the chemical potential and a lobe structure [36] arises in the $\mu - t$ plane (Fig.1.3): inside the lobes system behaves as a Mott insulator whereas outside it is globally superfluid. At integer values of μ/U two different integer fillings are degenerate and thus superfluidity is present

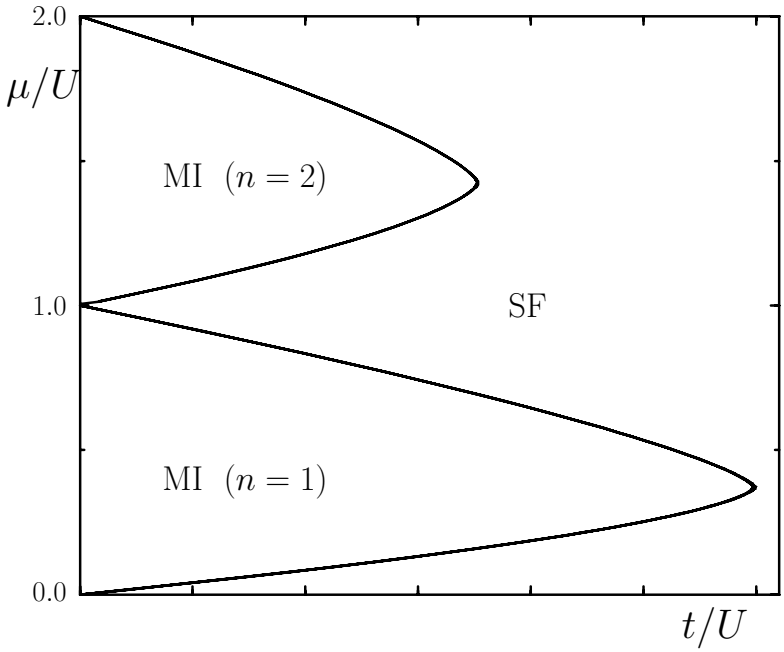

Figure 1.3: Schematic phase diagram of the Bose Hubbard model. The lobe structure described in the text is highlighted. Dimensionality effects are not taken into account here.

for an arbitrarily small hopping t. The higher is the Mott particle number, the higher are the bosonic hopping matrix elements involved and thus the smaller is the lobe in the phase diagram. Dimensionality of the system can affect the form of the lobes and their size, but not this general structure.

The uniform potential picture catches the essential physical effects near the center of a shallow enough trapping potential, where local energy offsets are negligible. More generally, the spatial dependence of ε_i leads to a spatial dependent phase diagram[15]: the system is locally Mott or Superfluid according to the position of (t, ε_i) in Fig.1.3. Henceforth we restrict our analysis to the uniform case, and leave the more realistic one to future investigations.

This Superfluid-Insulator (SI) transition has been extensively studied both theoretically and experimentally and we refer to Refs. [37, 1, 15, 16, 17] (and references therein) for an overview of its properties.

1.2.1 Magnetic frustration

Magnetic frustration can be introduced in the BH-model by appropriately changing the phase factors associated to the hopping amplitudes. The presence of frustration leads to a number of interesting physical effects which has been explored both experimentally and theoretically. In Josephson arrays, where this is realized by applying an external magnetic field, frustration effects have been studied extensively in the past for both classical [54, 55, 56, 57, 58, 59, 60] and quantum systems [1]. Very recently a great interest in studying frustrated optical lattices has emerged as well [61, 62, 63, 64]. There are already theoretical proposals to generate the required phases factors by means of atoms with different internal states [61] or by applying quadrupolar fields [62]. For simplicity we will always refer to $\vec{A}$ as to the vector potential and we will use the magnetic picture also in this case.

A charged particle moving in an external magnetic field will experience a phase shift proportional to the integral of the vector potential $\mathbf{A}$ along the path:

$$A_{i,j} = \frac{2\pi}{\Phi_0} \int_i^j \mathbf{A} \cdot d\mathbf{l} \tag{1.19}$$

where $\Phi_0 = h\,c/\,2\,e$ is the flux quantum. The hopping term will thus become $\widehat{b}_j^{\dagger}\ \widehat{b}_i\ e^{\imath\, A_{i,j}} + h.c.$ If the system is made up of identical plaquettes (as will be the case of lattices studied in Chapters 2-3), all the observables are function of the frustration parameter defined as

$$f = \frac{\Phi}{\Phi_0} = \frac{1}{\Phi_0} \int_P \mathbf{A} \cdot d\mathbf{l} = \frac{1}{2\pi} \sum_P A_{i,j} \tag{1.20}$$

where Φ is the field flux-per-plaquette. It can be shown (and it will be in Sec. 3.2) that if the frustration is rational p/q, then the corresponding $\mathbf{A}$ pattern can be chosen with a period q in lattice units. Due to periodicity of the model it is sufficient to consider values of the frustration $0 \leq f \leq 1/2$.

Among the wide spread of interesting effects determined by magnetic fields studied in literature, we will concentrate our analysis on Aharonov-Bohm (AB) cages (Ch.2-3) and $4e-$condensation (Ch.2). In some particular lattice geometries, magnetic frustration can induce localization without any

kind of disorder [8]. This phenomenon is due to destructive interference along all paths that particles could walk on ($f = 1/2$, i.e. phase factor π circumventing any plaquette). Moreover, in some quasi-$1D$ systems it has been shown that superfluidity onset mechanism is the condensation of pairs of Cooper pairs [65], thus leading to new physics.

1.2.2 Electric frustration

In quantum arrays (electric) frustration can also be induced by changing either the chemical potential (in optical lattices) or by means of a gate voltage (in Josephson junction arrays). This has the effect of changing the energy needed to add/remove a boson on a given island. In the case of long-range interactions, the phase diagram present a richer lobe structure due to ground states with fractional fillings. This states are sort of Wigner-like lattices of bosons commensurate with the underlying lattice [66].

If $U_{i,j}$ is a function of distance only, as it is the case for most of the common situations, changing the chemical potential μ can be seen as changing an offset number n_0 on each site. In the generalized $\mathcal{H}_U$ formulation:

$$\mathcal{H}_U^{'} = \frac{1}{2}\sum_{ij}(\widehat{n}_i - n_0)\, U_{i,j}\, (\widehat{n}_j - n_0) \quad . \tag{1.21}$$

Indeed, the chemical potential is nothing else than $\mu = n_0 \sum_j U_{i,j} - U_{i,i}/2$ and does not depend explicitly on position i. When an external uniform charge frustration is present, the array cannot minimize the energy on each site separately, hence frustration arises. The behaviour of the transition point as a function of the offset charge shows a typical lobe-structure [36, 66] (Fig. 1.3) in which, progressively on increasing the external charge, the filling factor increases as well. In the case of finite range charging interaction also Mott lobes with fractional fillings appear [66] (Fig. 1.4). Differently from the magnetic frustration the value of $n = 1/2$ does not necessarily correspond to fully (charge) frustration as this depends on the range of the interaction $\mathcal{U}_{i,j}$.

An analytical determination of the ground state of the charging Hamiltonian for generic values of the external charge is not possible. For the sake of simplicity, one can consider rational fillings of the whole lattice as made

up of periodic repetitions of a partially filled super-cell of size comparable with the range of the interaction $\mathcal{U}_{i,j}$. Let us consider the simple case of a bipartite lattice of N sites, each with coordination z. If the $\mathcal{U}$ matrix is limited to on-site U_0 and nearest neighbour U_1 terms, it is sufficient to consider the empty state and the periodic checkerboard pattern (half-filling). The corresponding energies are:

$$\begin{aligned} E_{00} &= zN\,U_1\,n_0^2 + N\,\frac{U_0}{2}\,n_0^2 \\ E_{01} &= zN\,U_1\,(1-n_0)(-n_0) + N\,\frac{U_0}{2}\,\left(\frac{1}{2}n_0^2 + \frac{1}{2}(1-n_0)^2\right) \end{aligned}$$

and they become degenerate, i.e. the lobe reaches the $t = 0$ axis, at a charge offset value

$$\overline{n_0} = \frac{U_0}{4(U_0/2 + zU_1)} = \frac{1}{2} - \frac{zU_1}{U_0 + 2zU_1)} \tag{1.22}$$

The longer is the interaction range the richer is the lobe structure of the phase boundary in the $n_0 - t$ $(\mu - t)$ plane (see Fig. 3.9).

Finally, we recall that the presence of the offset breaks the particle-hole symmetry and thus the universality class of the phase transition change [36].

1.2.3 Spin degrees of freedom

In conventional magnetic traps, only one spin component is trapped and thus spin degrees of freedom are frozen. The atoms can then be treated as effectively spinless particles. In contrast, optically trapped atoms [67] have extra spin degrees of freedom which can exhibit different types of magnetic orderings. In particular, alkali atoms have a nuclear spin $I = 3/2$; lower energy hyperfine manifold has 3 magnetic sublevels and a total moment $T = 1$. As for spinless particles, loading the spinor bosons into a lattice enhances the spin effects and thus offers novel realizations of quantum magnetic systems. This allows physicists to go beyond the simple explanation of details of particular experiments on peculiar samples with complicate structures (such as cuprate superconductors or organic materials). Stronger interactions and smaller occupation number open the fascinating possibility of several insulating phases according to different spin correlations [14].

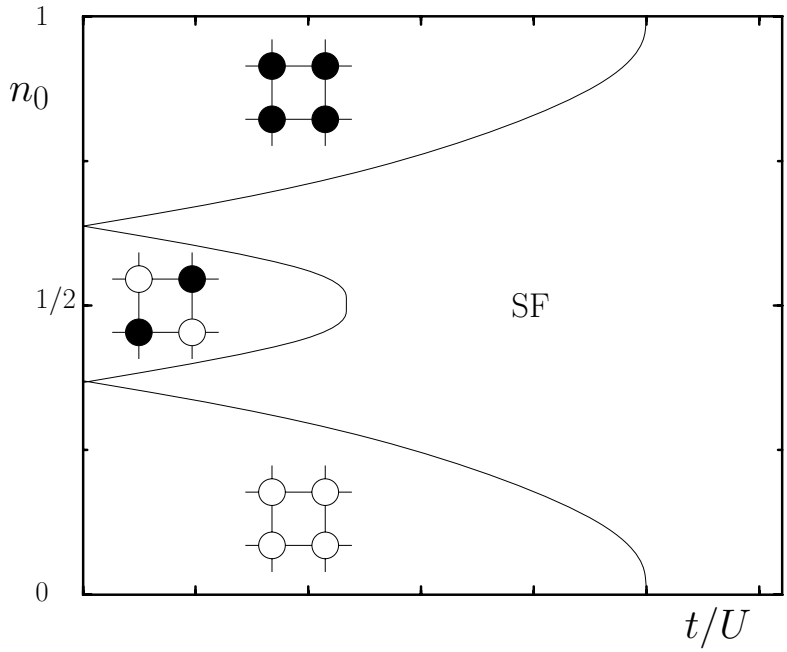

Figure 1.4: Schematic phase diagram of the QPM in presence of an offset, for a bipartite lattice with nearest neighbours interactions (coordination number z). On the n_0 axis, the amplitude of the *checkerboard* lobe is $2zU_1/(U_0+2zU_1)$ around $n_0 = 1/2$, where U_0 and U_1 are the local and n.n. energy terms (Eq. (1.22))

In $s-$wave approximation, scattering between two identical bosons with hyperfine spin 1 is well described by the contact potential:

$$\begin{aligned} V_{2b}(\mathbf{x}) &= \frac{4\pi\hbar^2}{M}\,\delta(\mathbf{x})\,(a_0\mathcal{P}_0 + a_2\mathcal{P}_2) \\ &= \frac{4\pi\hbar^2}{3M}\,\delta(\mathbf{x})\,((a_0+2a_2)\mathbb{I} + (a_2-a_0)\mathbf{T_1}\cdot\mathbf{T_2}) \end{aligned} \tag{1.23}$$

where subscript labels denote the total spin of the incident pair and $\mathcal{P}_T$ are spin channel projectors, a_T are the s-wave scattering lengths and M is the atomic mass. Generalization of the tight binding approach applied in Sec.1.1 to Eq.(1.11) leads to the presence of an extra term:

$$\frac{U_2}{2}\sum_i \left(\widehat{\mathbf{S}}_i^2 - 2\widehat{n}_i\right)\,. \tag{1.24}$$

The total spin operator on a site given by $\widehat{\mathbf{S}}_i = \sum_{\sigma,\sigma'}\widehat{b}^\dagger_{i,\sigma}\mathbf{T}_{\sigma,\sigma'}\widehat{b}_{i,\sigma'}$, where $\widehat{\mathbf{T}}$ are the usual spin-1 operators for single particles (the boson operators have

the additional label σ). The ratio between the interaction couplings is bound to be

$$\frac{U_2}{U_0} = \frac{a_2 - a_0}{a_0 + 2a_2} \quad \longrightarrow \quad -1 < \frac{U_2}{U_0} < 1/2 \; . \tag{1.25}$$

The tunnelling preserves the single particle spin, i.e. there are three independent channels and their couplings are equal. The appropriate Hamiltonian to describe such systems is thus given by the sum of Eqs.(1.18) and (1.24):

$$\begin{aligned} \widehat{\mathcal{H}} &= \frac{U_0}{2} \sum_i \widehat{n}_i(\widehat{n}_i - 1) + \frac{U_2}{2} \sum_i \left(\widehat{\mathbf{S}}_i^2 - 2\widehat{n}_i \right) - \mu \sum_i \widehat{n}_i \\ &- t \sum_{i,\sigma} \left(\widehat{b}^\dagger_{i,\sigma} \widehat{b}_{i+1,\sigma} + \widehat{b}^\dagger_{i+1,\sigma} \widehat{b}_{i,\sigma} \right) \; . \end{aligned} \tag{1.26}$$

Atoms residing on the same lattice site have identical orbital wave function and their spin function must be symmetric: such a constraint imposes that $s_i + n_i$ must be even[1]. Uniqueness of the completely symmetric state

[1] A quick proof is the following:
Since atoms residing on the same lattice site have identical orbital wave function, the single particle state is labelled only by $z = 0, \pm 1$ (projection of $S = 1$ along the quantization axis). Bose-Einstein statistics admits only $n-$body states invariant under the action of the permutation group $\mathbb{Z}_n$. The number of such states corresponds to the number of independent orbits of the group. In this case, an orbit of the group is identified by the component numbers $n_0, n_\pm$.
For fixed number of particles n and magnetization $s^z = n - m$ one has to satisfy the constraints $n_+ + n_0 + n_- = n$ and $n_+ - n_- = s^z = n - m$ that are equivalent to

$$\begin{cases} 2n_+ + n_0 &= 2n - m \\ 2n_- + n_0 &= m \end{cases} \tag{1.27}$$

which admit $[m/2]+1$ independent solutions: $n_- = 0, 1, \ldots, [m/2]$. The lowering operator $S^- = \sum_{p=1}^n S_p^-$ is invariant under $\mathbb{Z}_n$, and thus preserves the symmetry properties of a state. On the other hand, it is well known that from $|s,\, s^z = s\rangle$ it is possible to obtain all other states with the same total spin $|s,\, s^z\rangle$ simply applying iteratively S^-.
For $m = 0$ the unique symmetric state has total spin $s = n$; when $m = 1$ only one orbit is present and the corresponding state cannot be other than the "son" $|n, n-1\rangle$ of $|n, n\rangle$. On the other hand, for $m = 2$ a new possibility opens: apart from $|n, n-2\rangle$, another independent symmetric state is present. It must have $s = n - 2$ since there is no possible "father" with higher spin and the same $\mathbb{Z}_n$ properties. Thus each time m is even a new independent orbit appears, and it is possible to create a state with a total spin $s - m$. This concludes the proof, since $n + n, n + (n-2), \ldots$ are evidently even.

with fixed spin and number makes it possible to denote single site states with $|n_i, s_i, z_i\rangle$ (z_i is the z-projection of the i^{th} spin).

Effects of the spin degrees of freedom on the phase diagram will be analyzed in details in Ch. 4, where the possibility of different magnetic ordering in both Mott and superfluid phases (dimerized, nematic and singlet Mott; polar, singlet superfluid; etc.) emerges. Here we stress only the fact that the sign of U_2 distinguishes between on-site ferromagnetic ($U_2 < 0$, ground with $S = n$) and anti-ferromagnetic behaviours ($U_2 < 0$, minimum allowed spin value preferred). And we highlight the fact that, deep in the first Mott lobe described before, these systems can be seen as experimental implementations of spin-1 chains, offering the possibility of studying the phase diagram of the (generalized biquadratic) Heisenberg model (see Sec.4.2).

1.3 Fermi-Hubbard model: generalities

Coming to fermionic side of the world, we will focus our attention on a system where particles have some internal degree of freedom, henceforth addressed as spin. Within an s-wave scattering model, parallel-spin fermions do not interact while antiparallel-spin fermions interact via a contact potential with an effective coupling strength $g_{1\mathrm{D}}$ as determined by Olshanii [68] for the case of $1D$ confinement.

The resulting (Sec. 1.1.2) single-band Fermi-Hubbard Hamiltonian with spin is

$$\hat{\mathcal{H}} = -t \sum_i \sum_\sigma \left[\hat{c}^\dagger_{i,\sigma}\, \hat{c}_{i+1,\sigma} + \mathrm{h.c.} \right] + U \sum_i \hat{n}_{i,\uparrow}\, \hat{n}_{i,\downarrow} + V_2 \sum_i (i - L/2)^2 \hat{n}_i \,, \tag{1.28}$$

where t is the first-neighbor hopping matrix element and $\hat{n}_{i,\sigma} = \hat{c}^\dagger_{i,\sigma}\hat{c}_{i,\sigma}$ is the spin-resolved site occupation number, with $\hat{n}_i = \sum_\sigma \hat{n}_{i,\sigma}$. The system size L will always be chosen so that the trap makes the ground-state site occupation $n_i = \langle \Psi_{\mathrm{GS}} | \hat{n}_i | \Psi_{\mathrm{GS}} \rangle$ go to zero smoothly near the edges of the lattice.

In the absence of confinement ($V_2 = 0$) the model reduces to the $1D$ Hubbard model, which has been solved exactly by Lieb and Wu [69, 70]. For $V_2 \neq 0$ we calculate the ground-state properties of $\hat{\mathcal{H}}$ in Eq. (1.28) by

resorting to the density-matrix renormalization-group (DMRG) method [71], which provides a practically exact solution for any value of U/t. Motivated by the recent interest in the development of density-functional schemes for strongly correlated $1D$ systems [72, 73, 74, 75, 76, 77, 78] we also use, in parallel to DMRG, a lattice density-functional scheme based on the Lieb-Wu solution for $V_2 = 0$ as a a local-density approximation. This choice of the reference system thus embodies the exactly known correlations of a Luttinger liquid (for repulsive interactions, $U > 0$) or of a Luther-Emery liquid (for attractive interactions, $U < 0$). These calculations employ the Bethe-*Ansatz* Local-Density Approximation (BALDA) in its fully numerical formulation [73]. The BALDA method allows us to efficiently treat complex systems with a very large number of sites. The combined use of DMRG and BALDA allows a detailed understanding of the problem and paves the way for further extensions.

Figure 1.5 shows a sketch of the phases of a spin-balanced gas under harmonic confinement for the case of interspecies repulsions, in dependence of the average number of fermions per site. Starting with a Luttinger liquid in phase $\mathcal{A}$ for values of the site occupation number in the range $0 < n_i < 1$, one meets (i) phase $\mathcal{B}$ where an incompressible Mott insulator occupies the bulk of the trap with the site occupation number n_i locally locked to 1; (ii) phase $\mathcal{C}$ where a fluid with $1 < n_i < 2$ is embedded in a Mott plateau; (iii) phase $\mathcal{D}$ where a band insulator, with n_i locally locked to 2, is surrounded by fluid edges and embedded in a Mott insulator; and finally (iv) phase $\mathcal{E}$ where a band insulator with $n_i = 2$ coexists with fluid edges.

Restricting our investigations to the attractive particle interactions *i.e.* $U < 0$, some very peculiar phases show up. Namely these are the Luther-Emery liquid [79] ($N_\uparrow = N_\downarrow$), i.e. a peculiar 1D liquid phase with a massive spin sector, and a Fulde-Ferrel-Larkin-Ovchinikov [80, 81] superconductor, i.e. one with spatial order parameter dependent on the distance between Fermi surfaces ($N_\uparrow > N_\downarrow$).

If one consider spin-balanced populations, in the case of attractive interactions, fermions are predicted to exhibit a gap in the spin sector. This induces an exponential decay of spin correlations, while singlet superconduct-

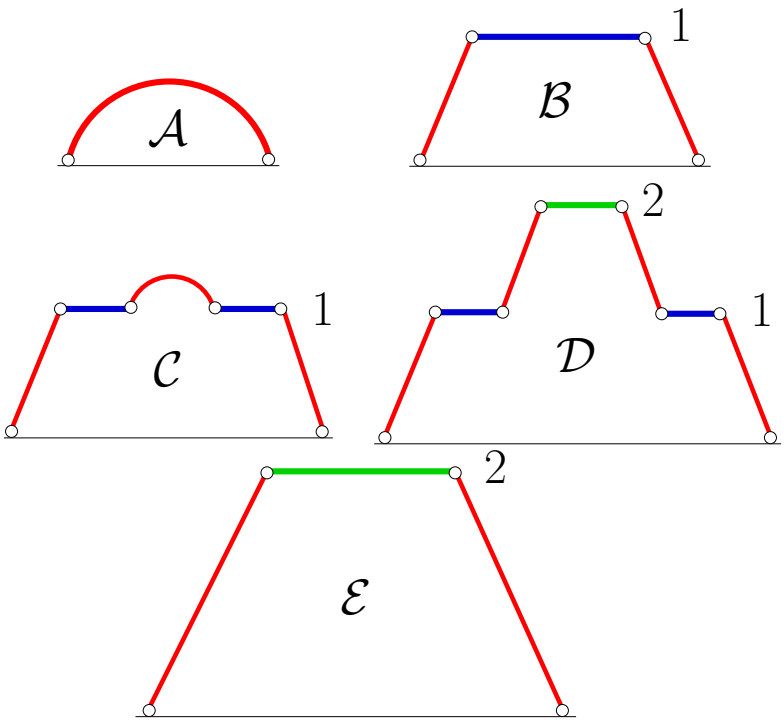

Figure 1.5: Sketch of the phases of a confined Luttinger liquid on a lattice for increasing number of fermions. Horizontal lines represent Mott plateaus, with the others being liquid phases.

ing and charge-density wave correlations have a power-law decay [30]. So far no observation of the Luther-Emery phase has been reported in solid-state electronic systems. In Sec. 5.1 we will propose realistic 1D Optical Lattices as a tool to realize and highlight the presence of such a phase [82].

Going to the more general case of polarized systems, an even more exotic phase, the FFLO phase [80, 81], has recently attracted a great deal of interest in both the experimental and the theoretical community [83, 84, 85, 86, 87, 88, 89, 90]. In such a phase Cooper pairing occurs at a finite momentum equal to the distance between the two distinct Fermi surfaces $\mathbf{q} = \mathbf{k}_{F\uparrow} - \mathbf{k}_{F\downarrow}$, yielding a spatially-dependent superconducting order parameter. The region of parameter space available for the FFLO phase in $3D$ space is however quite modest [84]. Quasi-one dimensional systems are, on the contrary, very

well known to be good candidates for the realization of the FFLO phase [84, 91, 92, 93]. In Sec. 5.2 we will show that a spin-polarized attractive Fermi gas loaded in a $1D$ OL is always in a polarized superfluid state of the FFLO type.

Chapter 2

Fully frustrated Josephson diamond chain

Josephson arrays in the quantum regime have been studied extensively [1], both experimentally and theoretically, as model systems where to investigate a variety of quantum phase transitions. The application of a magnetic field creates frustration and leads to a number of interesting physical effects[1, 2, 3].

Very recently, renewed interest in frustrated Josephson networks has been stimulated by the work by Vidal *et al.* [8] on the existence of localization in fully frustrated tight binding models with $\mathcal{T}_3$ symmetry (see Ch.3). Localization in this case is due the destructive interference for paths circumventing every plaquette. These clusters over which localization takes were named *Aharonov-Bohm* (AB) *cages*. Experiments in superconducting networks have been performed and the existence of the AB cages has been confirmed through critical current measurements both in wire [94] and junction [95, 96] networks. Starting from the original paper by Vidal *et al.* several aspects of the AB cages both for classical [97, 97, 98, 99] and quantum [100] superconducting networks have been highlighted.

The basic mechanism leading to the AB cages is also present in the (simpler) quasi-one-dimensional lattice shown in Fig.2.1. At fully frustration, it has been shown [65] that superconducting coherence is established through-

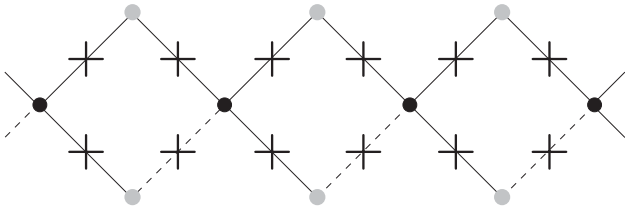

Figure 2.1: The diamond chain Josephson network analyzed in the present paper. The crosses represent the Josephson junctions connecting two neighbouring superconducting islands. In the chain there are two types of inequivalent sites with two (grey) and four (black) neighbours. By an appropriate choice of the gauge, the magnetic phase factors $A_{i,j}$ can be chosen to be zero on the three links indicated by a continuous lines and f in the fourth one indicated by a dashed line.

out the system by means of $4e$-condensation. The global superconducting state is due to the condensation of *pairs* of Cooper pairs. Predictions on the critical current of the diamond chain amenable of experimental confirmation have been put forward by Protopopov and Feigelman [101, 102]. Unusual transport properties of these systems have been also predicted in semiconducting samples [103, 104]. In this chapter we present the results of our Monte Carlo simulations [105] on the Josephson junction network with the geometry depicted in Fig.2.1. Our aim was to perform a detailed quantitative analysis of the phase diagram predicted in Ref.[65]. In order to have a fairly complete description of the effect of frustration in this case, we considered the stiffness and phase correlators for three values of the frustration parameter; i.e. $f = 0$, $f = 1/3$ and $f = 1/2$.

2.1 Basic definitions

As yet explained in Sec. 1.1.1, the Hamiltonian that we use to describe a Josephson junction network is the so called Quantum Phase (or Quantum Rotor) one:

$$\mathcal{H} = E_0 \sum_i n_i^2 - E_J \sum_{\langle i,j \rangle} \cos(\varphi_i - \varphi_j - A_{i,j}) \ . \tag{2.1}$$

For the sake of simplicity we neglect here long-range electrostatic effects and we restrict our analysis to a purely on-site interaction (charging energy E_0), written in the first term. The implicit assumption is that more complicate structures of U_i, j would only modify quantitatively the Mott-Superfluid transition point but not the qualitative behaviour that is depicted below. See Ref.[101] for the more realistic case of long range charging interaction.

In the second term, i.e. the Josephson contribution, the phase of the superconducting order parameter in the i-th island is denoted by φ_i and $A_{i,j} = \frac{2\pi}{\Phi_0} \int_i^j \mathbf{A} \cdot d\mathbf{l}$ is the magnetic phase factor (see Sec. 1.2.1) along the link. Such a shift is necessary to satisfy a gauge-invariant definition of the phase in presence of an external of a vector potential $\mathbf{A}$ and flux-per-plaquette Φ ($\Phi_0 = h\,c/\,2\,e$ is the flux quantum). All the observables are function of the frustration parameter defined as

$$f = \frac{1}{\Phi_0} \int_P \mathbf{A} \cdot d\mathbf{l} \; = \frac{1}{2\pi} \sum_P A_{i,j} \; .$$

where the line integral is performed over the elementary plaquette. With a proper gauge choice, the magnetic phase factors $A_{i,j}$ can be chosen to be zero on the three links indicated by a continuous lines and f in the fourth one indicated by a dashed line in Fig.2.1. Due to the periodicity of the model it is sufficient to consider values of the frustration $0 \leq f \leq 1/2$.

Let us consider a particle starting on a site with coordination $z = 4$ (black in the picture): it can reach all its nearest neighbours by means of a hopping since there are no interferences. If we consider then its two next-nearest neighbours, for each of them there is a pair of paths made by two hoppings. But these two paths are destructively interferant if the frustration is $1/2$, and thus the particle cannot escape from this "cage". Particles are trapped in a similar way even if they start from a grey site ($z = 2$), and thus localization without disorder is achieved. This is the key mechanism of the so called Aharonov-Bohm (AB) cages highlighted by the work of Vidal in particular two dimensional geometries [8] (see Chapter 3).

In order to perform numerical simulations, it is useful to map the quantum phase model into an effective classical $(d + 1)$-dimensional XY-model [106, 107] (here $d = 1$). Technical details are given in App. A, here we present only

the basic idea. Exploiting the canonical commutation rules of Eq. (1.7), the charging term can be expressed in terms of second derivative of the phase φ. After that a Trotter-Suzuki approximation is applied to the imaginary time representation of the partition function, cutting the time axis into slices. The resulting interaction between sites residing on different time slices is then found out to be an approximation of a cosine. Thus finally one gets the XY model with one extra dimension, with action given by

$$\begin{aligned} \mathcal{S} &= -K \sum_{i,\langle k,k' \rangle} \cos\left(\varphi_{i,k} - \varphi_{i,k'}\right) \\ &\quad -K \sum_{\langle i,j \rangle,k} \cos\left(\varphi_{i,k} - \varphi_{j,k} - A_{i,j}\right) . \end{aligned} \tag{2.2}$$

The effective dimensionless coupling is defined as $K = \sqrt{E_J/E_0}$. The index k labels the extra (imaginary time) direction which takes into account the quantum fluctuations (the vector potential does not depend on the imaginary time). At zero temperature the system extends to infinity also along the time direction.

Simulations were then performed with MonteCarlo methods by using a standard Metropolis algorithm. They where performed on $L \times L$ lattice with periodic boundary conditions (the largest lattice was 72×72). A finite size scaling analysis has then been done to extract indications about the thermodynamic limit. In Eq.(2.2) the couplings along the time and space directions have been made equal by a proper choice of the Trotter time slice [106, 107]. This choice, with no consequences on the study of the zero temperature phase transition, makes the analysis of the Monte Carlo data considerably simpler. The expectation values of the different observables (stiffness and correlation functions) have been obtained averaging up to 10^5 Monte Carlo configurations by using a standard Metropolis algorithm. Typically the first half of configurations, in each run, were used for thermalization.

2.2 Determination of the phase transition

In order to characterize the phase diagram we studied the phase stiffness, defined as the resistance of the system to undergo a phase twist across it

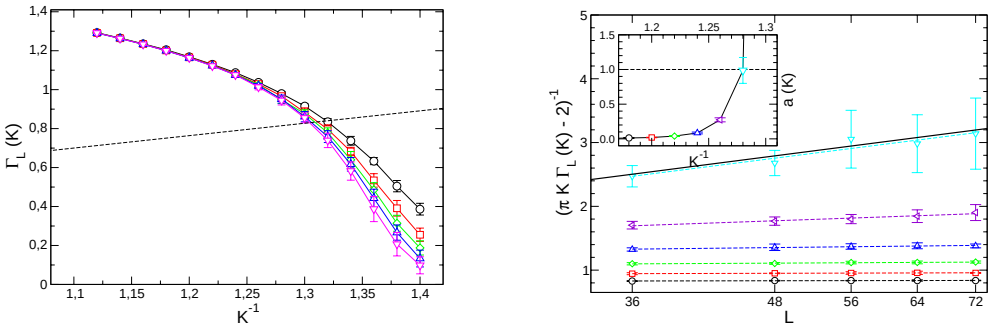

Figure 2.2: In the upper panel, the stiffness for the case of $f = 0$ frustration is plotted against the coupling. Different symbols correspond to different sizes of the chain: circles to $L = 36$, squares to $L = 48$, diamonds to $L = 56$, triangles up to $L = 64$, and triangles down to $L = 72$. The dashed line with slope $2/\pi$ gives a rough estimate of the transition point. A better estimate is obtained by means of the finite size scaling shown in the lower panel and explained in the text. Thick black line has exactly slope 1 and is plotted as a reference guide. The value of l_0 at the transition is 2.9.

and proportional to the superfluid density [108]. If one impose a phase twist along the spatial direction $\mathbf{e}$, i.e. $\varphi_i \to \varphi_i + \theta_{\mathbf{e}}\, \mathbf{e} \cdot \mathbf{r}_i$, the stiffness Γ is the corresponding "susceptibility":

$$\Gamma = \left. \frac{\partial^2 \mathcal{F}(\theta_{\mathbf{e}})}{\partial \theta_{\mathbf{e}}^2} \right|_{\theta_{\mathbf{e}}=0} . \tag{2.3}$$

The critical point is expected to be of the Berezinskii-Kosterlitz-Thouless universality class [6, 7, 65]. Its location can be determined using the following *ansatz* for the size dependence of $\Gamma_L(K_c)$ [109]

$$\frac{\pi K_c}{2}\, \Gamma_L(K_c) = 1 + \frac{1}{2\ln(L/l_0)} \tag{2.4}$$

where l_0 is the only fit parameter. In the presence of frustration, the universality class of the transition may be different from that of the unfrustrated case. In the case of the two-dimensional fully frustrated XY-model this issue has been investigated in great detail (see Ref. [110] and refs. therein). Up to date, there is no unanimous consensus on the nature of the transition.

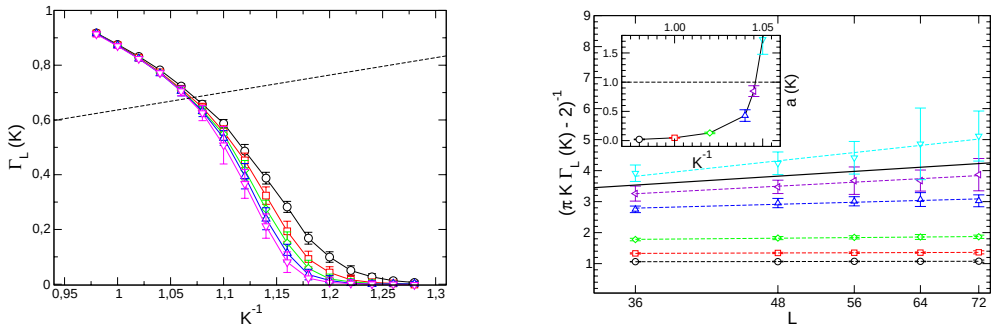

Figure 2.3: The same plots of Fig.2.2 for the case of $f = 1/3$. The critical point is $K_c^{-1} = 1.045 \pm 0.005$. The value of l_0 at the transition is 0.8 (thick line).

However, we suppose that the transition belongs to the BKT universality class, as suggested by Ref.[65], and determine the critical value by means of Eq.(2.4).

We first analyze the $f = 0$ case and extract the value of the critical coupling from the stiffness. This extrapolation has been done by performing a linear fit in logarithmic scale

$$[\pi\, K\, \Gamma(K) - 2]^{-1} = a(K) \ln L - \ln l_0 \tag{2.5}$$

and searching for the coupling value such that $a(K) = 1$. This coupling value is then identified with the critical point K_c. The proposed ansatz fits quite well the data and the estimated value of the critical coupling is $K_c^{-1} = 1.28 \pm 0.01$ which corresponds to $(E_J/E_0)_c \sim 0.61$. Data are reported in Fig.2.2.

We then analyze the transition at $f = 1/3$ and find out that the transition point $K_c(1/3) = 1.045 \pm 0.005$ is slightly smaller than the unfrustrated one $K_c(0)$. In fact, this means that the critical value of the Josephson coupling $E_{Jc} = 0.91 \pm 0.01 E_0$ required to establish superfluid coherence is larger for $f = 1/3$ since interference disturbs delocalization of Cooper pairs. Results are presented in Fig. 2.3.

Finally we present the numerical results for the fully frustrated situation, where the situation is not so clear as in the yet analyzed ones. As one could expect, the transition happens in a region with K values much smaller than

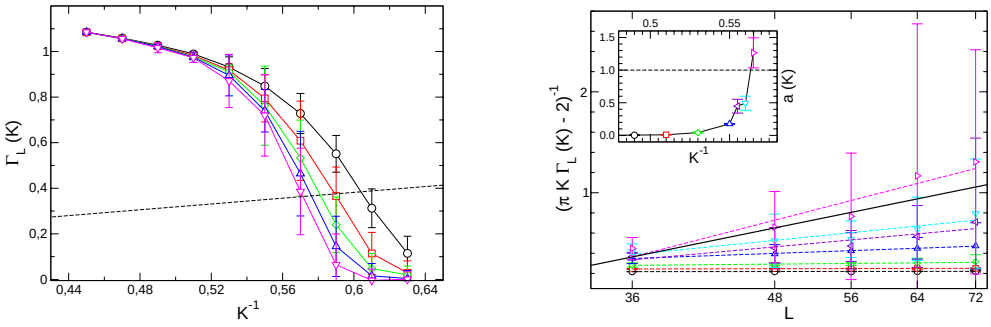

Figure 2.4: The same plots of Figs.2.2-2.3 for $f = 1/2$. Compared to the cases of $f = 0$ and $f = 1/3$, the superfluid region is considerably shrunk. The value of l_0 at the transition is 25.

the unfrustrated critical point but it's not easy to estimate its precise value. Simulation data are much more scattered than the previous ones and thus error bars are relevant. The value of $l_0 = 25$ at the estimated $K_c(1/2) \simeq 0.56$ indicates that we probably we need larger chains in order to really enter the critical region. Another indication of this fact emerges in the upper panel of Fig.2.2 where the line of slope $2/\pi$ crosses the data already when the stiffness is decreasing to zero. In order to put bounds to the critical point in the fully frustrated case we plot in Fig.2.5 the stiffness as a function of the system size. From the raw data it is possible to bound the transition point in the range $0.55 \leq K_c^{-1} \leq 0.57$.

All these results are summarized in table below:

f	0	1/3	1/2
K_c^{-1}	1.28 ± 0.01	1.045 ± 0.005	0.56 ± 0.05
$(E_J/E_0)_c$	0.61 ± 0.01	0.91 ± 0.01	3.2 ± 0.6

The ratio of the obtained critical couplings for $f = 0$ and $f = 1/2$ is $K_{c,1/2}/K_{c,0} = 2.28$. On the other hand, the proposed mechanism of condensation of pairs of Cooper pairs [65] would predict a ratio 4. Doubling the charge implies indeed halving the effective charge of the topological excitations that unbind at the BKT critical point, and T_c (K_c^{-1} in our formalism) scales quadratically with this charge. This apparent failure may be due to the fact that the screening of the vortices is different in the unfrustrated and

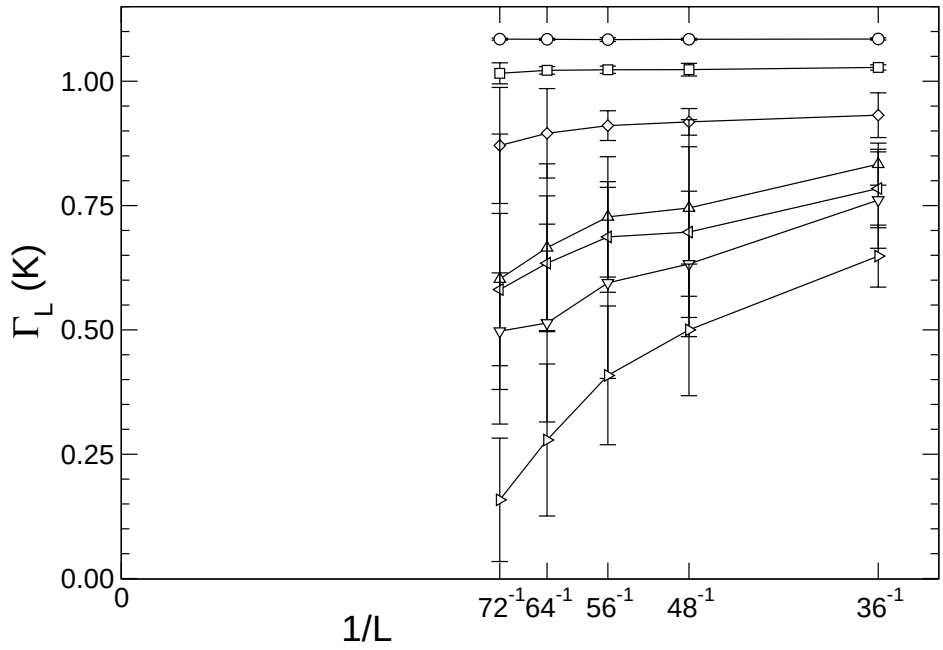

Figure 2.5: The stiffness is plotted as a function of the system size for different values of K in the critical region. This plot highlights the existence of a transition, though do not allow to extract the transition point. For $K^{-1} < 0.55$ data seem to scale to a finite value in the thermodynamic limit, whereas over 0.57 it seems clear that they go to zero. Different symbols correspond to values of K^{-1}: circles (0.45), squares (0.49), diamond (0.53), triangles up (0.555), triangles left (0.56), triangles down (0.565), triangles right (0.575).

fully frustrated case, therefore leading to a further correction in the ratio between the two critical points.

2.3 Superfluidity onset mechanism

The differences in the fully frustrated case manifest dramatically in the way condensation is achieved. As predicted by Douçot and Vidal [65], the destructive interference built in the diamond structure prevents Cooper pair to have (quasi-)long range order. The superfluid phase is then established via the delocalization of pairs of Cooper pairs. This is at the origin of the

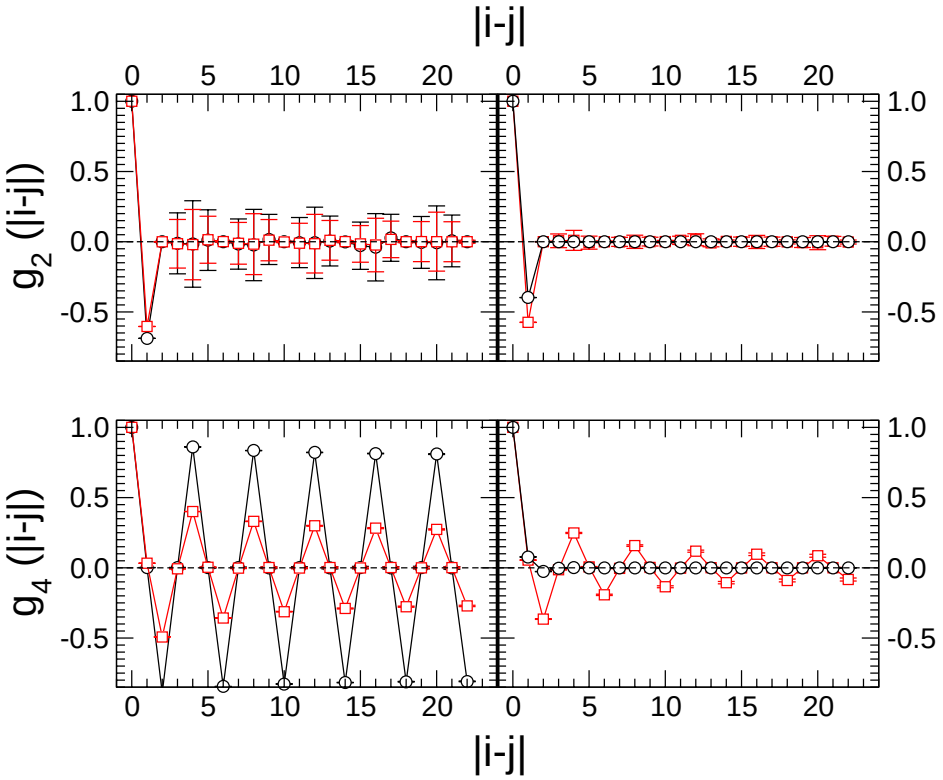

Figure 2.6: The phase correlators g_2 and g_4 are shown as a function of the distance for the *fully frustrated* case $f = 1/2$. Data are plotted for a chain with $L = 48$. On the left side circles correspond to $K^{-1} = 0.1$ deep in the ordered phase and squares to $K^{-1} = 0.5$ on the border of it. On the right side, squares are $K^{-1} = 0.6$ and circles $K^{-1} = 1.2$, deep in the Mott insulator phase. Differently from g_2, the correlator g_4 shows quasi-long range order.

$4e-$condensation.

In order to check this point, the knowledge of the phase-phase correlators is required. Quasi-long range behaviour in a two-point correlation function of the type

$$g_{2n}(|i-j|) = \langle \cos n(\varphi_i - \varphi_j) \rangle \tag{2.6}$$

signals the existence of condensation of $2n$ charged objects. In fact, the exponentials $e^{(-)\imath\phi_i}$ act as pure (without prefactors) creator (annihilator) operators for Cooper pair on an island. In Fig.2.6 we discuss their properties.

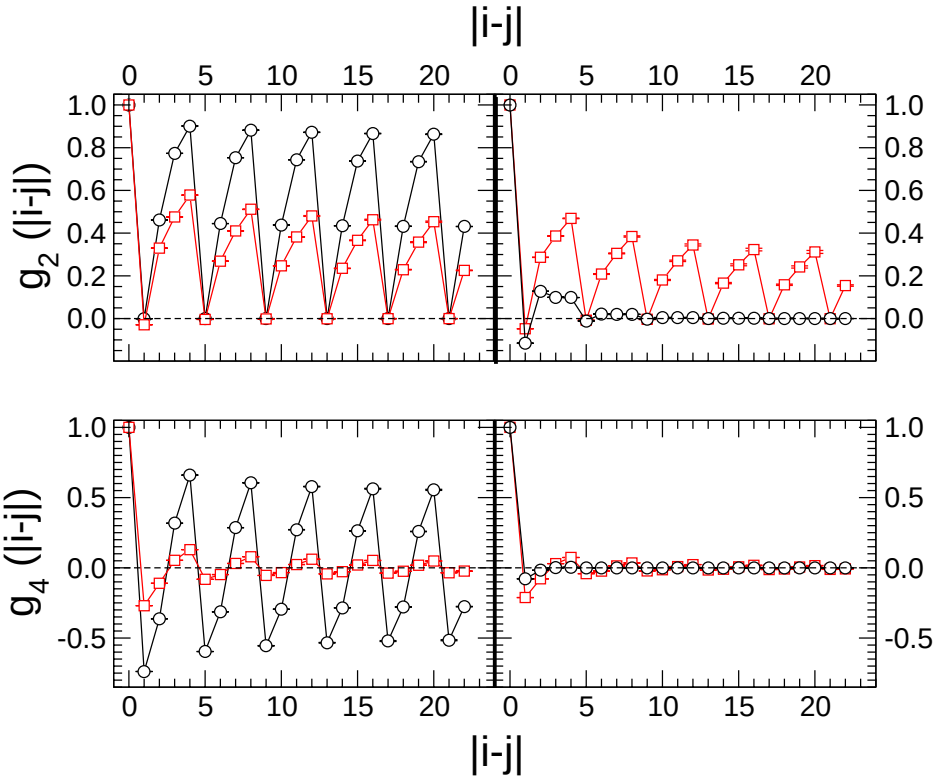

Figure 2.7: Phase correlators at frustration $f = 1/3$. Up: the phase correlator $g_2(|i-j|)$ is shown as a function of the distance between the sites both in the ordered phase (left panel), $K^{-1} = 0.3$ (circles) and 1.0 (squares) and in the Mott insulator phase (on the right) $K^{-1} = 1.1$ (squares) and 1.4 (circles). Differently from the fully frustrated case, here the phase correlator of Cooper pairs changes its behaviour at the critical point. Down: the phase correlator $g_4(|i-j|)$ is shown for the same coupling values as upwards.

In the upper panels, we consider the phase-phase correlator g_2 for two different couplings deep in the superfluid and Mott insulating phases respectively. What is evident from the figure is that, despite the fact that the system is phase coherent, phase correlations decay very fast almost independently from the value of K. As explained in [65], this behaviour should be ascribed to the existence of the Aharonov-Bohm cages.

However, even if hopping of single Cooper pairs is forbidden because of

quantum interference, correlated hopping of two pairs does not suffer the same destructive interference. In the lower panels of the same figure, the space dependence of the correlator g_4 is plotted for the same coupling as upwards. The different behaviour between the Mott and the superfluid phase is now evident. The correlator decays exponentially only for $K^{-1} = 1.2 \gg K_c$ (right side): in the other panel, differently from g_2, the decay is power-law like.

For comparison we report also simulations of the phase correlators for the case $f = 1/3$. In this case the "standard" condensation of Cooper pair is observed as witnessed by the behaviour of g_2 shown in Fig.2.7. In this *partially* frustrated case, the decay of the one-particle correlations is not immediate and regardless of the coupling but shows a clear tendency to (quasi-)long range ordering for $K < K_c(1/3)$.

We thus furnished numerical evidence supporting the existence of a different mechanism for the onset of superfluidity in the case of quasi-1D frustrated systems. Even more interesting effects of magnetic fields on Josephson Junction Arrays will be the object of next Chapter about two dimensional dice lattices.

Chapter 3

Two dimensional $\mathcal{T}_3$ lattice

In the present chapter we focus our attention to a two dimensional bipartite structure with differently coordinated sublattices, illustrated in Fig.3.1 and known as $\mathcal{T}_3$ or dice lattice [111]. The interest in the properties of these lattices has been stimulated by the yet cited work by Vidal *et al.* [8] on the existence, in fully frustrated dice lattices, of Aharonov-Bohm (AB) cages for all the sites. Destructive interference along every path leads to localization without any kind of disorder.
In quantum arrays (charge) frustration can also be induced by changing either the chemical potential (in optical lattices) or by means of a gate voltage (in Josephson junction arrays). The typical lobe-like structure [36] (see Sec.1.2.2) of the phase diagram is related to the onset of Wigner-like lattices of bosons commensurate with the underlying lattice [66].
Due to the particular topology of the $\mathcal{T}_3$ lattice the superconducting phase is characterized, even at zero frustration, by a modulation of the order parameter on the different sublattices (i.e. hubs and rims), which indicates a different phase localization on islands depending on their coordination number [100].

The location and the properties of the phase diagram will be analyzed by a variety of approximate analytical methods (mean-field, variational Gutzwiller approach, strong coupling expansion, see Sec. 3.2) and by Monte Carlo simulations (Sec. 3.3.4). The $\mathcal{T}_3$ lattice has been experimentally realized in Josephson *arrays* [95]; in addition we show that it is possible to realize it ex-

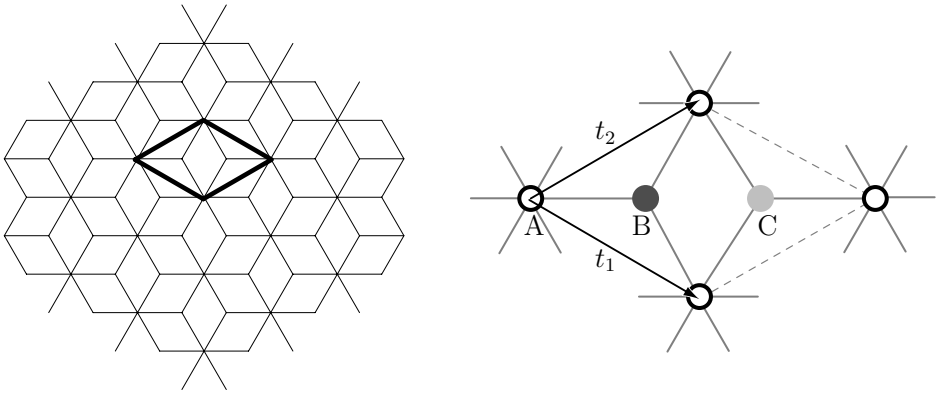

Figure 3.1: The $\mathcal{T}_3$ lattice: it consist of hubs (with six nearest neighbours) connected to rims (three nearest neighbours). Lines between the sites corresponds to those links where boson hopping is allowed.The $\mathcal{T}_3$ structure is a Bravais lattice with a base inside the conventional unitary cell. The lattice vectors are $\mathbf{t_1}$ and $\mathbf{t_2}$. The basis is given by the sites A,B,C. Due to the fact that these sublattices are not self–connected and have different coordination numbers, we refer to this structure as tripartite. All rhombic plaquettes are identical, although differently oriented.

perimentally also with optical lattices [100] (Sec. 3.1.2). Although the main properties of the phase diagram are common to both experimental realizations, there are some differences which are worth to be highlighted. The zero-temperature phase diagram, in the presence of magnetic and electric frustration, will then be described in Sec. 3.3. We first discuss the unfrustrated case and afterwards we consider the role of electric and magnetic frustration respectively. In particular we will provide evidences that there is an important signature of the Aharonov-Bohm cages in the quantum phase diagram. It seems that due to the AB cages a new phase intermediate between the Mott insulating and superfluid phases should appear. On varying the ratio between the hopping and the Coulomb energy the system undergoes *two* consecutive quantum phase transitions. At the first critical point there is a transition from a Mott insulator to a *Aharonov-Bohm insulator*. The stiffness vanishes in both phases but the compressibility is finite only in the Aharonov-Bohm insulator. At a second critical point the system goes into a

superfluid phase. Most of the analysis is presented by using approximated analytical methods. These results will be checked against Monte Carlo simulations that we present in Sec. 3.3.4. The concluding remarks are summarized in Sec. 3.4.

3.1 $\mathcal{T}_3$ array definitions

For the basic definitions of the Bose-Hubbard model and its Quantum Phase version, we refer the reader to Ch.1. We introduce here only a more appropriate labelling of the lattice sites when the array is made up of sublattices, i.e. when the Bravais unit cell has a base. Indeed, the $\mathcal{T}_3$ lattice, represented in Fig.3.1, is not itself a Bravais lattice, but could be considered as a lattice with a base inside the conventional unitary cell (see Fig. 3.1) defined by the vectors

$$\mathbf{t_1} = \left(3/2; -\sqrt{3}/2\right) a \qquad \mathbf{t_2} = \left(3/2; +\sqrt{3}/2\right) a \ .$$

where a is the lattice constant. The lattice sites of the base are at positions

$$\mathbf{d_A} = (0;0)\, a \quad \mathbf{d_B} = (0;1)\, a \quad \mathbf{d_C} = (0;2)\, a \ .$$

The reciprocal lattice ($\mathbf{g_a} \cdot \mathbf{t_b} = 2\pi\delta_{a,b}$) vectors are defined as

$$\mathbf{g_1} = \frac{2\pi}{a}\left(1/3; -\sqrt{3}/3\right) \qquad \mathbf{g_2} = \frac{2\pi}{a}\left(1/3; +\sqrt{3}/3\right) \ . \tag{3.1}$$

In several situations it turns out to be more convenient to label the generic site i by using the position of the cell $\mathbf{t} = n_1\mathbf{t_1} + n_2\mathbf{t_2}$ ($-N_l \leq n_l < N_l$) and the position within the cell $\alpha = A, B, C$. In the rest of the chapter we either use the index i or the pair of labels $(\mathbf{t}, \alpha)$.

A generic observable W_i can be written henceforth as $W_\alpha(\mathbf{t})$. By imposing Born-Von Karman periodic boundary conditions its Fourier transform is given by

$$\widetilde{W}_\alpha(\mathbf{K}) = \frac{1}{\sqrt{4N_1N_2}} \sum_{\mathbf{t}} W_\alpha(\mathbf{t})\ e^{-\imath\mathbf{K}\cdot\mathbf{t}} \tag{3.2}$$

with $\mathbf{K} = k_1\mathbf{g_1} + k_2\mathbf{g_2}$ in the first Brillouin zone.

It is also useful to introduce a connection matrix $\mathcal{T}$ whose entries are non-zero only for islands connected by the hopping. More precisely $T_{\alpha,\gamma}(\mathbf{t},\mathbf{t}') = 1$ if site α of cell $\mathbf{t}$ is connected by a line (see Fig.3.1) to site γ of cell $\mathbf{t}'$ and $T_{\alpha,\gamma}(\mathbf{t},\mathbf{t}') = 0$ otherwise. The local coordination number is thus defined as $z_\alpha = \sum_{\mathbf{t}',\gamma} T_{\alpha,\gamma}(\mathbf{t},\mathbf{t}')$. It is $z = 6$ for the hubs (labelled by A) and $z = 3$ for the rims (labelled by B and C). For later convenience we also define the matrix $\mathcal{P}$ with elements

$$P_{\alpha,\gamma}(\mathbf{t},\mathbf{t}') \ = T_{\alpha,\gamma}(\mathbf{t}'-\mathbf{t})\ e^{\imath \mathbf{A}_{\alpha,\gamma}(\mathbf{t},\mathbf{t}')} \tag{3.3}$$

which includes the link phase factors which appear if the system is frustrated. In the whole paper we fix $k_B = \hbar = c = 1$.

In the next two subsections we give a brief description of the origin and characteristics of the coupling terms in the model Hamiltonians of Eqs.(1.18) - (1.6) . In addition we show how to realize optical lattices with $\mathcal{T}_3$ symmetry.

3.1.1 Josephson junction arrays

The charging energy which can be evaluated by assuming that each island has a capacitance to the ground C_0 and each junction a geometrical capacitance C. The electrostatic interaction between the Cooper pairs (charge $2e$) is defined as $\mathcal{U} = 4e^2\mathcal{C}^{-1}$, with capacitance matrix given by

$$\mathcal{C} = (C_0 + z_i C)\,\mathcal{I} - C\,\mathcal{T}\ . \tag{3.4}$$

Since both the connection and the capacitance matrices depend only on the distance between the cells (and on the base index of both sites), their space dependence can be simplified to

$$C_{\alpha,\gamma}(\mathbf{t},\mathbf{t}') = C_{\alpha,\gamma}(\mathbf{0},\mathbf{t}'-\mathbf{t}) \equiv C_{\alpha,\gamma}(\mathbf{t}'-\mathbf{t}) \tag{3.5}$$

We recall here that an estimate of the range of the electrostatic interaction is given by [40] $\lambda \approx \sqrt{C/C_0}$ and that the charge frustration n_0, assumed to be uniform, can be induced by an external (uniform) gate voltage $V_0 = n_0/8U_0$. From now on the energy and capacitance scale units will be put to $U_0 = e^2/2C_0$ and C_0 respectively. The experimental meaning is quite clear: these

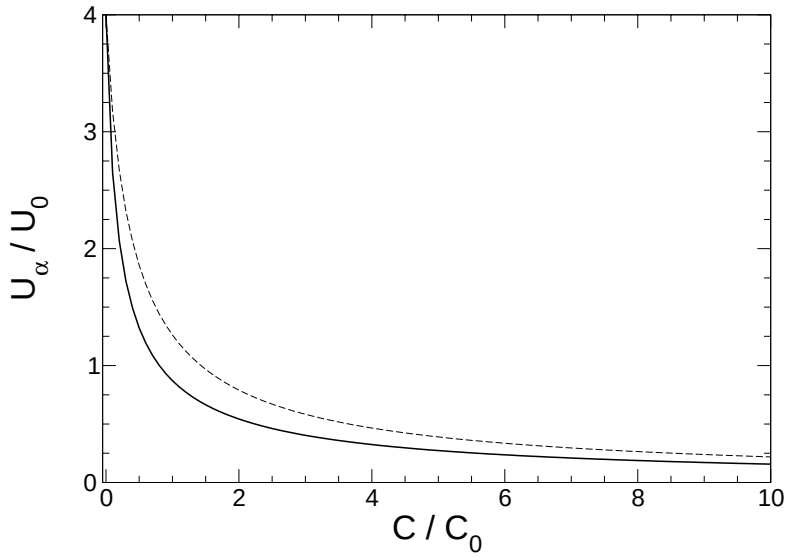

Figure 3.2: Electrostatic energy (in units of $U_0 = e^2/2C_0$) required to put an extra Cooper pair (for zero external charge) on an hub (straight line) and on a rim (dashed) as a function of the reduced capacitance C/C_0.

two parameters are fixed by the island size only, whereas the link capacitance C and Josephson energy t (or E_J) depend on the thickness of the junction much more easy to tune in the preparation of the sample. It is worth to stress here that the coupling parameters are fixed when the sample is built and can not be modified any longer. Thus the *phase transition* we are searching for can happen only under the action of external (magnetic or electric) fields.

Due to the particular structure of the $\mathcal{T}_3$ lattice, the charging energy of a single (extra) Cooper pair placed on a given islands *depends* on that site being a rim or a hub as shown in Fig.3.2. As a consequence quantum fluctuations of the phase of the superconducting order parameter may be different in the two different cases (rims or hubs). We will see in Sec.3.3.1 that this property is responsible for an additional modulation of the order parameter in the superconducting phase.

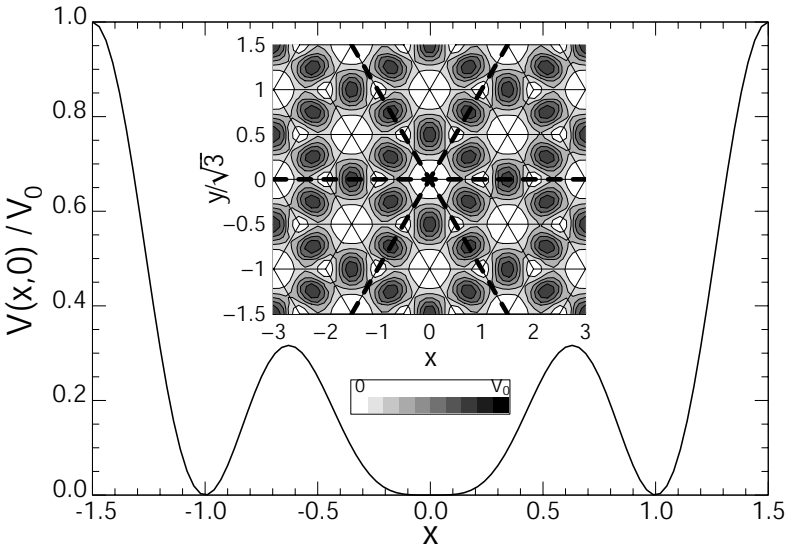

Figure 3.3: Optical potential with $\mathcal{T}_3$ symmetry generated by three counter-propagating laser beams. The inset shows the bidimensional contour plot while in the figure the details of the profile along a line connecting three sites (placed at positions $x = 1$, $x = 0$ and $x = -1$) is shown. The sites $x = -1, 1$ are rims while the site at $x = 0$ is a hub. Also here, as in the case of JJAs, the different form of the potential implies that the on-site energy U_0 is different for hubs and rims.

3.1.2 Optical lattices

Cold atoms loaded in optical lattices offer a concrete realization of the Bose-Hubbard model as explained in Sec. 1.1.2. The experimental test [16, 17] of the SI transition, predicted in [15], has finally opened the way to study strongly correlated phenomena in such systems. Very recently, several works addressed the possibility to induce frustration in optical lattices [61, 62, 63, 64]. For simplicity we will always refer to $\vec{A}$ as to the vector potential and we will use the magnetic picture also for optical lattices. It is therefore appealing to test the properties of the $\mathcal{T}_3$ lattice also with optical lattices once it is known how to create $\mathcal{T}_3$ lattices by optical means.

Here we propose [100] an optical realization of a $\mathcal{T}_3$ structure by means of three counter-propagating pairs of laser beams. These beams divide the plane in six sectors of width 60° (see the inset of Fig.3.3) and are linearly

polarized such to have the electrical field in the xy plane. They are identical in form, apart from rotations, and have wavelength equal to $\lambda = 3/2\,a$ (a is the lattice constant. Given a polarization of the x-propagating pair of lasers on the y-axis $\vec{E_1} = (0, E_y)$ the other two pairs are obtained by rotating $\vec{E_1}$ of 120° and −120° around the z-axis:

$$\begin{aligned} E_1(x,y) &= \left(0, \cos\left(\frac{4\,\pi\,x}{3}\right)\right) \\ E_2(x,y) &= \mathcal{R}\left(-\frac{2\pi}{3}\right).E_1\left(\mathcal{R}\left(\frac{2\pi}{3}\right).(x,y)\right) \\ E_3(x,y) &= \mathcal{R}\left(\frac{2\pi}{3}\right).E_1\left(\mathcal{R}\left(-\frac{2\pi}{3}\right).(x,y)\right) \end{aligned} \tag{3.6}$$

where $\mathcal{R}(\theta)$ is the rotation matrix of angle θ around the z-axis. The square modulus of the total field gives rise to the desired optical potential as it is shown in the inset of Fig.3.3.

The form of the potential landscape also in this case imposes that the on-site repulsion may be different for hubs and rims, since the width of the potential wells is different in the two cases (see main panel of Fig.3.3). It is however diagonal

$$\mathcal{U} = U_r\,\mathcal{I}_r + U_h\,\mathcal{I}_h \quad . \tag{3.7}$$

The subscript h, r denotes the respectively the hub and rim sites and $\mathcal{I}_{h,r}$ are the projectors on the corresponding sublattices.

3.2 Analytic approaches

The SI transition has been studied by a variety of methods; here we apply several of them to understand the peculiarities that emerge in the phase diagram due to the $\mathcal{T}_3$ lattice structure. The results that derive from these approaches will be presented in the next section.

The location of the critical point depends on the exact form and the range of $\mathcal{U}_{i,j}$. This issue is particulary interesting when discussing the role of electric frustration. In the paper we address the dependence of the phase boundary on the range of the interaction in the mean-field approximation.

The variational Gutzwiller ansatz and the strong coupling expansion will be analyzed only for the on-site case of Eq.(3.7). In the case of magnetic frustration the form of $\mathcal{U}_{i,j}$ leads only to quantitative changes so, also in this case, we discuss only the on-site case.

3.2.1 Mean field approach

The simplest possible approach to study the SI phase boundary consists in the evaluation of the superconducting order parameter, defined as

$$\psi_i = \langle e^{-\imath\varphi_i} \rangle \,, \tag{3.8}$$

by means of a mean-field approximation. By neglecting terms quadratic in the fluctuations around the mean field value, the hopping part of the Hamiltonian can be approximated as

$$\mathcal{H}_t^{(mf)} = -\frac{1}{2} \quad t \quad \sum_{i,j} e^{-\imath\varphi_i(\tau)} \; P_{i,j} \; \psi_j + h.c.$$

The order parameter is then determined via the self-consistency condition

$$\psi_i(\tau') = \frac{\mathrm{Tr}\left\{ e^{\imath\varphi_i(\tau')}\, e^{-\beta\,\mathcal{H}_U}\, \mathrm{T}_\tau \exp\left(\int_0^\beta \mathcal{H}_t^{(mf)}(\tau) \right) \right\}}{\mathrm{Tr}\left\{ e^{-\beta\,\mathcal{H}_U} \mathrm{T}_\tau \exp\left(\int_0^\beta \mathcal{H}_t^{(mf)}(\tau) \right) \right\}} \,. \tag{3.9}$$

In the previous equation, T_τ is the time-ordering in imaginary time τ and $\beta = 1/T$. The τ dependence of the operators is given in the interaction representation $W(\tau) = e^{\tau\,\mathcal{H}_U}\, W\, e^{-\tau\,\mathcal{H}_U}$. For simplicity we already assumed the order parameter independent on the imaginary time. One can indeed verify that this is the case in the mean-field approximation. Close to the phase boundary the r.h.s. of Eq. 3.9 can be expanded in powers of the order parameter and the phase boundary is readily determined.

A central quantity in the determining the transition is the phase-phase correlator

$$G_{i,j}(\tau) = \langle \mathrm{T}_\tau e^{\imath\phi_i(\tau)} e^{-\imath\phi_j(0)} \rangle_U \tag{3.10}$$

where the average is performed with the charging part of the Hamiltonian only. Charge conservation imposes that the indexes i, j are equal. The

Matsubara transform at $T = 0$ of the correlator reads

$$\widetilde{G}_{i,i}(\omega) = \int_{-\infty}^{\infty} G_{i,i}(\tau) e^{\imath\,\omega\,\tau} = \sum_{s=\pm} \frac{1}{\Delta E_{\alpha,s} - \imath s\omega} \tag{3.11}$$

where $\Delta E_{\alpha,\pm}$ are the excitation energies (for zero Josephson tunnelling) to create a particle (+) or a hole (-) on a site of the sublattice α where i lies.

In the case of the $\mathcal{T}_3$ lattice considered here even at zero magnetic field the order parameter is not uniform. The tripartite nature of the lattice results in a vectorial mean field ψ with one component for each sublattice. In the general case the linearized form of Eq.(3.9) can be rewritten as

$$\psi_\alpha(\mathbf{t}) = \frac{t}{2} \sum_\gamma \sum_{\mathbf{t}'} \widetilde{G}_{\alpha,\alpha}(0) P_{\alpha,\gamma}(\mathbf{t},\mathbf{t}') \psi_\gamma(\mathbf{t}') \tag{3.12}$$

that, due to the topology of the lattice is equivalent to

$$\psi_\alpha(\mathbf{t}) = \frac{t^2}{4} \widetilde{G}_{A,A}(0)\, \widetilde{G}_{B,B}(0) \sum_\gamma \sum_{\mathbf{t}'} P^2_{\alpha,\gamma}(\mathbf{t},\mathbf{t}') \psi_\gamma(\mathbf{t}')$$

The phase transition is identified with a non-trivial solution to this secular problem, i.e. one should determine π_{max}, the largest eigenvalue of P. This requirement translates in the following equation for the critical point:

$$t_{cr} = 2 \frac{\pi^{-1}_{max}}{\sqrt{\widetilde{G}_{A,A}(0) \widetilde{G}_{B,B}(0)}}\,. \tag{3.13}$$

In deriving the previous equation we used the fact that the sites B and C in the elementary cell (see Fig.3.1) have the same coordination number and therefore the phase-phase correlator is the same. In addition to the evaluation of the Matsubara transform at zero frequency of the phase correlator, one has to determine the eigenvalues of the gauge-link matrix $\mathcal{P}$. With a proper gauge choice [100] it is possible to reduce this matrix to a block diagonal form. For rational values of the frustration, $f = p/q$, by choosing $\mathbf{A} = (x - \sqrt{3}\, y)\, \frac{2\Phi_0}{\sqrt{3}a^2}\, f\, \hat{\mathbf{y}}$, the magnetic phase factors $\mathbf{A}_{i,j}(\mathbf{t},\mathbf{t}')$ (shown in Fig. 3.4) have a periodicity of $r \times 1$ elementary cells with $r = LCM(q,3)/3$. This implies that in the Fourier space (see Eq.(3.2)) the component k_2 is conserved and that k_1 is coupled only with the wavevectors $k_1^{(m)} = k_1 + 2\pi m/r$

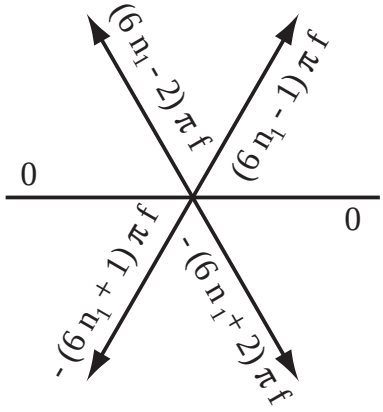

Figure 3.4: Magnetic phase pattern with the gauge choice $\mathbf{A} = (x - \sqrt{3}\, y)\, \frac{2\Phi_0}{\sqrt{3}a^2}\, f\, \hat{\mathbf{y}}$.

$(m = 0, ...r - 1)$. The determination of π_{max} is therefore reduced to the diagonalization of a $3r \times 3r$ matrix ($\widetilde{P}_{\alpha,\gamma}(k_1)$ is $r \times r$)

$$\widetilde{\mathcal{P}}(k_1, k_2) = \delta_{k_2,0} \begin{pmatrix} 0 & \widetilde{P}_{A,B}(k_1) & \widetilde{P}_{A,C}(k_1) \\ \widetilde{P}^{\dagger}_{A,B}(k_1) & 0 & 0 \\ \widetilde{P}^{\dagger}_{A,C}(k_1) & 0 & 0 \end{pmatrix} \tag{3.14}$$

with (k_1, k_2) belonging to the reduced Brillouin zone $\mathbb{B}_r = \{0 \leq k_i < 2\pi/r\}$.

The matrix $\mathcal{P}$ has r zero eigenvalues, and r pairs of eigenvalues equal in absolute value given by the reduced secular equation

$$\left[\widetilde{P}_{1,2}(k_1)\widetilde{P}^{\dagger}_{1,2}(k_1) + \widetilde{P}_{1,3}(k_1)\widetilde{P}^{\dagger}_{1,3}(k_1)\right]\ \widetilde{v}_1 = \pi^2\ \widetilde{v}_1$$

This simplification allows us to deal with $r \times r$ matrices instead of $q \times q$.

The inclusion of a finite range interaction, important only for Josephson arrays, leads to a richer lobe structure in presence of electrostatic frustration. The calculation of the lobes will be done within the mean field theory only.

3.2.2 Gutzwiller variational approach

A different approach, still mean-field in spirit, that allows to study the properties of the superconducting phase is the Gutzwiller variational ansatz

adapted to the Bose-Hubbard model by Rokhsar and Kotliar [112] The idea is to construct a variational wave-function for the ground state starting from the knowledge of the wave-function in the absence of the interaction term $\mathcal{H}_U$ in the Hamiltonian. In this case, and in absence of magnetic frustration, the ground state has all the phases aligned along a fixed direction θ. In the boson number representation it reads

$$|GS\rangle_{U=0} = \sum_{\{n_i\}} e^{\imath \sum_i n_i \theta} |\{n_i\}\rangle \tag{3.15}$$

A finite charging energy, tends to suppress the components of the state with large charge states, a variational state can then be constructed through the ansatz

$$|GS\rangle = \sum_{\{n_i\}} c_{n_1,\cdots,n_N} |\{n_i\}\rangle \tag{3.16}$$

where

$$c_{\{n_i\}} = \frac{1}{\sqrt{N_{GS}}} e^{\imath \sum_i n_i \theta} e^{-\sum_i \frac{K_i}{2}(n_i - \overline{n}_i)^2} . \tag{3.17}$$

In Eq.(3.17) N_{GS} is a normalization factor and K_i and $\overline{n}_i$ are variational parameter to be determined by minimizing the ground state energy. The Mott insulator is characterized by $K = \infty$, i.e. by perfect localization of the charges, $K = 0$ is the limit of zero charging, a finite value of K describes a superfluid phase where the phase coherence has been established albeit suppressed by quantum fluctuations.

3.2.3 Strong coupling perturbation theory

Both methods illustrated in Sections 3.2.1 and 3.2.2 are based on the analysis of the superconducting phase and on the determination of the phase boundary as the location of points where the superfluid order parameter vanishes. A complementary approach, which analyzes the phase boundary from the insulating side, was developed by Freericks and Monien [113]. The method was applied to the case of square and triangular lattices in Ref. [114] for the Bose-Hubbard model and in Ref. [115] for the quantum rotor model; it was then generalized to arbitrary topologies in Ref. [116]. In this section

we describe how to adapt the method to the $\mathcal{T}_3$ lattice. We will present the results of this analysis, particularly important for the fully frustrated case, in Sec. 3.3.3.

In the insulating phase the first excited state is separated by the ground state by a (Mott) gap. In the limit of vanishing hopping the gap is determined by the charging energy needed to place/remove an extra boson at a given lattice site. The presence of a finite hopping renormalizes the Mott gap which, at a given critical value, vanishes. The system becomes compressible, and the bosons, since are delocalized, will condense onto a superfluid phase. It is worth to emphasize that the identification of the SI boundary with the point at which the gap vanishes is possible as the bosons delocalize once the energy gap is zero. As we will see, in the case of $\mathcal{T}_3$ lattice the situation becomes more complex. In the presence of external magnetic frustration it may happen that though the Mott gap is zero, the states are localized and therefore the charges cannot Bose condense. In this cases between the Mott and superconducting region an additional compressible region (with zero superfluid stiffness) may appear. In order to keep the expressions as simple as possible we consider only the case of on-site interaction, though we allow a different U for hubs and rims as in Eq.(3.7). The possible existence of such a phase, however, does not depend on the exact form of $\mathcal{U}_{i,j}$. The strong coupling expansion is particularly useful for $\mathcal{T}_3$ lattice as it may help in detecting, if it does exist, the intermediate phase.

In the strong-coupling approach of Freericks and Monien the task is to evaluate, by a perturbation expansion in t/U, the energy of the ground and the first excited state in order to determine the point where the gap vanishes. We denote the ground and first excited levels by E_M^{gs} and E_M^{exc} respectively. The choice of the starting point for the perturbation expansion is guided by the nature of the low-lying states of the charging Hamiltonian. When $n_0 < 1/2$ (and in zero-th order in t/U) the ground state of the electrostatic Hamiltonian is ($n_i = 0\ \forall i$) and first excited level is given by a single extra charge localized on a site. Levels corresponding to charging a hub and a rim are nearly degenerate (i.e. $(U_r - U_h)/(U_r + U_h) \ll 1$, with the hub being lower in energy). As the strength of the hopping is increased, the insulating

gap decreases. We would like to stress, and this is an important difference emerging from the $\mathcal{T}_3$ topology, i.e. the location of the extra charge (on a hub or a rim) requires a different energy. This in turn has important consequences in the structure of the perturbation expansion.

Up to the second-order in the tunnelling, the ground state energy at $n_0 = 0$ is given by

$$E_M^{gs} = -\frac{2 \cdot 2N}{(U_h + U_r)/2} \frac{t^2}{4} \tag{3.18}$$

where N is the number of sites and $2N$ the number of hub-rim links in the lattice. Note that the first-order correction vanishes because the tunnelling term does not conserve local number of particles.

Due to nearly degeneracy of the excited levels, one is not allowed to perturb each of them independently but has to diagonalize the zeroth and the first order terms simultaneously. One has to diagonalize the following matrix:

$$\mathcal{Q}^{(1)} = \frac{1}{2}\mathcal{U} - \frac{t}{2}\mathcal{P} \tag{3.19}$$

This task can be reduced to the diagonalization of a $3r(f) \times 3r(f)$ matrix with a proper choice of the gauge (see Section 3.2.1).

For example, the (degenerate) lowest eigenvalue at $f = 1/2$ is

$$Q_{min}^{(1)}\Big|_{f=1/2} = \frac{U_h + U_r}{4} - \frac{1}{2}\sqrt{6t^2 + \left(\frac{U_r - U_h}{2}\right)^2}$$

which reduces to $U/2 - t\sqrt{6}/2$ in the case of perfectly degenerate charging energy. It must be stressed that all the energy bands are flat, independently of the values of the charging energies (it depends only on the peculiar $\mathcal{P}$ structure).

The second order perturbation term should be calculated on the lowest energy manifold: moreover only matrix elements between states of the same manifold are allowed. Nonetheless, it is simpler to write the different contributions in the usual basis of hub and rims (see Fig.(3.5)). The first excited state, to second order in tunnelling is given by

$$E_M^{(1)} = Q_{min}^{(1)} + \frac{t^2}{4} Q_{min}^{(2)} \tag{3.20}$$

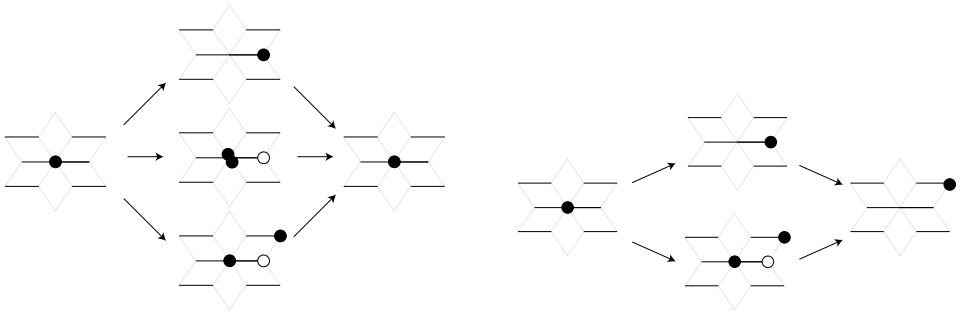

Figure 3.5: Intermediate charge states involved in the definition of Eq.(3.22). In the upper panel the contributions to the diagonal part are shown while in the lower panel there are the contributions to the off-diagonal part. The processes represented here are those contributing to the second order in the hopping amplitude. The black/white circles represent one extra +/- Cooper pair on a given site.

where $\mathcal{Q}^{(2)}$ is the second order matrix and can be split into separate submatrices on different sub-lattices, i.e.

$$\mathcal{Q}^{(2)} = \mathcal{Q}_h^{(2)}\,\mathcal{I}_h + \mathcal{Q}_r^{(2)}\,\mathcal{I}_r \tag{3.21}$$

Such a decomposition is possible because after two tunnelling events the boson come back to the initial sublattice.

$$\begin{aligned}\mathcal{Q}(2)_h &= z_h\frac{\mathcal{I}_h}{(U_h-U_r)/2} + z_h\frac{\mathcal{I}_h}{(U_h-(4U_h+U_r))/2} \\ &+ (2\cdot 2N - 2z_h)\,\frac{\mathcal{I}_h}{(U_h-(2U_h+U_r))/2} \\ &+ \frac{\mathcal{P}^2 - z_h\mathcal{I}_h}{(U_h-U_r)/2} + \frac{\mathcal{P}^2 - z_h\mathcal{I}_h}{(U_h-(2U_h+U_r))/2}\end{aligned} \tag{3.22}$$

($\mathcal{Q}(2)_r$ is defined in a similar way) where $\mathcal{I}_{h,r}$ are the projectors on the hub and rim sublattices. After some algebra and by changing basis to the one composed by the eigenvectors of Eq.(3.19), one gets the first excited energy level. The task is now to determine the location of points at which the gap, given by the difference of Eq.(3.20) and Eq.(3.18), vanishes. It is worth to stress that the thermodynamically divergent contributions wash out exactly their analogous in the ground state expression of Eq.3.18.

We discuss the results deriving from this approach in the next Section where we analyze the phase diagram.

3.3 Phase diagram

In order to keep the presentation as clear as possible we first discuss the main features of the phase diagram by means of the analytical approaches introduced before. We will then corroborate these results in a separate section by means of the Monte Carlo simulations.

The value of the critical Josephson coupling as a function of the range of the electrostatic interaction, in the absence of both electric and magnetic frustration is discussed first. The effect of frustration, either electric or magnetic will then be discussed in two separate sections. In the case of electrical frustration the topology of a $\mathcal{T}_3$ lattice gives rise to a rather rich lobe structure, the overall picture is nevertheless very similar to the one encountered in the square lattice. Much more interesting, as one would suspect, is the behaviour of the system as a function of the magnetic frustration. The location of the phase boundary shows the characteristic butterfly shape with an *upturn* at fully frustration typical of the $\mathcal{T}_3$. In addition, at $f = 1/2$, a very interesting point which emerges from our analysis is the possibility of an intermediate phase, the Aharonov-Bohm insulating phase, separating the Mott insulator from the superfluid.

3.3.1 Zero magnetic & electric frustration

A first estimate for the location of the phase boundary can be obtained by means of the mean-field approach described in Sec. 3.2.1. The results coincide with the first-order perturbative calculation introduced in Sec. 3.2.3 and with the Gutzwiller variational approach of Sec. 3.2.2. In absence of frustration the $\mathbf{K} = \mathbf{0}$ mode corresponds to the maximum eigenvalue of the matrix $\mathcal{P}$ ($\pi_{max} = \sqrt{18}$) and the transition point is given by

$$t_{cr} = \frac{1}{6\sqrt{2}} \sqrt{\widetilde{U}_{A,A}(\mathbf{0})\, \widetilde{U}_{B,B}(\mathbf{0})} \tag{3.23}$$

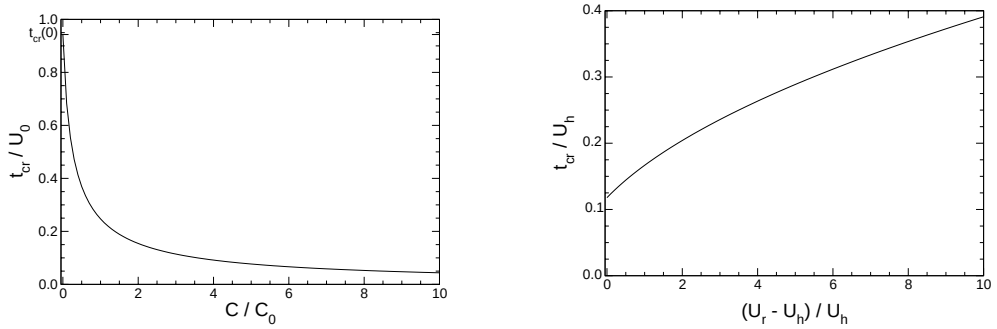

Figure 3.6: Josephson arrays (left): dependence of the critical point at $f = 0$ on the range of the Coulomb repulsion determined by the ratio C/C_0. Optical lattices (right): dependence of the transition point on the difference repulsion in the hubs and the rims.

In the limit of on-site uniform ($U_r = U_h = 8U_0$) the SI transition occurs at the value $t_{cr}/U_0 = 2\sqrt{2}\,/3 \approx 0.943$ very close to the mean field value for a square lattice $t_{cr}/U_0 = 1$ (in both lattices the average value of nearest neighbours is 4). In the case of a Josephson array the transition point depends on the range of the interaction. In the (more realistic) case of a finite junction capacitance an analytic form is not available and the numerical phase boundary is shown in Fig. 3.6 as a function of the ratio C/C_0. In the case of optical lattices, see Eq.(3.7), the repulsion is on-site. There is still a weak dependence of the transition on the difference $U_r - U_h$. As it is shown in Fig. 3.6, this dependence is not particularly interesting and in the Monte Carlo simulation we will ignore it.

As already mentioned, a characteristic feature that emerges in $\mathcal{T}_3$ lattices, even in the absence of magnetic frustration, is that the superfluid order parameter is not homogeneous. This can be already seen from the eigenvector corresponding to the solution of Eq.(3.23). Near the transition point the ratio between the order parameter value on hubs and rims is constant and is related to the ratio of the on-site repulsions $|\psi_h/\psi_r| \simeq \sqrt{z_h U_r / z_r U_h}$. Phase localization is more robust on hubs ($z_h = 6$) than on rims ($z_r = 3$) because of the larger number of nearest neighbours. In order to better understand the modulation of the order parameter we analyzed the properties of the

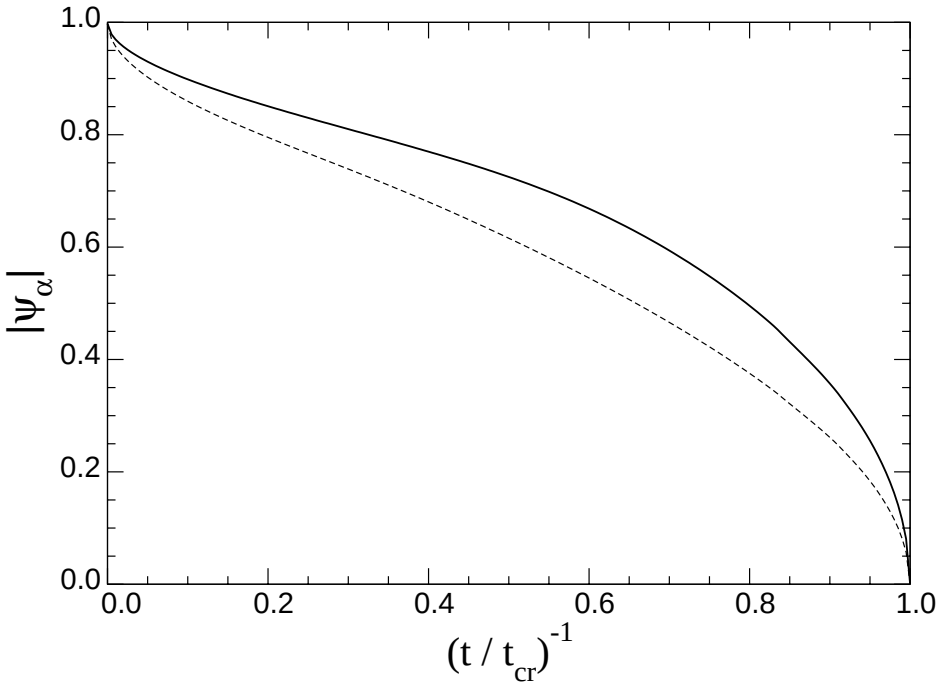

Figure 3.7: Modulation of the order parameter for zero frustration, ψ_{hub} (straight) is always higher than ψ_{rim} (dashed). The curves are obtained by means of the Gutzwiller variational approach.

superconducting phase using the variational approach exposed in Sec. 3.2.2 (which allows us to study the behaviour of ψ also far from the transition).

As it can be clearly seen from Fig.3.7, quantum fluctuations have a stronger effect on the rims than hubs due to the different coordination number of the two sublattices. Note that this is a pure quantum mechanical effect, in the classical regime all phases are well defined and $|\psi_{hub}| = |\psi_{rim}| = 1$. The transition point (as it was implicit in the previous discussion) is the same for both sublattices: there is no possibility to establish phase coherence between rims if the hub-network was already disordered (and viceversa).

3.3.2 Electric frustration

When an external uniform charge frustration is present (see Sec. 1.2.2), the array cannot minimize the energy on each site separately, hence frustration arises. The behaviour of the transition point as a function of the offset charge shows a typical lobe-structure [36, 66]. At the mean-field level all the information to obtain the dependence of the phase boundary on the chemical potential (gate potential for Josephson arrays) is contained in the zero-frequency transform of the Green functions G in Eq.(3.13). The calculation of the phase-phase correlators, defined by Eq.(3.10), is determined, at $T = 0$, once the ground and the first excited states of $\mathcal{H}_U$ is known. As all the observables are periodic of period one in the offset charge n_0 and are symmetric around $n_0 = 0$, the analysis can be restricted to the interval $[0, 1/2]$. *Ground state* charge configuration in the case of some values of the electric frustration are shown in Fig.3.8.

Progressively on increasing the external charge, the filling factor increases as well. In the case of finite range charging interaction also Mott lobes with fractional fillings appear [66]. An analytical determination of the ground state of the charging Hamiltonian for generic values of the external charge is not available. We considered rational fillings of the whole lattice as made up of periodic repetitions of a partially filled super-cell of size comparable with the range of the interaction $\mathcal{U}_{i,j}$ and then constructed a Wigner crystal for the Cooper pairs with this periodicity. For $C/C_0 \leq 1$ a 3×3 super-cell turns out to be sufficient. Given a certain rational filling p/q, the corresponding charging energy is given by

$$E_{\{n_i\}}(\frac{p}{q}, n_0) = 3N \frac{e^2}{C_0} \left(n_0^2 - 2\frac{p}{q} n_0 + \frac{C_0}{N} \sum_{i,j} n_i \mathcal{C}_{i,j}^{-1} n_j \right)$$

where N is the number of cells in the system and $\{n_i\}$ is the particular realization of the filling. This defines a set of parabolas which allow to determine the sequence of ground states. It is evident that, for fixed p/q filling, the optimal configuration is the one that exhibits longer average distance between particles. The variation of the ground state configurations as a function of gate charge gives to the phase boundary a characteristic structure made of

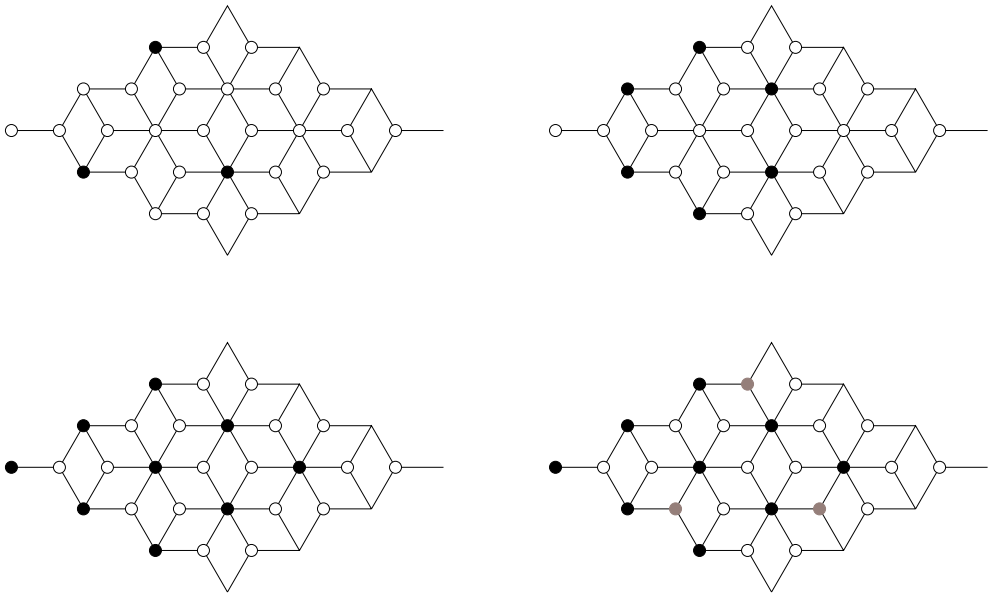

Figure 3.8: Ground state configurations of the charges (i.e. at $t = 0$) for filling $1/9, 2/9, 1/3, 4/9$. The different ground states occurs on increasing the value of the external charge n_0 The black circles denote those sites that are occupied by one Cooper pair. The ground state configurations are responsible for the behaviour of the phase correlator and hence of the lobe-like structure, Fig.3.9, of the phase diagram.

lobes, as shown in Fig. 3.9. The longer is this range of the electrostatic interaction the richer is the lobe structure.

As can be seen in Fig. 3.9 when the interaction is purely on-site there is only one lobe that closes at half filling when the degeneracy between the empty ground state and the extra-charged one leads to superconductivity for arbitrarily small t. As soon as the range becomes finite, other fillings come into play. An interesting feature typical of the $\mathcal{T}_3$ lattice is that at $n_0 = 1/2$ the half filled state is not the ground state (see Fig. 3.9).

Finally, we recall that the presence of the offset breaks the particle-hole symmetry and thus the universality class of the phase transition change [36]. This can be seen from the expansion at small ω of the correlator (Eq. 3.11) that enters the quadratic term of the Wilson-Ginzburg-Landau functional.

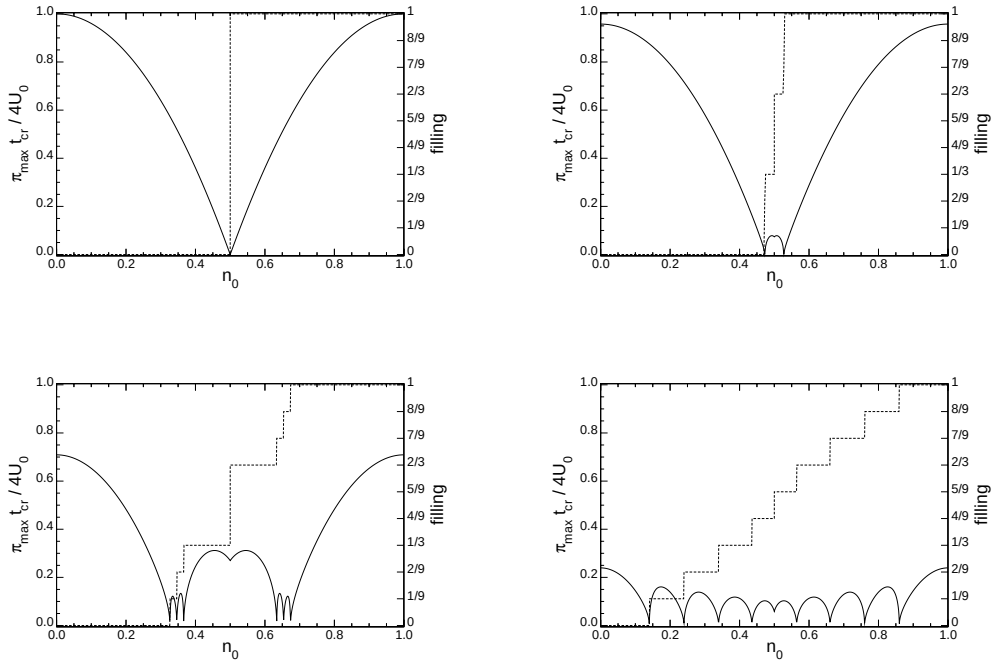

Figure 3.9: Lobe structures at different values of the capacity, i.e. electrostatic range (respectively $C = 0, 10^{-2}, 10^{-1}, 1$). The dashed lines point out the discrete filling of the ground state. Pictures on the right are magnifications of the highlighted areas in the left ones.

With n_0 also terms linear in ω enter the expansion and the dynamical exponent z changes from 1 to 2.

3.3.3 Magnetic frustration and Aharonov-Bohm insulating phase

The outgrowing interest in $\mathcal{T}_3$ lattices is especially due to their behaviour in the presence of an externally applied magnetic field. The presence of a magnetic field defines a new length scale, the magnetic length. The competition between this length and the lattice periodicity generates interesting phenomena such as the rising of a fractal spectrum à la Hofstadter. In $\mathcal{T}_3$ lattices perhaps the most striking feature is the complete localization in a fully frustrating field ($f = 1/2$). This is due to destructive interference along

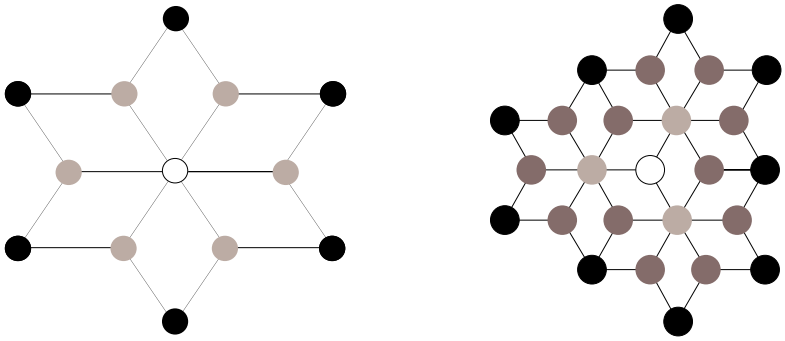

Figure 3.10: Aharonov-Bohm cages. Particles that starts on white sites can't go further than black sites, due to destructive interference. In fact, $f = 1/2$ means π phase shift around a plaquette. In square lattices this could not happen because of the escape opportunity given by straight lines.

all paths that particles could walk on, when the phase shift around a rhombic plaquette is π (see Fig. 3.10). Is there any signature of this localization (originally predicted for tight-binding models) in the quantum phases transition between the Mott and the superconducting phases? This is what we want to investigate in this section.

In order to determine the phase boundary at $T = 0$ we can follow either the mean field approach of Sec. 3.2.1 or the perturbative theory presented in Sec. 3.2.3. We remind that while the first approach signals the disappearance of the superfluid phase, the perturbation expansion indicates where the Mott phase ends. The results of both approaches are shown in Fig. 3.11. Commensurate effects are visible in the phase boundary of Fig. 3.11 at rational fractions $f = p/q$ of the frustration. The results presented are quite generic. We decided to show, as a representative example, the results for a JJ array with capacitance ratio $C/C_0 = 1$ and an optical lattice with $U_r - U_h = 0.5U_h$. The peak at $f = 1/2$, characteristic of the $\mathcal{T}_3$ lattice is due to the presence of the Aharonov-Bohm cages.

Although there is a difference between the mean-field and the strong coupling calculation, they both confirm the same behaviour. A very interesting point however emerges at half-filling. It is worth to stress again that while the

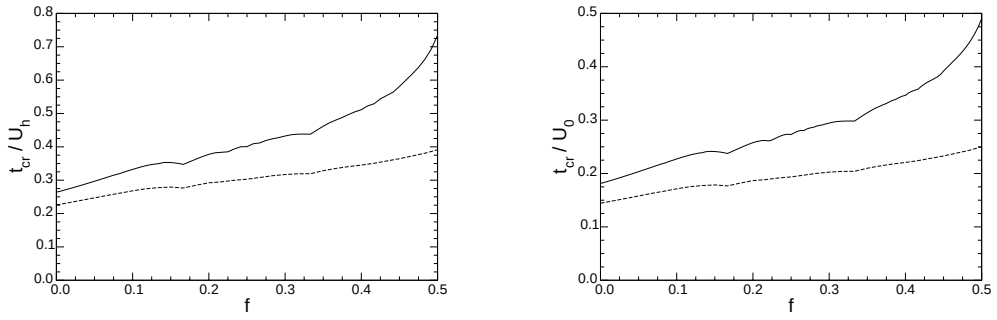

Figure 3.11: Phase boundary in presence of a magnetic field in $\mathcal{T}_3$: straight line is the perturbative result, mean field is dashed. Left: JJAs with $C/C_0 = 1$; right: optical lattices with $U_r - U_h = 0.5U_h$. Note the highly pronounced peak at $f = 1/2$ in contrast to the square lattice case.

mean-field shows the disappearance of the superconducting phase, the strong coupling expansion indicates where the Mott gap vanishes and hence charges can condense. The vanishing of the gap can be associated to boson condensation *only* if bosons are delocalized. This is the case for the whole range of frustrations except at $f = 1/2$. In the fully frustrated case the excitation gap *vanishes* but the excited state (the extra boson on a hub) still remains localized due to the existence of the Aharonov-Bohm cages. This may lead to the conclusion that at fully frustration there is an intermediate phase where the system is *compressible* (the Mott gap has been reduced to zero) with *zero superfluid density* (the bosons are localized in the Aharonov-Bohm cages).

At this level of approximation there is no way to explore further this scenario. In order to assess the existence of the intermediate phase a more accurate location of the phase boundaries is necessary. We will discuss the possible existence of the *Aharonov-Bohm insulator* by means of Monte Carlo simulations in the next section.

3.3.4 MonteCarlo methods

The simulations are performed on an effective classical model obtained after mapping the Quantum Phase model of Eq.(1.6) onto a $(2 + 1)$ XY

model. Our main interest in performing the Monte Carlo simulation is to look for signatures of the Aharonov-Bohm insulator. As its existence should not depend on the exact form of the repulsion $\mathcal{U}_{i,j}$ we chose the simplest possible case in which the repulsion is on-site and $U_h \sim U_r$. The details of the mapping are described in Refs. [106, 107] and are briefly reviewed in App.A. The effective action $\mathcal{S}$ (at zero charge frustration) describing the equivalent classical model is

$$\begin{aligned} \mathcal{S} &= K \sum_{\langle i,\, j\rangle,\, k} \left[1 - \cos\left(\varphi_{i,k} - \varphi_{j,k} - A_{i,j}\right)\right] \\ &+ K \sum_{i,\, \langle k,\, k'\rangle} \left[1 - \cos\left(\varphi_{i,k} - \varphi_{i,k'}\right)\right] \ . \end{aligned} \tag{3.24}$$

where the coupling K is $\sqrt{t/U}$. The index k labels the extra (imaginary time) direction which takes into account the quantum fluctuations. The simulations where performed on $L \times L \times L_\tau$ lattice with periodic boundary conditions. The two correlation lengths (along the space and time directions) are related by the dynamical exponent z through the relation $\xi_\tau \sim \xi^z$. For zero magnetic frustration, because of the particle-hole symmetry (we consider only the case $n_0 = 0$) holds $z = 1$. As we will see this seems not to be the case at fully frustration because of the presence of the Aharonov-Bohm cages.

The evaluation of the various quantities have been obtained averaging up to 3×10^5 Monte Carlo configurations for each one of the 10^2 initial conditions, by using a standard Metropolis algorithm. Typically the first 10^5 were used for thermalization. The largest lattice studied was $24 \times 16 \times 24$ at fully frustration and $48 \times 48 \times 48$ at $f = 0$. This difference is due to the much larger statistics which is needed to obtain sufficiently reliable data. While in the unfrustrated case we took a cube of length L in the fully frustrated case it turned out to be more convenient to consider (but will discuss other lattice shapes) an aspect ratio of 2/3. With this choice the equilibration was simpler probably due to a different proliferation of domain walls[97, 98].

In order to characterize the phase diagram we studied the superfluid stiffness and the compressibility of the Bose-Hubbard model on a $\mathcal{T}_3$ lattice. The

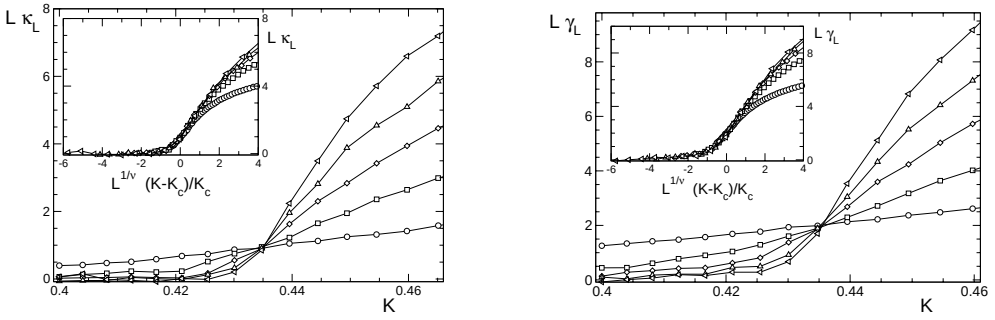

Figure 3.12: $f = 0$: a)Scaling (main) and data collapse (inset) of the compressibility for the unfrustrated case. b)The same as in a) for the superfluid stiffness. All the systems have aspect ratio $L_\tau = L_y = L_x$ with $L_\tau = 6$ (circles), 12 (squares), 18 (diamonds), 24 (triangles up), 30 (triangles down).

phase stiffness Γ has been defined in the previous chapter in Eq.(2.3) and is related to the free energy $\mathcal{F}$ change if one imposes a phase twist θ across the system in a spatial direction, $\Gamma = \partial^2\mathcal{F}/\partial\theta^2$. The compressibility, κ, is defined by $\kappa = \partial^2\mathcal{F}/\partial V_0^2$ where V_0 the chemical potential for the bosons. By employing the Josephson relation in imaginary time, see Ref.[107], the compressibility can be expressed as the response of the system to a twist in imaginary time, $\varphi_{i,k} \to \varphi_{i,k} + \theta_\tau\, k$, i.e.

$$\kappa = \left.\frac{\partial^2\mathcal{F}(\theta_\tau)}{\partial\theta_\tau^2}\right|_{\theta_\tau=0} \quad . \tag{3.25}$$

In the case of unfrustrated system we expect that the transition belongs to the $3D-XY$ universality class. Close to the quantum critical point $\kappa \sim \xi^{-1}$, the corresponding finite size scaling expression for the compressibility reads

$$\kappa = L^{-(d-z)}\,\widetilde{\kappa}\left(L^{1/\nu}\,\frac{K-K_c}{K_c},\,\frac{L_\tau}{L^z}\right) \tag{3.26}$$

An analogous expression holds for the finite size-scaling behaviour of the stiffness

$$\gamma = L^{-(d+z-2)}\,\widetilde{\gamma}\left(L^{1/\nu}\,\frac{K-K_c}{K_c},\,\frac{L_\tau}{L^z}\right) \tag{3.27}$$

The expected exponent is $\nu = 2/3$ as it is known from the properties of the three-dimensional XY model.

The results of the simulations for the compressibility and for the stiffness are reported in Fig.3.12. Finite size scaling shows that the SI transition occurs at

$$K_c = 0.435 \pm 0.0025 \quad . \tag{3.28}$$

As expected the unfrustrated case follows remarkably well the standard picture of the Superfluid-Mott Insulator quantum phase transition. In the absence of the magnetic field the system defined by Eq.(3.24) is isotropic in space-time and therefore the stiffness and the compressibility have the same scaling and critical point.

The situation changes dramatically in the fully frustrated system. In this case an anisotropy in space and time directions arises because of the presence of the applied magnetic field which frustrates the bonds in the space directions (see the r.h.s of Eq.(3.24)). This field induced anisotropy is responsible for the different behaviour of the system to a twist in the time (compressibility) or space (stiffness) components.

As already observed in the classical case [98], the Monte Carlo dynamics of frustrated $\mathcal{T}_3$ systems becomes very slow. This seems to be associated to the presence of zero-energy domain walls first discussed by Korshunov in Ref. [97]. This issue is particulary delicate for the superfluid stiffness. In this case the longest simulations had to be performed. Moreover in order to alleviate this problem we always started the run deep in the superfluid state and progressively increased the value of the Hubbard repulsion U. Also the choice of the lattice dimensions turned out to be important. We made the simulations on $12 \times 8 \times 12$, $18 \times 12 \times 18$, and $24 \times 16 \times 24$ systems and found out that by choosing this aspect ratio along the x and y directions thermalization was considerably improved.

The results of the simulations are reported in Fig.3.13 for the compressibility and for the stiffness. As it appears from the raw data of the figure it seems that the points at which the compressibility and the stiffness go to zero are different. An appropriate way to extract the critical point(s) should

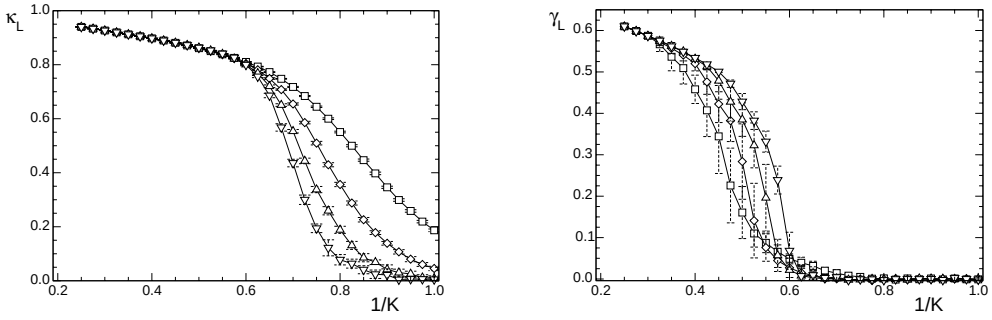

Figure 3.13: $f = 1/2$:Compressibility (upper panel) and stiffness (lower panel) assuming the aspect ratio $L \times L \times 2L/3$. Different symbols corresponds to $L = 12$ (circles), 18 (squares), 24 (triangles up), and 30 (triangles down).

be by means of finite size scaling.

As a first attempt we assumed that the transition is in the same universality class as for the unfrustrated case and we scaled the data as in Fig.3.12. Although the scaling hinted at the existence of two different critical points for the Mott to Aharonov-Bohm insulator and for the Aharonov-Bohm insulator to superfluid transitions respectively, the quality of the scaling points was poor. In our opinion this observation may suggest that the scaling exponents for the fully frustrated case are different as the one for the direct Mott Insulator to Superfluid phase transition at $f \neq 1/2$. In order to extract more tight bounds on the existence of this phase we analyzed the size dependence of the observables without any explicit hypothesis on the scaling exponent (which we actually do not know). The results are presented in Fig.3.14. The data of Fig.3.14 seem to indicate that there is a window

$$0.65 \leq K^{-1} \leq 0.7$$

where the system is compressible but not superfluid! This new phase, the Aharonov-Bohm insulator, is the result of the subtle interplay of the $\mathcal{T}_3$ lattice structure and the frustration induced by the external magnetic field. Our simulations cannot firmly determine the existence of two separate critical points since we were not able to improve their accuracy and study larger lattices. However we think that, by combining both the analytical results

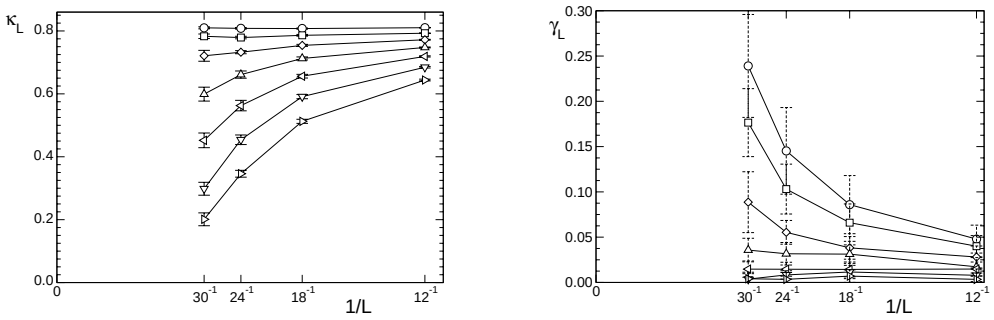

Figure 3.14: $f = 1/2$: Compressibility (upper panel) and the stiffness (lower panel) as a function of the L_t size of the system for different values of K. Data corresponds to $1/K = 0.6$(circles), 0.625(squares), 0.65(diamonds), 0.675(triangles up), 0.7(tr. left), 0.725(tr. down), 0.75(tr. right).

and the Monte Carlo data we have a possible scenario for the phase diagram of the frustrated BH model on a $\mathcal{T}_3$ lattice.

Further evidence of the existence of the AB cages can be obtained by analyzing the anisotropy in space and time directions of the phase correlations. For this purpose we considered the compressibility as a function of L and L_τ separately. The idea is that because of the AB cages the correlations are short-ranged in the space directions (bosons are localized) while there are longer ranged correlations in the time direction. Indeed the dependence of the compressibility on the system dimensions is strong when one changes L_τ while it is rather weak when the space dimensions are varied as shown in Fig.3.15. This hints at the fact that the Aharonov-Bohm phase is a phase in which the gap has been suppressed (correlation in the time dimension) but where the bosons are localized (short-range correlations in space).

The Monte Carlo simulations just discussed provide evidence for the existence of a new phase between the Mott insulator and superfluid. Due to the finite size of the system considered and to the (present) lack of a scaling theory of the two transitions, we cannot rule out other possible interpretations of the observed behaviour of the Monte Carlo data. A possible scenario which is compatible with the simulations (but not with the result of the per-

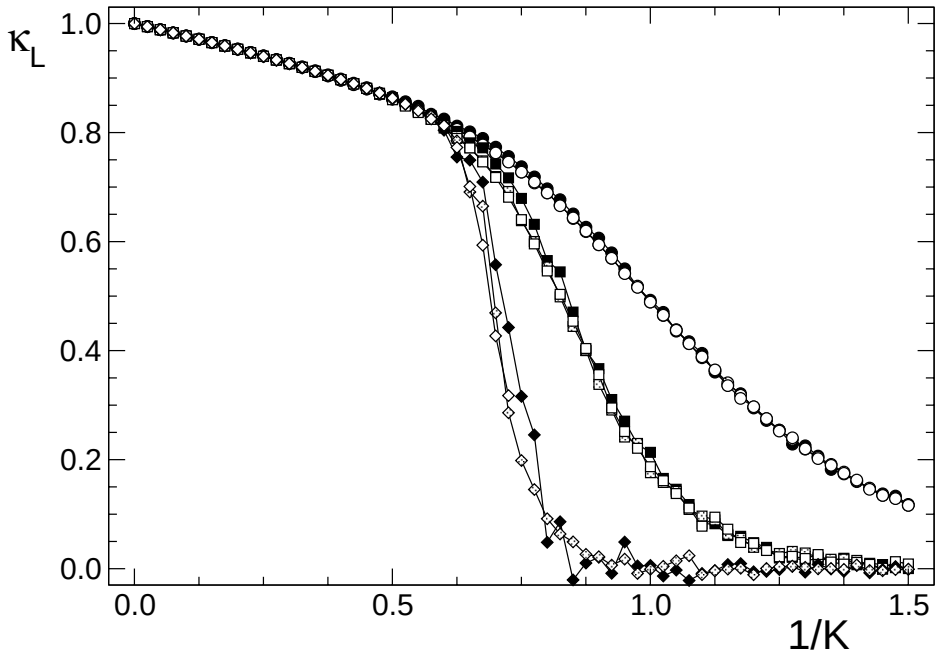

Figure 3.15: Compressibility as a function of $K = \sqrt{t/U}$ for different values of the system sizes. Different symbols corresponds to different lengths L_τ in the time dimension: 6 (circles), 12 (squares), and 30 (diamonds). Different fillings are different spatial sizes $L_x \times L_y$: 6×4 (black), 12×8 (gray), and 18×12 (white). The compressibility depends strongly on L_τ but very weakly on $L_x \times L_y$.

turbation expansion [1]) is that a single thermodynamic transition is present in the $2+1$ dimensional system but the phase coherence is established in a two step process. First the system becomes (quasi) ordered along the time direction, then, upon increasing the hopping the residual interaction between these "quasi-one-dimensional" coherent tubes go into a three-dimensional coherent state driven by the residual coupling between the tubes. In more physical terms the "tubes" represent the boson localized in the AB cages and the residual hopping is responsible for the transition to the superfluid state. This means that the intermediate state that we observe is due to a one- to

[1] In the perturbation expansion, the eigenfunction corresponding to the excited state is localized in space. Therefore one should not expect any condensation to a superfluid state.

three-dimensional crossover that takes place at intermediate couplings.

3.4 Conclusions

In this Chapter we exploited several methods, both analytic and numerical, in order to determine the phase diagram of a Bose-Hubbard model on a $\mathcal{T}_3$ lattice. Differently from previous studies on $\mathcal{T}_3$ networks we analyzed the situation where the repulsion between bosons (or Cooper pairs for Josephson arrays) becomes comparable with the tunnelling amplitude (Josephson coupling in JJAs) leading to a quantum phase transition in the phase diagram. Up to now the attention on experimental implementations has been confined to Josephson networks. As discussed in Sec. 3.1.2, the $\mathcal{T}_3$ lattice can also be realized in optical lattices. The possibility to experimentally study frustrated $\mathcal{T}_3$ optical lattices open the very interesting possibility to observe subtle interference phenomena associated to Aharonov-Bohm cages also with cold atoms. Having in mind both the realization in Josephson and optical arrays, we studied a variety of different situations determined by the range of the boson repulsion including both electric and magnetic frustration. Although in the whole paper we concentrated on the $T = 0$ case, in this discussion we will also comment on the finite temperature phase diagram.

The peculiarity of the lattice symmetry already emerges for the unfrustrated case. The superfluid phase is not uniform but it has a modulation related to the presence of hubs and rims with different coordination number. As a function of the chemical potential (gate charge) the transition has a quite rich structure due to the different boson super-lattices which appear as the ground state.

As a function of the magnetic field the SI transition has the characteristic butterfly form. In the fully frustrated case, however, the change is radical and we find indications that the presence of the Aharonov-Bohm cages can lead to the appearance of a new phase, the Aharonov-Bohm insulator. This phase should be characterized by a finite compressibility and zero superfluid stiffness. A sketch of the possible phase diagram is shown in Fig.3.16. With the help of Monte Carlo simulations we were able to bound the range of

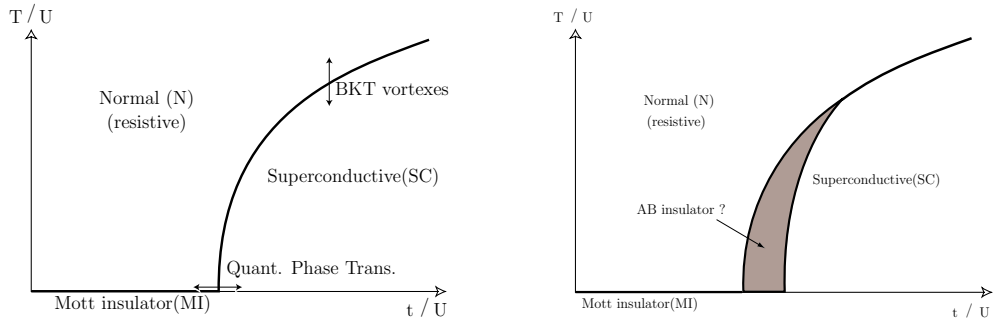

Figure 3.16: A possible phase diagram of an array with $\mathcal{T}_3$ lattice. In the unfrustrated case (upper panel) we sketch the standard phase diagram which leads at $T = 0$ to the SI transition. On the lower panel we present a possible scenario that emerges from our work. An new phase appears separating the normal from the superfluid phases.

existence of the new phase. Unfortunately we have to admit that our results are not conclusive and, as discussed in the previous section, an alternative scenario is also possible. Nevertheless, we think that the existence of an intermediate phase is a very appealing possibility worth to being further investigated.

How is it possible to experimentally detect such a phase? In Josephson arrays, where one typically does transport measurement, the AB-insulator should be detected by looking at the temperature dependence of the linear resistance. On approaching the zero temperature limit, the resistance should grow as T^δ differently from the Mott insulating phase where it has an exponential activated behaviour. In optical lattices the different phases can be detected by looking at the different interference pattern (in the momentum density or in the fluctuations [49]). A detailed analysis of the experimental probe will be performed in future studies.

There are several issues that remain to be investigated. It would be important, for example, to see how the phase diagram of the frustrated system (and in particular the Aharonov-Bohm phase) is modified by a finite range of $\mathcal{U}_{i,j}$ and/or the presence of a finite chemical potential. An interesting possibility left untouched by this work is to study the fully frustrated array at

$n_0 = 1/2$. In this case (for on-site interaction) the superfluid phase extends down to vanishing small hopping. In this case a more extended AB insulating phase could be more favoured, and thus more clearly visible.

Chapter 4

Spin-1 bosons on one-dimensional lattices

As yet explained in Sec. 1.1.2, the experimental realization of optical lattices has paved the way to study strongly correlated many-particle systems with cold atomic gases. The main advantages with respect to condensed matter systems lie on the possibility of a precise knowledge of the underlying microscopic models and an accurate and relatively easy control of the various couplings. More recently the use of far-off-resonance optical traps, has opened the exciting possibility to study spinor condensates [14]. In particular Bose condensation has been achieved in alkali atoms with nuclear spin $I = 3/2$ that have three low energy hyperfine states and therefore behave as $T = 1$ particles. Importance of using optical lattices to study the quantum spin phenomena can be understood from the following example. For particles with anti-ferromagnetic interactions, such as ^{23}Na, the exact ground state of an even number of particles in the absence of a magnetic field is a spin singlet described by a rather complicated correlated wave function [117]. Various properties of such condensate in a single trap were investigated [117, 118, 119, 120, 121, 122]. When the number of particles in the trap is large, the energy gap separating the singlet ground state from the higher energy excited states is extremely small, and the precession time of the classical mean-field ground state can be of the order of the trap lifetime.

So, experimental observation of the quantum spin phenomena in such systems is very difficult. To amplify quantum spin effects one would like to have a system with smaller number of particles and stronger interactions between atoms. Hence it is natural to consider the idea of loading these spinor bosons into an optical lattice, in which one can have a small occupation number per site (in experiments of Ref. [17] this number was around 1-3) and relatively strong interactions between atoms.

The appropriate Hamiltonian to describe such systems is given by the sum of Eq.(1.18) and (1.24):

$$\begin{aligned} \widehat{\mathcal{H}} &= \frac{U_0}{2}\sum_i \widehat{n}_i(\widehat{n}_i-1) + \frac{U_2}{2}\sum_i \left(\widehat{\mathbf{S}}_i^2 - 2\widehat{n}_i\right) - \mu\sum_i \widehat{n}_i \\ &- t\sum_{i,\sigma}\left(\widehat{b}^\dagger_{i,\sigma}\widehat{b}_{i+1,\sigma} + \widehat{b}^\dagger_{i+1,\sigma}\widehat{b}_{i,\sigma}\right) , \end{aligned} \tag{4.1}$$

where the operator $\widehat{a}^\dagger_{i,\sigma}$ creates a boson in the lowest Bloch band localized on site i and with spin component σ along the quantization axis. The operators $n_i, \mathbf{S}_i$ are the total particles number and spin on a site, respectively. The uniqueness of the completely symmetric state with fixed spin and number makes it possible to denote the single site states with $|n_i, S_i, S_i^z\rangle$ (S_i^z is the z-projection of the i-th spin); the constraint $S_i + n_i =$ even must be satisfied (see Sec.1.1.2).

Spin effects are enhanced by the presence of strong interactions and small occupation number, thus resulting in a rich variety of phases characterized by different magnetic ordering. For spin-1 bosons it was predicted that the Mott insulating phases have nematic singlet [123] or dimerized [124] ground state depending on the mean occupation and on the value of the spin exchange. Since the original paper by Demler and Zhou [123] several works have addressed the properties of the phase diagram of spinor condensates trapped in optical lattices (see [125, 126, 127, 128, 129, 130] and references therein). The increasing attention in spinor optical lattices has also revived the attention on open problems in the theory of quantum magnetism. The spinor Bose-Hubbard model, when the filling corresponds to one boson per site, can be mapped onto the $S = 1$ Heisenberg model with biquadratic interactions

which exhibits a rather rich phase diagram including a long debated nematic to dimer quantum phase transition [131, 132, 133, 134, 135, 136, 137, 138].

Up to now the location of the phase boundary of the spinor Bose-Hubbard model has been determined by means of mean-field and strong coupling approaches. A quantitative calculation of the phase diagram is however still missing. This might be particularly important in one dimension where non-perturbative effects are more pronounced. This is the aim of our work [139, 140] presented in this chapter. We determine the location of the Mott lobes showing the even/odd asymmetry in the spinor case discussed in [123]. We then concentrate on the first lobe and discuss its magnetic properties concluding that it is always in a dimerized phase.

4.1 Mott-Superfluid phase boundary

In this section we present numerical data which determine the location of the Mott lobes in the phase diagram of the spinorial Bose-Hubbard model described by Eq. (4.1) [139, 140]. They have been obtained by using the finite-size numerical Density Matrix Renormalization Group (DMRG) with open boundary conditions [26, 27] (see App. B for details). The phase boundary has been determined by looking at the point where the Mott gap shrinks to zero [113].

Here we discuss only the anti-ferromagnetic case ($0 < U_2 < 1/2$); the parameter U_0 is set as the energy scale unit ($U_0 = 1$). Spin degrees of freedom affect the yet explained lobe structure in the $\mu - t$ plane (Fig. 1.3), because of the spin pairing when the occupation number is even. Indeed, when the anti-ferromagnetic coupling U_2 is different from zero, states with lowest spins, compatible with the constraint $n_i + S_i =$ even, are favoured. For example, the extra energy required to have two particles on a site (instead of one) at $t = 0$ is $U_0 - \mu$, while the gain associated to their singlet state (instead of triplet) is $2U_2$. The effective chemical potential is thus shifted: $\mu_{\text{eff}} = \mu + 2U_2$; therefore the upper phase boundary of the first lobe is lowered. On the other hand the lower boundary is left almost unvaried, since adding a hole gives no gain due to spin terms. Moreover the second lobe grows

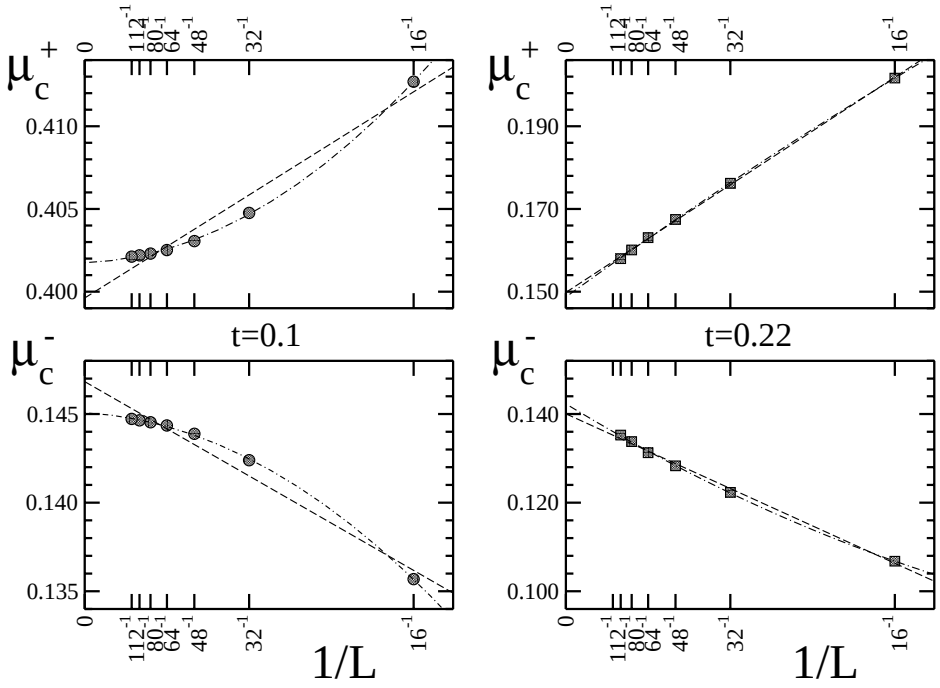

Figure 4.1: System size dependence of the critical chemical potential for the upper (μ_c^+) and the lower (μ_c^-) phase boundaries. The upper graphs correspond to the energy necessary to add a particle to the ground state of the insulator, while the lower ones to that of adding a hole. The extrapolation of the value at the thermodynamic limit has been obtained with a linear fit (dashed line) of numerical data. Quadratic fit (dashed-dotted line) is also shown to estimate minor corrections (within 1%). Here we set $U_2 = 0.2$ and two different values for the hopping t.

downwards, and similar even-odd asymmetry effects are visible for higher occupation numbers [123].

On a chain of finite length L the numerical evaluation of the Mott gap for a generic value of t has been obtained by performing three iterations of the DMRG procedure, with projections on different number sectors $L, L \pm 1$. The corresponding ground states give the desired energies E_0, $E_\pm = E_0 + \Delta E_\pm$. The extrapolation procedure to the thermodynamic limit was obtained by means of linear fit in $1/L$, as discussed in [141]. A comparison with a

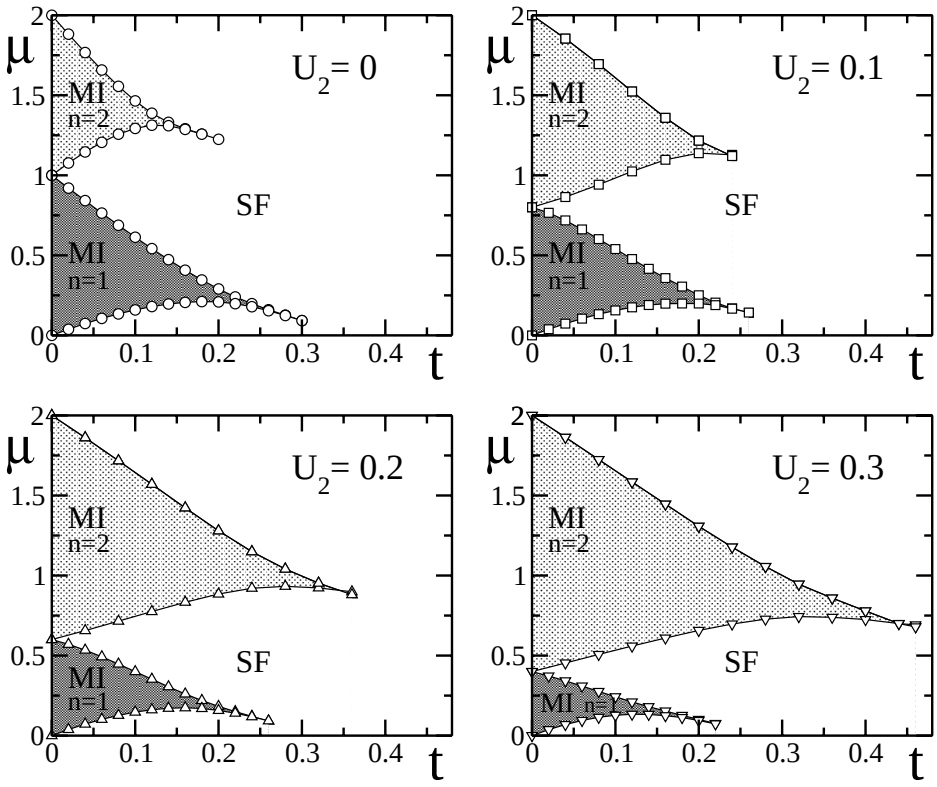

Figure 4.2: Phase diagram of the 1D spin 1 Bose Hubbard model. Dark grey indicates the location of the first Mott insulating lobe, with $n = 1$ particle per site; bright grey highlights the second lobe, where $n = 2$ particles per site are present. The different panels correspond to different values of U_2; the curves for $U_2 = 0$ coincide with the first two lobes for the spinless model computed in Refs.[142, 141].

quadratic fit (Fig. 4.1) shows that $O(1/L^2)$ corrections are negligible on the scale of Fig. 4.2. The phase boundary is then straightforwardly obtained, since the critical value of μ is given by: $\mu_c^{\pm}(t) = \pm\Delta E_{\pm}(t)$.

The DMRG method has been already employed, for the spinless case, in [142, 141]. The strategy of the DMRG is to construct a portion of the system (called the system block) and then recursively enlarge it, until the desired system size is reached. At every step the basis of the corresponding Hamiltonian is truncated, so that the size of the Hilbert space is kept man-

ageable as the physical system grows. The truncation of the Hilbert space is performed by retaining the eigenstates corresponding to the m highest eigenvalues of the block's reduced density matrix. We refer the reader to App. B for a more precise and technical description of the algorithm.
The on-site Hilbert space used for numerics has to be cut to d states by imposing a maximum occupation number $\overline{n}_{max}$. Here the presence of the spin degrees of freedom makes the analysis considerably more difficult, since the local dimension is much bigger (e.g., for $\overline{n}_{max} = 3$, d grows from 4 (spinless case) to 20 (spin 1)). Such a truncation is carefully chosen to efficiently describe the physics of the system: for the first lobe we choose $\overline{n}_{max} = 3$, for the second $\overline{n}_{max} = 4$. In each DMRG iteration we keep up to $m = 300$ states; by increasing the value of $\overline{n}_{max}$ and m, we checked that these truncations give accurate results. As target energies we used those obtained by the mapping of the Bose-Hubbard system into effective models, as described in [125]. We considered chains up to $L = 128$ sites for the first lobe, and $L = 48$ for the second lobe.

The plot of the phase diagram in the (μ, t) plane for different values of the spin coupling U_2 is shown in Fig.4.2. The first lobe tends to reduce its size on increasing the spin coupling; in particular the upper critical chemical potential at $t = 0$ is $\mu_c^+(0) = 1 - 2U_2$, while the t^* value of the hopping strength over which the system is always superfluid is suppressed as U_2 increases. On the other hand, the second lobe grows up when U_2 increases. In the limiting case $U_2 = 0.5$ the first lobe is no longer present, since the insulating ground is made up of singlet pairs on each site. In the following we concentrate on the first Mott lobe.

4.2 Magnetic properties of the first Mott lobe

Well inside the first Mott lobe, bosons can be considered localized on the sites and the system resembles a spin-1 chain. Boson tunnelling processes induce effective pairwise magnetic interactions between the spins described

by the Hamiltonian [125]:

$$\widehat{\mathcal{H}}_{\text{eff}} = \kappa \sum_{\langle ij \rangle} \left[\cos\theta \, (\widehat{\mathbf{S}}_i \cdot \widehat{\mathbf{S}}_j) + \sin\theta \, (\widehat{\mathbf{S}}_i \cdot \widehat{\mathbf{S}}_j)^2 \right] \tag{4.2}$$

with

$$\tan\theta = \frac{1}{1-2U_2}\,, \qquad \kappa = \frac{2t^2}{1+U_2}\sqrt{1+\tan^2\theta} \ . \tag{4.3}$$

The absence of higher order terms, such as $(\widehat{\mathbf{S}}_i \cdot \widehat{\mathbf{S}}_j)^3$, is due to the fact that the product of any three spin operators can be expressed via lower order terms. An additive term independent from the spin configuration has been neglected for the sake of simplicity. The coupling constants are calculated by means of perturbative analysis: first order terms are absent since hopping does not conserve local number of particles.

The $S = 1$ Heisenberg model with biquadratic interactions (Eq. 4.2) has been widely studied, since it exhibits a rather rich phase diagram [133, 143]. Let us consider the two site problem to understand where this richness comes from. The energy depends only on the pair total spin, as shown in the table:

S_{tot}	$\vec{S}_1\vec{S}_2$	$(\vec{S}_1\vec{S}_2)^2$	Energy/κ
0	-2	4	$-2\cos\theta + 4\sin\theta$
1	-1	1	$-\cos\theta + \sin\theta$
2	1	1	$\cos\theta + \sin\theta$

In the case of anti-ferromagnetic interaction in Eq.(4.1), the parameter θ varies in the interval $\theta \in [-3/4\pi, -\pi/2[$. Thus each bond tends to form a singlet-spin configuration ($S_{tot} = 0$), but singlet states on neighbouring bonds are not allowed. A spin order will appear, whose precise nature depend on the lattice and dimensionality. In the 1D chain under our investigations, there are two possible ground states that may appear in this situation. A *nematic* state can be constructed by mixing states with total spin $S = 0$ and $S = 2$ on each bond. This construction can be repeated on neighbouring bonds, thereby preserving translational invariance. This state breaks the spin-space rotational group $O(3)$, though time-reversal symmetry is preserved. On the other hand a possibility to have $SO(3)$ symmetric solution

stems from breaking translational invariance. Indeed, a *dimerized* solution with singlets on every second bond satisfy these requirements.

At mean field level a nematic solution can be written as

$$|N\rangle = \bigotimes_i |S_i = 1,\ m_i = 0\rangle; \tag{4.4}$$

its energy is $E_{\rm nem}^{\rm (mf)} = 2\sin\theta\ (L-1)$.
More generally, a nematic state is defined by the vanishing of any spin operator expectation value ($\langle \widehat{S}_i^\alpha \rangle = 0,\ \alpha = x, y, z$), while some of the quadrupole operators have finite ones. The tensor $\mathcal{Q}^{ab} = \langle \widehat{S}^a \widehat{S}^b \rangle - \frac{2}{3}\delta^{ab}$ is a traceless diagonal matrix, due to invariance under spin reflections. Since it has two identical eigenvalues ($\langle (\widehat{S}_i^x)^2 \rangle = \langle (\widehat{S}_i^y)^2 \rangle \neq \langle (\widehat{S}_i^z)^2 \rangle$), it can be written as $\mathcal{Q}^{ab} = Q\left(d^a d^b - \frac{1}{3}\delta^{ab}\right)$ using an order parameter

$$\langle \widehat{Q} \rangle \equiv \langle (\widehat{S}_i^z)^2 \rangle - \langle (\widehat{S}_i^x)^2 \rangle = \frac{3}{2}\langle (\widehat{S}_i^z)^2 \rangle - 1 \tag{4.5}$$

and a unit vector $\mathbf{d} = \pm\mathbf{z}$. However, since $[\widehat{Q}, \widehat{\mathcal{H}}_{\rm eff}] = 0$, Coleman's theorem forbids to get $Q \neq 0$ in one-dimensional finite size systems, analogously to what happens for the magnetization without external field. Therefore we characterized the range of nematic correlations in the ground state by coupling this operator to a fictitious "nematic field"

$$\widehat{\mathcal{H}}_\lambda = \widehat{\mathcal{H}}_{\rm eff} + \lambda \widehat{Q} \tag{4.6}$$

and then by evaluating the nematic susceptibility $\chi_{\rm nem}$ as a function of the system size:

$$\chi_{\rm nem} \equiv -\left.\frac{{\rm d}^2 E_0(\lambda)}{{\rm d}\lambda^2}\right|_{\lambda=0} = \sum_\gamma \frac{|Q_{0,\gamma}|^2}{E_\gamma - E_0}\,, \tag{4.7}$$

where $E_0(\lambda)$ is the ground energy of $\widehat{\mathcal{H}}_\lambda$, $Q_{0,\gamma}$ is the matrix element between the ground and an excited state of $\widehat{\mathcal{H}}_{\rm eff}$ (respectively with energy E_0 and E_γ).

The simplest dimerized state one can imagine is written as

$$|D\rangle = \bigotimes_{i\ \text{odd}} |S_i = 1,\ S_{i+1} = 1,\ S_i + S_{i+1} = 0\rangle\ , \tag{4.8}$$

and has energy $E_{\rm dim}^{\rm (mf)} = \frac{L}{2}\left(-2\cos\theta + 4\sin\theta\right) + \left(\frac{L}{2} - 1\right)\frac{4}{3}\sin\theta$.
Dimerization could be described by looking at the differences in expectation values of the pair Hamiltonian $\widehat{\mathcal{H}}_{\rm eff}^{(ij)}$ on adjacent links ($\widehat{\mathcal{H}}_{\rm eff} = \sum_{\langle ij\rangle} \widehat{\mathcal{H}}_{\rm eff}^{(ij)}$) [1]. The order parameter D reads[133]

$$D \equiv \left| \langle \widehat{\mathcal{H}}_{\rm eff}^{(i-1,i)} - \widehat{\mathcal{H}}_{\rm eff}^{(i,i+1)} \rangle \right| . \tag{4.9}$$

From the mean field ansatz in Eqs. (4.4) and (4.8) it seems that a narrow nematic region exists between the ferromagnetic phase boundary ($\theta_F = -3\pi/4$, i.e. $U_2 = 0$) and a critical angle $\theta_C \approx \arctan 3/2 \simeq -0.69\pi$ (i.e. $U_2 \sim 10^{-2}$), whereas a dimerized solution is favoured in the remaining antiferromagnetic region $\theta_C \leq \theta \leq -\pi/2$. The nematic-to-dimer quantum phase transition has also been conjectured in a more rigorous way in Ref. [131], and has originated a long debated question in literature [131, 132, 133, 134, 135, 136, 137, 138, 143].

The dimerization order parameter D should scale to zero in the whole nematic region. This possibility has been analyzed in Ref. [133] where it was suggested that D might go to zero in an exponential way near the ferromagnetic boundary, making it difficult to detect the effective existence of the nematic phase. This interesting challenge has motivated numerical investigations with different methods [133, 134, 136, 137, 143]. Here we present new DMRG results published in Ref. [139, 140] which, in our opinion, clarify the magnetic properties of the first Mott lobe (for sufficiently small hopping) and consequently of the Heisenberg chain with biquadratic interaction.

According to our numerical calculations there is *no* intermediate nematic phase, indeed we found a finite value of the dimerization order parameter for all values of θ, down to $\theta_F = -3\pi/4$. The simulations of the bilinear-biquadratic model Eq. (4.2) are less time and memory consuming than Bose-Hubbard ones, since the local Hilbert space has a finite dimension $d = 3$. The number of block states kept during the renormalization procedure was chosen

[1] On any finite chain some inhomogeneity exists, thus leading to a finite D_L even if $D = 0$. Quantitatively, an order parameter D_L could be defined by evaluating Eq. (4.9) in the middle of the finite size chain. The order parameter D has to be extrapolated in the thermodynamic limit: $D \equiv \lim_{L\to\infty} D_L$.

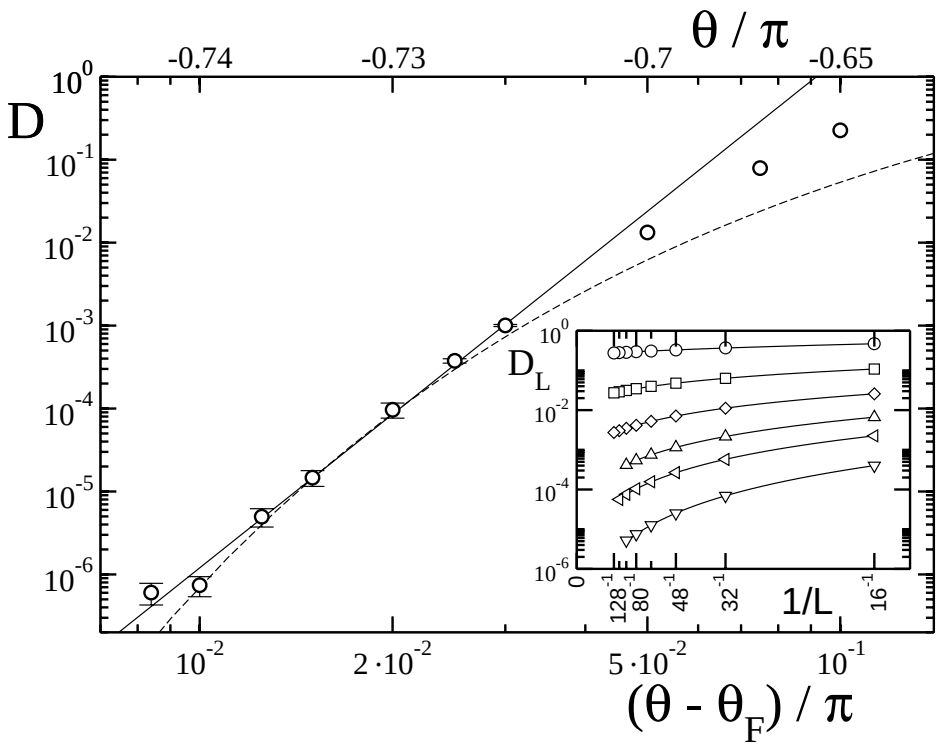

Figure 4.3: Behaviour of the dimerization order parameter D of Eq. (4.9) near the ferromagnetic boundary: solid line shows a power law fit $D \sim (\theta - \theta_F)^\gamma$ of numerical data with an exponent $\gamma \simeq 6.15$; dashed line shows an exponential law fit $D \sim \exp[-a/(\theta - \theta_F)^{-1/2}]$ with $a \simeq 2.91$. The linear fit is done over data for $\theta < -0.7\pi$, while the exponential fit is for $\theta \leq -0.73\pi$. The inset shows finite size scaling of D_L for selected values of θ: circles ($\theta = -0.65\pi$), squares (-0.7π), diamonds (-0.72π), triangles up (-0.73π), triangles down (-0.735π), triangles left (-0.74π). In order to extrapolate the order parameter D, numerical data have been fitted with $D_L = D + cL^{-\alpha}$ (straight lines). DMRG simulations are performed with $m \simeq 140$ for $\theta > -0.73\pi$, and $m \simeq 300$ for $\theta \leq -0.73\pi$.

step by step in order to avoid artificial symmetry breaking. This procedure insures that there are no spurious sources of asymmetry like partially taking into account a probability multiplet (see App. B). Here we considered up to $m \simeq 300$ states in order to obtain stable results. Raw numerical data are shown in the inset of Fig. 4.3, where the finite size dimerization parameter

$D(L)$ is plotted as a function of the chain length L (see Eq. 4.9). Finite size scaling was used to extrapolate to the thermodynamic limit. After the extrapolation to the $L \to \infty$ limit, we fitted the dimer order parameter with a power law

$$D = \left(\frac{\theta - \theta_F}{\theta_0} \right)^{\gamma} \tag{4.10}$$

where $\gamma \sim 6.1502$ and $\theta_0 \sim 0.09177\,\pi$ (Fig. 4.3, solid line). We also tried to fit our data by an exponential law of the form

$$D = D_0\, e^{-a/\sqrt{\theta - \theta_F}} \tag{4.11}$$

as suggested in [133], with $a \sim 2.911$, $D_0 \sim 9.617$; this fit seems to work for narrower regions (Fig. 4.3, dashed line), however from our numerics we cannot exclude an exponential behaviour of D in the critical region. The dimerized phase thus seems to survive up to the ferromagnetic phase boundary, independently from the chosen fitting form.

Another argument in support of the absence of the nematic phase comes by the fact that the scaled gap between the ground state E_0 and the lowest excited state E_2 (which is found to have total spin $S_T = 2$) seems not to vanish in the interesting region $\theta > -0.75\pi$ (see Fig. 4.4). Moreover its behaviour in proximity of θ_F is consistent with our perturbative analysis (see 4.2.1, Eq. (4.17)): the linear term is well estimated by $\sqrt{2}\frac{S(S+1)}{L}(\theta - \theta_F)$. A closure of this gap would have been a signature of a nematic ordered phase, since it has not well defined total spin on the contrary of a dimerized chain.

To further characterize the behaviour of the system we analyzed the susceptibility χ_{nem} of the chain to nematic ordering. Numerical data, presented in Fig. 4.5, show a power law behaviour $\chi_{nem}(L) \propto L^{\alpha}$ as a function of the system size. The exponent α (shown in the inset) approaches the value $\alpha = 3$ as $\theta \to \theta_F$. This can also be confirmed by means of a perturbative calculation around the exact solution available at θ_F (see 4.2.1). The only non vanishing $Q_{0,\gamma}$ is the one where $\gamma = |S = 2\rangle$, and scales $\sim L^2$; as already stated, the energy difference $(E_\gamma - E_0)$ scales $\sim L^{-1}$. Then the conclusion follows from Eq. (4.7). The increase of the exponent for $\theta \to \theta_F$ indicates, as suggested in [136], that a tendency towards the nematic ordering is enhanced as the

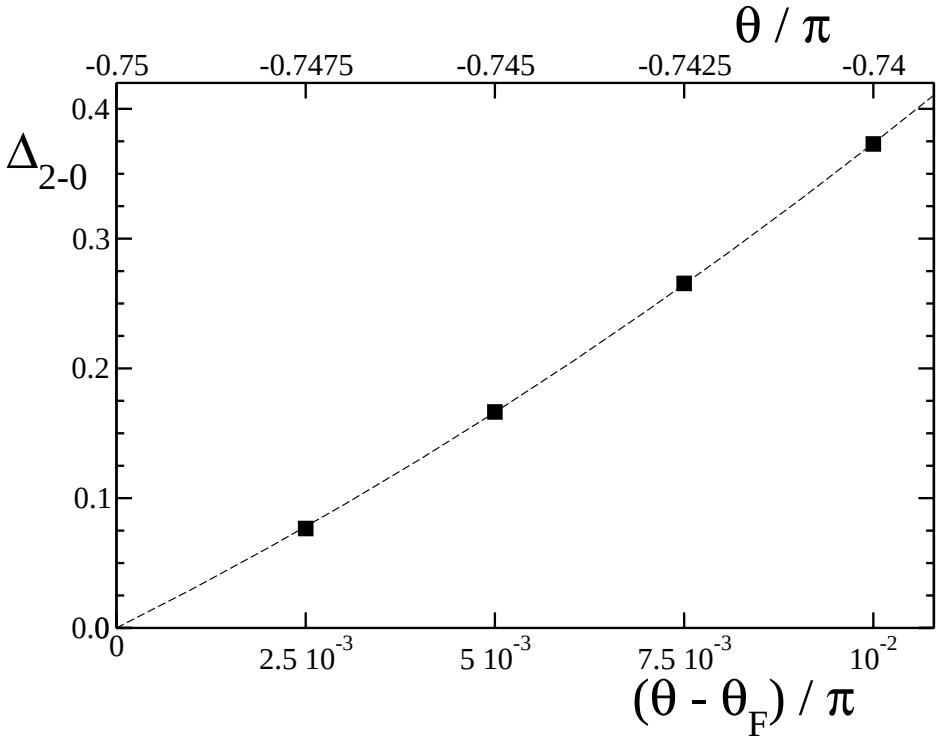

Figure 4.4: Extrapolated scaled gap $\Delta_{2-0} = (L-1)(E_2 - E_0)$ at the thermodynamic limit, for some points at $\theta \leq -0.74\pi$. Dashed line indicates a quadratic fit of data $\Delta_{2-0} \sim c_1(\theta - \theta_F) + c_2(\theta - \theta_F)^2$, where the linear coefficient $c_1 \simeq 9.3$ is consistent with the perturbative calculation done in 4.2.1, which gives $\tilde{c}_1 = 6\sqrt{2} \approx 8.5$.

dimer order parameter goes to zero. On the other hand, we consider the fact that the value 3 is reached only at the ferromagnetic boundary θ_F, as another proof in support of our thesis against the existence of an intermediate proper nematic phase.

In this Chapter we analyzed, by means of a DMRG analysis, the phase diagram of the one-dimensional spinor boson condensate on an optical lattice. We determined quantitatively the shape of the first two Mott lobes, and the even/odd properties of the lobes induced by the spin interaction. We furthermore discussed the magnetic properties of the first lobe. Our results indicate that the Mott insulator is *always* in a dimerized phase.

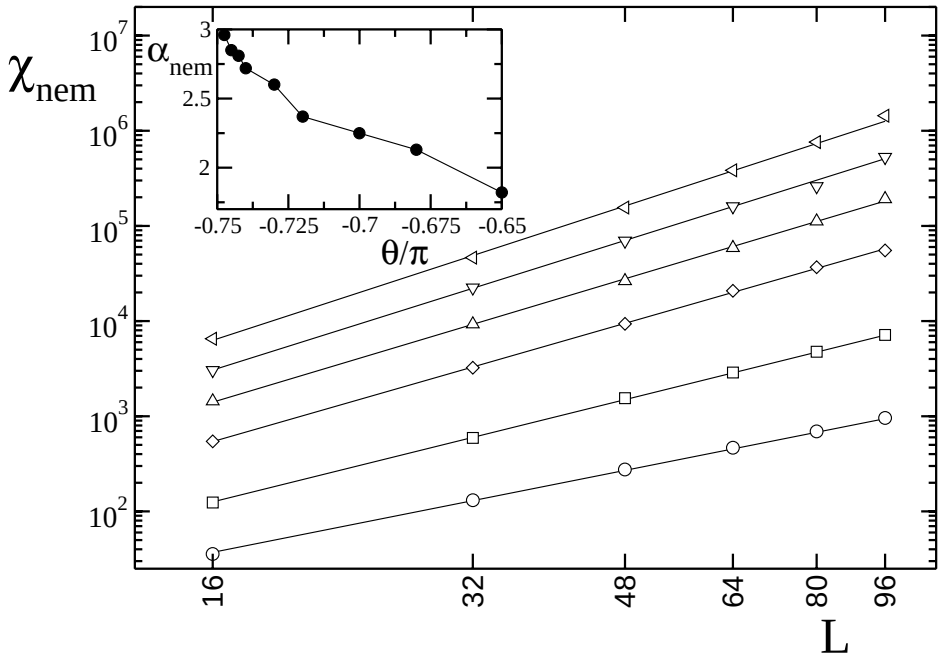

Figure 4.5: Nematic susceptibility χ_{nem} as a function of the system size L. The various symbols refer to different values of θ: circles ($\theta = -0.65\pi$), squares (-0.7π), diamonds (-0.73π), triangles up (-0.74π), triangles down (-0.745π), triangles left (-0.7475π). Straight lines are the result of a power law fit $\chi_{nem} = cL^{\alpha}$ of numerical data. In the inset the exponent α is plotted as a function of θ.

4.2.1 Perturbative analysis of susceptibility

Since both $\widehat{\mathcal{H}}$ and $\widehat{Q}$ conserve the total spin, their expectation values do not depend on the projection along z, and we can henceforth restrict our analysis to $S_z = 0$. At $\theta = \theta_F \equiv -3/4\,\pi$ the Hamiltonian on each link becomes a multiple of the sum of scalar product and its square. For a pair of nearest neighbour sites the generic state (with S_z fixed to 0) can be written in terms of a superposition of states with defined pair total spin, $|\psi_{i,i+1}\rangle = \sum_{S=0}^{2} c_S |S,0\rangle$. The interesting matrix elements are thus:

$$\langle \widehat{\mathbf{S}}_i \cdot \widehat{\mathbf{S}}_{i+1} \rangle_\psi = -2\,|c_0|^2 - |c_1|^2 + |c_2|^2 \tag{4.12}$$

$$\langle \left(\widehat{\mathbf{S}}_i \cdot \widehat{\mathbf{S}}_{i+1} \right)^2 \rangle_\psi = 4\,|c_0|^2 + |c_1|^2 + |c_2|^2 \tag{4.13}$$

The energy minimization is given by $c_1 = 0$: every $|\psi_{i,i+1}\rangle$ completely symmetric under particles' permutation has energy $E_{i,i+1} = -\sqrt{2}$. The ground of the entire chain should thus be completely symmetric: states could be labelled by the (even) total spin S (and S_z).

A further decomposition of $|S,0\rangle_L$ into the tensor products of single site states is useful; the only relevant thing is the number n_0 of sites with $s_z = 0$ ($n_0 + n_+ + n_- = L$ and $n_+ = n_-$): $|S,0\rangle_L = \sum_{n_0} c^{(L)}_{S,n_0} \mathcal{P}\{|n_0\rangle_L\}$. Indeed, the nematic operator $\widehat{Q}$ is such that

$$\widehat{Q}\,\mathcal{P}\{|n_0\rangle_L\} = \frac{L-3n_0}{2}\mathcal{P}\{|n_0\rangle_L\}\ . \tag{4.14}$$

Using explicit expressions for $c^{(L)}_{S,n_0}$ and the selection rules $\Delta S = 0, \pm 2$, one obtains the matrix elements $\langle S|\widehat{Q}|S'\rangle$:

$$\begin{aligned}\langle S,0|\widehat{Q}|S',0\rangle = \Big(& \delta_{S,S'}\, q_0(S)\,(L+3/2)^2 \\ & +\delta_{S,S'-2}\, q_2(S)\,(L-S)\ (L+S'+1) \\ & +\delta_{S,S'+2}\, q_2(S+2)\,(L-S')\ (L+S+1)\ \Big)\end{aligned} \tag{4.15}$$

On the other hand, the system Hamiltonian for $\theta = \theta_F + \delta$ can be written as

$$\widehat{\mathcal{H}}_\delta = \cos\delta\,\widehat{\mathcal{H}}_0 + \sin\delta\,\widehat{\mathcal{H}}_p \tag{4.16}$$

where

$$\widehat{\mathcal{H}}_0 = -\frac{1}{\sqrt{2}}\sum_{\langle ij\rangle}\left[(\widehat{\mathbf{S}}_i\cdot\widehat{\mathbf{S}}_j) + (\widehat{\mathbf{S}}_i\cdot\widehat{\mathbf{S}}_j)^2\right];\quad \widehat{\mathcal{H}}_p = \frac{1}{\sqrt{2}}\sum_{\langle ij\rangle}\left[(\widehat{\mathbf{S}}_i\cdot\widehat{\mathbf{S}}_j) - (\widehat{\mathbf{S}}_i\cdot\widehat{\mathbf{S}}_j)^2\right]$$

Energy differences that enter the susceptibility expression $E_\delta(L,S) = \langle S|\widehat{\mathcal{H}}_\delta|S\rangle$ can be estimated with perturbative analysis for $\delta \longrightarrow 0$:

$$E_\delta(L,S) = -\sqrt{2}\,\left[(L-1) + \left((L+1) - \frac{S(S+1)}{L}\right)\,\delta + O(\delta^2)\right]\ . \tag{4.17}$$

The ground state will thus have $S = 0$ and the only non-zero matrix element of $\widehat{Q}$ in the susceptibility expression is $\langle 0|\widehat{Q}|2\rangle$. Consequently the scaling law of χ_{nem} is obtained:

$$\chi_{nem} \propto \delta^{-1}\,L^2\,(L+3) \tag{4.18}$$

and the asymptotic exponent 3 is recovered, as well as the discontinuity in θ_F (where the system is non-linear under the action of the λ field). We stress that this result accounts also for the linear part of the gap behaviour with $(\theta - \theta_F)$ in Fig. 4.4.

As δ increases, higher orders in perturbation theory become relevant and the scaling law is modified firstly by non-$1/L$ terms in the energy differences at susceptibility's denominator, and secondly by different $Q_{\alpha,\gamma}$ contributions.

Chapter 5

Attractive Fermions

The ground-state properties of multi-component asymmetric fermionic systems have attracted continued interest for many decades in several fields of physics. These are systems with unequal mass and/or density (or unequal chemical potential) for the different constituent elements, which are of great interest in high-energy [83, 84], condensed matter [84, 85], and atomic physics [86, 87, 88, 89, 90]. Attractive intercomponent interactions can destroy the canonical scenario predicted by Landau's theory of normal Fermi liquids, leading to various types of exotic superconducting instabilities, which might be even responsible for some glitches (*i.e.* rapid variations in the rotation frequency) in pulsars [83].

In current experimental setups in atomic physics, the cold gas can be subjected to a strongly anisotropic harmonic potential, characterized by angular frequencies $\omega_\perp$ and $\omega_\parallel$ in the radial and axial directions (with $\omega_\parallel \ll \omega_\perp$). The fermions are dynamically $1D$ if the anisotropy parameter of the trap is much smaller than the inverse of the particle number ($\omega_\parallel/\omega_\perp \ll N^{-1}$). The preparation of two-component Fermi gases in a quasi-$1D$ geometry [29] provides a unique possibility to experimentally study phenomena predicted a long time ago for electrons in $1D$. Independently of statistics, the effective low-energy description of all $1D$ systems is based on a harmonic theory of long-wavelength fluctuations due to the interplay between topology and interactions [144]. In particular, linearization of the single-particle dispersion relation in the Tomonaga-Luttinger model for fermions allows bosoniza-

tion and leads to gapless elementary excitations consisting of density and spin-density waves that propagate with acoustic dispersion laws at different velocities [30].

Great theoretical and computational efforts has been spent in relation to strongly correlated electron fluids in condensed matter physics. It is worth mentioning at this point that experimental evidence supporting the Tomonaga-Luttinger model has come from measurements on edge properties of $2D$ electron liquids in semiconductors [145]. Both tunnelling of electrons from a metal into the edge and tunnelling of fractionally charged quasiparticles between the edges of a quantum Hall liquid are explained in terms of a chiral Luttinger liquid flowing through the edge states. Nonetheless, some exotic phases are still object of theoretical and experimental investigations in the community. Restricting ourselves to the attractive interactions, *i.e.* $U < 0$, these are namely the Luther-Emery phase and the Fulde-Ferrel-Larkin-Ovchinnikov one. LE [79] phase is an unpolarized phase which exhibit a gap in the spin sector: this induces an exponential decay of spin correlations, while singlet superconducting and charge-density wave correlations have a power-law decay [30]. The FFLO phase [80, 81], is an even more exotic phase, that has recently attracted a great deal of interest in both the experimental and the theoretical community [83, 84, 85, 86, 87, 88, 89, 90]. Cooper pairing occurs at a finite momentum equal to the distance between the two distinct Fermi surfaces, yielding a spatially-dependent superconducting order parameter.

In this Chapter we present our results about experimental feasibility of these two long-searched states by means of ultracold fermions living in optical lattices in harmonic confinements. We address the reader to the introductory Section 1.3 in order to have more general informations about these phases, apart from specific original results.

Whereas so far no observation of the Luther-Emery phase has been reported in solid-state electronic systems, in Sec. 5.1 we propose realistic unpolarized 1D Optical Lattices as a tool to realize and highlight the presence of such a phase [82].

The region of parameter space available for the FFLO phase in $3D$ space is

quite modest [84], whilst quasi-one dimensional systems are very well known to be good candidates for the realization of the FFLO phase [84, 91, 92, 93]. In Sec. 5.2 we show that a spin-polarized attractive Fermi gas loaded in a $1D$ OL is always in a polarized superfluid state of the FFLO type. We also discuss in detail what is the expected behavior of several observables, ranging from momentum distributions to density-density correlation functions, that are measured routinely in cold-atom laboratories.

5.1 Spin balance and Luther-Emery liquids

In the presence of attractive interactions spin-balanced fermions are predicted to form a peculiar $1D$ liquid phase characterized by a massive spin sector, *i.e.* a Luther-Emery liquid [79]. So far no observation of the Luther-Emery phase has been reported in solid-state electronic systems. In Ref. [146, 147, 148] it has been shown that an integrable model of two-component interacting Fermi gases in a quasi-$1D$ geometry exhibits a smooth crossover between a Luther-Emery liquid and a Luttinger liquid of tightly-bound bosonic dimers. A Luther-Emery point has also been identified in a $1D$ model of fermions with a narrow Feshbach resonance that allows them to bind reversibly into bosonic molecules [149]. Seidel and Lee [150, 151] have shown that the ground-state energy of a system with spin gap and gapless charge degrees of freedom has an exact period of $hc/(2e)$ (corresponding to half a flux quantum) as a function of an applied Aharonov-Bohm flux. In a recent paper [82] we proposed to exploit the new possibilities offered by Optical Lattices (OLs) in order to study the Luther-Emery phase and the existence of antiparallel-spin pairing in a Luther-Emery liquid. A careful analysis is devoted to analyze the interplay between attractive interactions and the confining potential. This is not a merely quantitative issue: it is well known that in other cases the confinement modifies qualitatively the properties of the gas. An example is the coexistence of superfluid (metallic) and Mott-insulating regions in bosonic (fermionic) OLs [152, 153, 154, 155, 72, 73]. This task is thus of fundamental importance in order to assess the very existence and the nature of the Luther-Emery phase in realistic cold-atom systems. We first

Table 5.1: Ground-state and pair-binding energies for $N = 30$, $L = 100$, and $V_2/t = 4 \times 10^{-3}$. The agreement between DMRG and BALDA for $E_{\rm GS}$ is quite satisfactory even for $U/t = -20$, where the deviation is about 2.2%. However, BALDA tends to overestimate $E_{\rm P}$ even at moderate values of U/t. The "$\times$" sign indicates that the spin-BALDA code for 31 atoms does not converge for $U/t = -20$.

U/t	$E_{\rm GS}^{\rm BALDA}/(tL)$	$E_{\rm GS}^{\rm DMRG}/(tL)$	$E_{\rm P}^{\rm BALDA}/t$	$E_{\rm P}^{\rm DMRG}/t$
-0.5	-0.35824	-0.35832	-0.0283	-0.0213
-1	-0.39336	-0.39340	-0.0614	-0.0577
-2	-0.47672	-0.47631	-0.3265	-0.2442
-4	-0.70693	-0.69010	-5.1008	-1.3278
-20	-3.05320	-2.98536	$\times$	-16.4217

show that, in the presence of harmonic confinement, a $1D$ Fermi gas with attractive interactions inside an OL manifests unambiguous real-space spin pairing, which in turn determines the emergence of Atomic-Density Waves (ADWs) in the ground-state density profile. We then propose an experiment that can lead to the observation of these ADWs.

The tendency of fermions to pairing can be studied analyzing the pair binding energy [156] defined as

$$E_{\rm P} = E_{\rm GS}(N+2) + E_{\rm GS}(N) - 2\,E_{\rm GS}(N+1) \tag{5.1}$$

where $E_{\rm GS} = \langle \Psi_{\rm GS}|\hat{\mathcal{H}}|\Psi_{\rm GS}\rangle$ is the ground-state energy, with $N = \langle \sum_i \hat{n}_i \rangle$ the total number of particles. In Table 5.1 we report results for $N = 30$ fermions in a lattice with $L = 100$ sites, inside a trap with $V_2/t = 4 \times 10^{-3}$. $E_{\rm P}$ is negative, thus hinting at the presence of an opposite-spin pairing, i.e. at the presence of spin singlets as fundamental objects around in the system.

Such a singlet pairing tendency should lead to the presence of Atomic Density Waves (ADWs), and indeed we found out that their presence is stabilized by the harmonic potential. In Fig. 5.1 we report our numerical results for the site occupation of a gas with $N = 30$ atoms. The consequences of Luther-Emery pairing in the presence of confinement are dramatic.

For $U < 0$ the site occupation exhibits a density wave (with $N/2$ peaks in a weak trap), reflecting the tendency of atoms with different pseudospins to form stable spin-singlet dimers that are delocalized over the lattice. For small V_2/t (see the top panel of Fig. 5.1) n_i in the bulk of the trap ($80 \leq i \leq 100$) can be fitted to an ADW of the form $n_i = \widetilde{n} + A_{\rm ADW} \cos{(k_{\rm ADW}\, i + \varphi)}$. For example, for $V_2/t = 10^{-5}$ we find $k_{\rm ADW} = 0.73$ for $U/t = -1$ and $k_{\rm ADW} = 0.84$ for $U/t = -3$. In such a weak confinement the oscillations of the site occupation extend to regions far away from the center of the trap, where they are characterized by smaller edge wavenumbers. For $V_2 = 0$ bosonization predicts [30] an incipient ADW with wavenumber $2k_{\rm F}$, $k_{\rm F}$ being the Fermi wavenumber, quenched by strong quantum fluctuations. In the present case we find $k_{\rm ADW} \simeq 2k_{\rm F}^{\rm eff}$, where the effective Fermi wavenumber $k_{\rm F}^{\rm eff} = \pi\widetilde{n}/2$ is determined by the average density in the bulk of the trap (note that $k_{\rm ADW} = \pi$ when the average density in the bulk reaches half filling).

Finite-size effects become important on increasing V_2 (see the bottom panel of Fig. 5.1) and a simple fitting formula such as the one used above does not work even at the center of the trap. Eventually when $V_2/t \approx 10^{-1}$ a region of doubly-occupied sites develops at the center of the trap: spin-singlet dimers, which in a weak trap are delocalized, are squeezed close together to produce an extended region of $\approx N/2$ doubly-occupied consecutive sites.

In Fig. 5.2 we show how the ADWs evolve with increasing $|U|/t$ at fixed V_2/t. For weak-to-intermediate coupling ADWs are present in the bulk of the trap. The agreement between the BALDA and the DMRG results is excellent for $|U|/t \leq 1$. With increasing $|U|/t$ the BALDA scheme deteriorates [1], leading to an overestimation of the amplitude of the ADWs (see panel C). According to DMRG, the bulk ADWs disappear in the extreme strong-coupling limit (see panel D). For $|U|/t \gg 1$ a flat region of doubly-occupied sites emerges at the trap center, resembling that described above

[1] This is different from the case $U > 0$, where the BALDA profiles agree with quantum Monte Carlo and DMRG data even for $U/t > 1$ [73, 77]. Since the $U < 0$ Bethe *Ansatz* is obtained from that at $U > 0$ by means of an exact transformation, this shows that the locality assumption inherent in the LDA is less well satisfied for attractive than for repulsive interactions. In fact, it appears that the BALDA performance for a fixed value of $|U|/t$ depends on the value of V_2/t

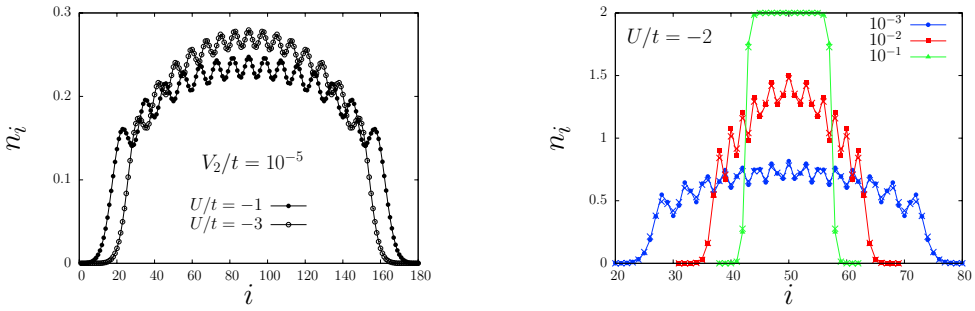

Figure 5.1: Top panel: DMRG results for the site occupation n_i as a function of site position i for a system with $N = 30$ fermions in $L = 180$ lattice sites, and in the presence of a harmonic potential with $V_2/t = 10^{-5}$. For this value of V_2/t BALDA overestimates the ADW amplitude. Bottom panel: DMRG results (crosses) for $N = 30$, $L = 100$, and $U/t = -2$ are compared with BALDA data (filled symbols). V_2/t is increased from 10^{-3} to 10^{-1}. The thin solid lines are just a guide for the eye.

for the case of weak interactions and strong confinement (see the bottom panel of Fig. 5.1).

The disappearance of the ADWs at strong coupling can be explained by mapping the Hamiltonian (1.28) onto a spin-1/2 XXZ model [30, 79],

$$\hat{\mathcal{H}}_\infty = \sum_i \sum_{\alpha=x,y,z} J_\alpha \hat{\sigma}_i^\alpha \hat{\sigma}_{i+1}^\alpha + \sum_i B_i \hat{\sigma}_i^z \,, \tag{5.2}$$

with $J_x = J_y = -J_z = -t^2/|U|$ and $B_i = V_2(i - L/2)^2$. The total site occupation operator $\hat{n}_i$ is related to $\hat{\sigma}_i^z$ by $\hat{n}_i = 1 + \hat{\sigma}_i^z$. Particle-number conservation requires working in a sector with fixed total magnetization $\langle \sum_i \hat{\sigma}_i^z \rangle = N - L \equiv M$. In the limit $|U|/t \to \infty$, J_α is negligibly small and thus finding the ground state of $\hat{\mathcal{H}}_\infty$ is equivalent to solving the problem of orienting a collection of spins in a nonuniform magnetic field in order to minimize the Zeeman energy in producing a magnetization M. Thus, for $|U|/t \to \infty$ one expects a classical state with $\langle \hat{\sigma}_i^z \rangle = 1$ ($\langle \hat{n}_i \rangle = 2$) in $N/2$ sites at the trap center where B_i is small, and $\langle \hat{\sigma}_i^z \rangle = -1$ ($\langle \hat{n}_i \rangle = 0$) in the remaining $L - N/2$ sites.

The main results of these investigations [82], *i.e.* negative pair bind-

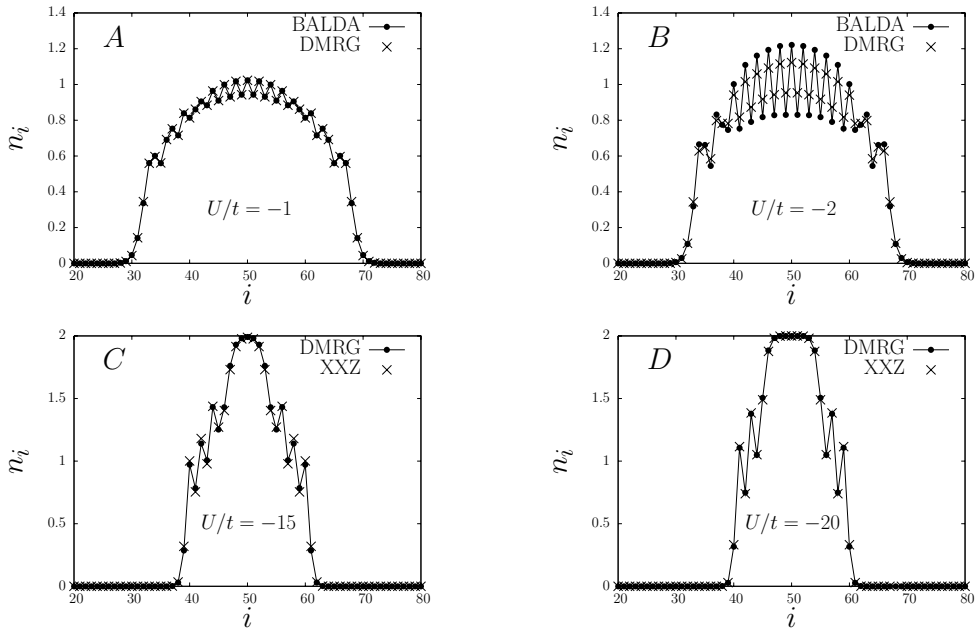

Figure 5.2: Site occupation n_i as a function of i for $N = 30$, $L = 100$, and $V_2/t = 4 \times 10^{-3}$. Panels A and B: DMRG results (crosses) are compared with BALDA data (filled circles). Panels C and D: DMRG results for the Hamiltonian (1.28) (filled circles) are compared with DMRG results for the strong-coupling Hamiltonian (5.2) (crosses). The thin solid lines are just a guide for the eye.

ing energies and delocalized dimers forming ADWs in weak traps, are not a result of finite-size effects. Indeed, the proper finite size scaling to get the thermodynamic limit in the presence of an external parabolic potential has been used to test both $E_{\rm P}$ and $A_{\rm ADW}$. The procedure proposed in Ref. [157] consists in performing the limits $N \to \infty$ and $V_2/t \to 0$ keeping $N\sqrt{V_2/t} = \text{const}$. We found that in this limit (i) $E_{\rm P}$ approaches a finite negative value and (ii) the amplitude of the ADWs (calculated after subtracting the smooth Thomas-Fermi site-occupation profile) approaches a finite value. For example, for $U/t = -2$ and $N^2 V_2/t = 3.6$ we find $E_{\rm P}(N \gg 1)/t = -0.184 - 0.171 \exp(-N/28.61)$ and $A_{\rm ADW}(N \gg 1) = 0.032 + 0.114 \exp(-N/39.93)$.

The interplay between attractive interactions and harmonic confinement

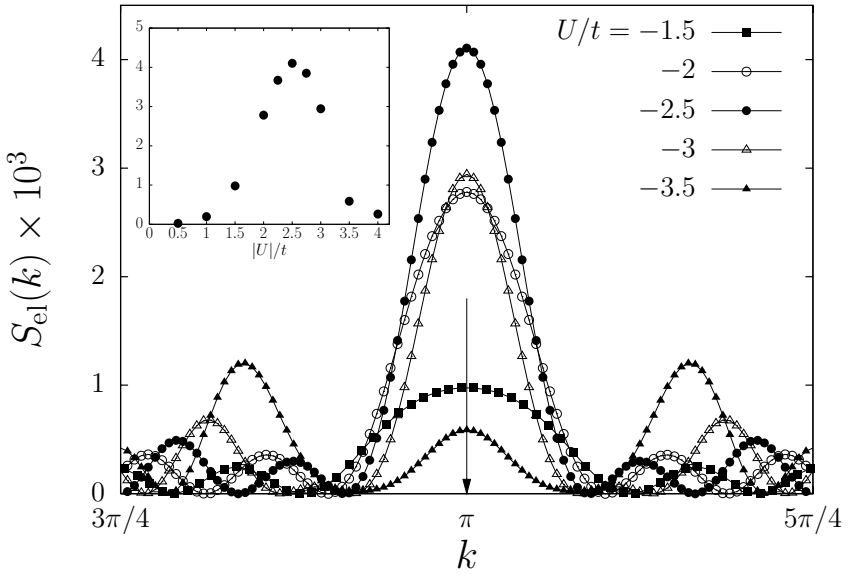

Figure 5.3: DMRG data for $S_{\rm el}(k)$ as a function of k in the range $3\pi/4 \leq k \leq 5\pi/4$, for $N = 30$, $L = 100$, and $V_2/t = 4 \times 10^{-3}$. The long vertical arrow indicates the value of $k_{\rm ADW}$. In the inset we show $S_{\rm el}(\pi)$ as a function of $|U|/t$.

on ultracold fermions inside an optical lattice thus leads to coexistence of spin pairing and atomic-density waves of dimer singlets. This has been interpreted as a Luther-Emery phase signature: another, even more convincing proof, will be given in the next Section where the power law decay of Cooper correlators is shown (see Fig.5.4).

Finally, we want to stress the experimental feasibility of observing these Luther-Emery signatures. It is again a crucial feature of cold atoms in optical lattices, since usual condensed matter systems has not yet offered a convincing proof of the LE phase. On one hand, the existence of a finite pairing gap $\Delta = -E_{\rm P}/2$ can be tested *via* radio-frequency spectroscopy [158, 159]. On the other side, ADWs can be detected by a measurement of the elastic contribution to the light-scattering diffraction pattern, *i.e.* the Fraunhofer structure factor

$$S_{\rm el}(k) = \frac{1}{N^2} |\sum_j e^{-ikj} n_j|^2 \,, \tag{5.3}$$

through the appearance of a peak at $k = k_{\rm ADW}$. In Fig. 5.3 we show the most favourable situation where there is a wide region in the trap with oscillations at $k_{\rm ADW} = \pi$, inducing a well defined peak in $S_{\rm el}(k)$. The height of the peak is non-monotonic as a function of $|U|/t$, as a consequence of the aforementioned crossover between the $U \to 0^-$ and $U \to -\infty$ limits, and is best observed when this ratio is of order two. However, in a case such as that shown in the top panel of Fig. 5.1, where the density oscillations extend into regions far away from the trap center, the Fraunhofer structure factor peaks at a slightly lower wavenumber, $k_{\rm peak} \simeq 0.96 k_{\rm ADW}$. At strong coupling atomic-density waves change into a state in which spin-singlet dimers form an extended region of doubly occupied sites at the center of the trap, and thus a lot of nearly equivalent contributions come into play.

5.2 Spin unbalance and FFLO phase

In the preceding Section we have considered two-component Fermi gases with $N_\uparrow = N_\downarrow$, and the possibility of observing a Luther-Emery phase. A further type of tunability in atomic gases consists in creating in a controlled way a population imbalance between the two species in a Fermi gas and thus producing a mismatch between their Fermi spheres. This has currently been at the focus of intense experimental [86, 87, 88, 89, 90] and theoretical [160, 161, 162, 163, 164, 165, 166, 167, 168, 169, 170] work. Beyond a critical spin polarization the gas is reported to consist of a superfluid core surrounded by a shell of normal unpaired fermions. Indicators of the superfluid region are the presence of vortices in a rotating mixture as well as the fraction of condensed fermion pairs. The lattice-Hubbard model with attractive interactions (Sec 1.3) is able to account for such density profiles in an asymmetric Fermi mixture [171]. In the case of repulsive interactions one finds instead that the asymmetric mixture can phase-separate at strong coupling, provided that one allows a different trap strength for the two species [172].

There has been in parallel a flurry of theoretical activity on non-conventional superfluid states obtained from pairing in conditions where the Fermi surfaces do not match, first of all because the densities or the effective masses of

the two species are different [173, 161, 163, 165, 174, 175, 168]. This area has relevant implications not only for atom-gas physics, but also for condensed-matter physics (*e.g.* pairing between electron populations in different energy bands) and for quantum chromodynamics (*e.g.* in relation to the mass difference between the strange, up and down quarks leading to a difference in Fermi momenta in quark matter). In this context Liu and Wilczek have proposed a new state of matter, the so-called *interior-gap superconductivity*, in which the pairing interaction carves out a gap within the interior of a large Fermi sphere while the exterior surface remains gapless. This situation may arise when the mixture consists of fermions with heavy and light masses and the species interact attractively in the region of momentum space where the surface of the smaller Fermi sphere lies in the interior of the larger Fermi sphere.

Some 40 years ago Larkin and Ovchinnikov (LO) and Fulde and Ferrell (FF) proposed on purely theoretical grounds what amounted to a new type of superconducting state [80, 81, 84], now often referred to as the FFLO phase or as inhomogeneous superconductivity. In this state the superfluid condensate density varies in space. The FFLO phase can be viewed as a further generalization of the BCS state: whereas the building block of the BCS theory is the Cooper pair, where the paired electrons have momenta that are equal in magnitude and opposite in direction, in the FFLO phase a salient feature is that the momenta do not add to zero. Then an almost immediate consequence of the FFLO proposal is that the superfluid energy gap varies in space: the ground state is inhomogeneous, and even crystalline structure might be formed. In the original proposal, a "breached-pair state" was achieved by a combination of a spin-exchange field and a shift of the Fermi spheres in momentum space: down-spin fermions are stabilized by the exchange field, while only part of the states for spin-up fermions remain occupied and available for pairing.

This proposal has not yet been confirmed beyond reasonable doubt in condensed matter: its observation would necessitate the employment of high magnetic fields and type-II superconductors that should be essentially devoid of impurities. Studies of organic and heavy-fermion materials or layered

superconductors with magnetic fields parallel to the layers, and observations on surface superconductivity, vortex lattices, and Josephson junctions between FFLO and BCS materials have all been addressed in the recent literature [176, 177, 178, 179, 180]. The basic ideas of FFLO may also prove to play an important role in the future in nuclear physics, in relation to neutron-proton correlations and the likelihood of n-p Cooper-pair condensation, and in the theory of properties of pulsars as commonly identified with neutron stars.

Machida *et al.* [169] and Yang [92, 93] have examined the possibility that a spatially modulated superfluid FFLO state could be observed in quasi-1D fermion-atom gases. In a long cigar-shaped gas Machida *et al.* [169] find that a FFLO state with a position-dependent superfluid gap is energetically stable when the relative population difference of the two spin states lies above a critical value. Beyond this value the uniform BCS state would change into the modulated FFLO state, showing a periodic accumulation of the excess density of spin-up fermions at the zeroes of the gap. Yang [92, 93] has treated the inhomogeneous superfluid state in a system of weakly coupled chains and found a phase diagram in which the system goes from the uniform to the non-uniform state through a continuous transition of the commensurate-incommensurate type. His basic Hamiltonian for a single chain, that he treats by an exact bosonization method in contrast to the mean-field treatment of Machida *et al.*, contains terms describing the independent charge and spin sectors in a Luther-Emery liquid as well as a Zeeman coupling with a magnetic field. For further technical details the reader is referred to the original works.

The region of parameter space available for the FFLO phase in 3D space is however quite modest [84]. Quasi-one dimensional or strongly anisotropic 2D systems are, on the contrary, very well known to be good candidates for the realization of the FFLO phase [84, 91, 92, 93]. Examples of laboratory systems that have been successfully investigated in this context range from coupled chains, to heavy-fermion, organic, high-T_c, and $CeCoIn_5$ superconductors [85]. Although important results in one-dimensional systems have been obtained, to date there is no direct demonstration of the the oscillatory

behaviour of the pairing correlations other than in some limiting cases. For magnetic field close to Clogston-Chandrasekhar limit, Yang [92] has shown within a bosonization approach that a $1D$ system of fermions with attractive interactions is characterized by oscillating superconducting correlation functions that make it the $1D$ analogue of a bulk FFLO superconductor. Very recently Orso [181] and Hu *et al.* [182] have studied by means of the Bethe-*Ansatz* $1D$ polarized cold Fermi gases described by the Gaudin model and established the phase diagram. The identification of the partially polarized phase with the FFLO state was however made on the basis of the bosonization calculation close to the critical field or by resorting to mean-field calculations which were claimed to be accurate in 1D [182]. This section is devoted to demonstrate indeed that a spin-polarized attractive Fermi gas loaded in a $1D$ OL is always in a polarized superfluid state of the FFLO type [171]. We also discuss in detail what is the expected behavior of several observables, ranging from momentum distributions to density-density correlation functions, that are measured routinely in cold-atom laboratories.

We consider henceforth the Fermi-Hubbard Hamiltonian in Eq. (1.28) without harmonic confinement ($V_2 = 0$) but with atoms kept into the lattice by two hard walls located at the edges (*i.e.* at sites $\ell = 0$ and $\ell = L + 1$). According to Refs. [181, 182] the presence of a harmonic trapping potential induces phase-separated states in which partially-polarized locally-FFLO phases at the edges of the trap coexist with an unpolarized core of atoms at the trap center [181, 182]. The degree of spin polarization $\delta = (N_\uparrow - N_\downarrow)/(N_\uparrow + N_\downarrow)$ is changed below keeping always a constant number of "background" up-spin atoms $N_\uparrow$ and decreasing $N_\downarrow$ from $N_\downarrow = N_\uparrow$ (unpolarized case, *i.e.* $\delta = 0$) to $N_\downarrow = 0$ (fully polarized case, *i.e.* $\delta = 1$). At $\delta = 0$ the system belongs to the Luther-Emery universality class (as illustrated in previous Section 5.1); at $\delta = 1$ it describes a system of $N_\uparrow$ noninteracting fermions. Results reported below have all been obtained numerically through the DMRG method [71].

Due to the well-known (and yet cited) Coleman's theorem, in a $1D$ system no true long-range order is possible [30], and thus the ground-state expectation value of the pairing gap operator $\hat{\Delta}_\ell = \hat{c}_{\ell\downarrow}\hat{c}_{\ell\uparrow}$ is zero. Despite true

long-range order can not be achieved, the correlation function of the Cooper pair operator can decay with a power law at long distances

$$\mathcal{C}_{\ell\ell'} = \langle \hat{\Delta}_\ell^\dagger \hat{\Delta}_{\ell'} \rangle \;\simeq\; |\ell - \ell'|^{-(1+1/K_\rho)}$$

where $K_\rho \in [1,2]$ is an interaction-dependent dimensionless parameter [30]. Furthermore, Yang has shown [92, 93] that if this property holds for a system at $\delta = 0$ then the $\mathcal{C}_{\ell\ell'}$ acquires an oscillatory character for every $\delta > 0$. In other words an unpolarized system in Luther-Emery phase is driven to FFLO phase by an arbitrary polarization.

We start our investigations by looking at Cooper correlator $\mathcal{C}_{\ell\ell'=L/2}$, which measures real-space superfluid correlations between the central site $\ell' = L/2$ and all the other sites. In Fig. 5.4 we illustrate its spin-polarization dependence, at $U/t = 5$. For $\delta = 0$ the power-law decay of the $\mathcal{C}_{\ell\ell'=L/2}$ for $|\ell - L/2| \gg 1$ is clearly visible, and gives another proof of the system being in the Luther-Emery phase (Sec. 5.1). Once a finite polarization is introduced, the superfluid correlator exhibits a distinctive oscillatory character (enveloped by power-law decay). The most striking feature of this nodal structure is the number of simple zeroes, exactly equal to $N_\uparrow - N_\downarrow$.

The exceeding number of oriented particles shows up also in the local spin polarization profile which is directly measurable through phase-contrast imaging [89, 90]. Indeed, averaging over short distances, one can define an envelope profile which oscillates around the mean value $(N_\uparrow - N_\downarrow)/L$ with $(N_\uparrow - N_\downarrow)$ clear peaks (inset of Fig. 5.4). On the other hand the spin-summed site occupation profile $n_\ell = \sum_\sigma n_{\ell\sigma}$ exhibits $N_\downarrow$ maxima associated with the formation of $N_\downarrow$ spin-singlet pairs which are delocalized over the whole trap.

These features hint at the searched space dependent superfluidity, and so we now perform the Fourier transform ($\mathcal{F}.\mathcal{T}.$) of the Cooper correlator in order to make this statement more rigorous. The basis used is given by the eigenstates of the hopping term in Eq. (1.28) as explained in App. C:

$$\mathcal{C}(k_m, k_{m'}) = \mathcal{F}.\mathcal{T}.[\mathcal{C}_{\ell\ell'}] \equiv \sum_{\ell,\ell'=1}^{L} \mathcal{C}_{\ell\ell'} \varphi_m(\ell) \varphi_{m'}(\ell') \,, \tag{5.4}$$

where $\varphi_{k_m}(\ell) = [2/(L+1)]^{1/2} \sin(k_m \ell)$ with $k_m = \pi m/(L+1)$, m being an integer $\in [1, L]$. Of course, the mode with zero wave number is excluded

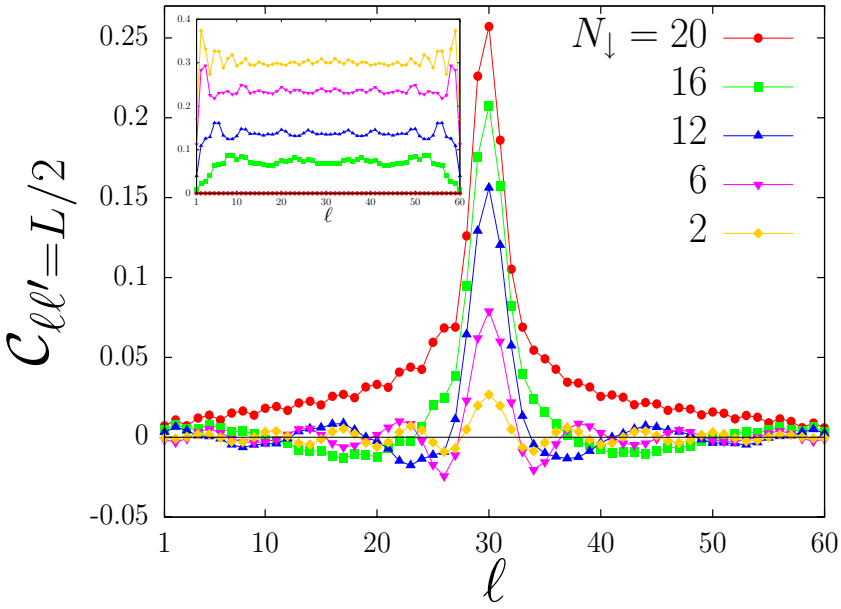

Figure 5.4: DMRG results for the pairing correlator $\mathcal{C}_{\ell\ell'=L/2}$ as a function of site position ℓ for a system with $N_\uparrow = 20$ fermions in $L = 60$ lattice sites and $U/t = 5$. The number of down-spin fermions is $N_\downarrow = 20, 16, 12, 6$ and 2. In the inset we show the local spin polarization $n_{\ell\uparrow} - n_{\ell\downarrow}$ as a function of ℓ.

from the allowed k_m values in a box. The lowest energy mode corresponds to k_1 (which tends to zero in the thermodynamic limit). The diagonal part of the matrix $\mathcal{C}(k_m, k_{m'})$ will be simply denoted by $\mathcal{C}(k_m) = \mathrm{diag}[\mathcal{C}(k_m, k_{m'})] \equiv \mathcal{C}(k_m, k_m)$. The direct term $\langle \hat{c}^\dagger_{\ell\uparrow}\hat{c}_{\ell'\uparrow}\rangle \langle \hat{c}^\dagger_{\ell\downarrow}\hat{c}_{\ell'\downarrow}\rangle$ gives contribution also in the noninteracting case $\mathcal{C}^{(0)}_{\ell\ell'} = \langle \hat{c}^\dagger_{\ell\sigma}\hat{c}_{\ell'\sigma}\rangle = \sum_{n=1}^{N_\sigma} \varphi_{k_n}(\ell)\varphi_{k_n}(\ell')$. In order to emphasize the impact of many-body effects in the superfluid correlations, in Fig. 5.5 we plotted the difference

$$\Delta\mathcal{C}(k_m) = \mathcal{C}(k_m) - \mathcal{C}^{(0)}(k_m)$$

At $\delta = 0$ $\mathcal{C}(k_m)$ possesses a very narrow peak at k_1, signaling quasi-long-range superfluid order of the conventional Bardeen-Cooper-Schrieffer (BCS) type. For a finite δ, instead, $\mathcal{C}(k_m)$ has a local minimum at k_1 and a well-defined peak appears at a wave number $q_{\mathrm{FFLO}} = k_1 + |k_{\mathrm{F}\uparrow} - k_{\mathrm{F}\downarrow}|$,

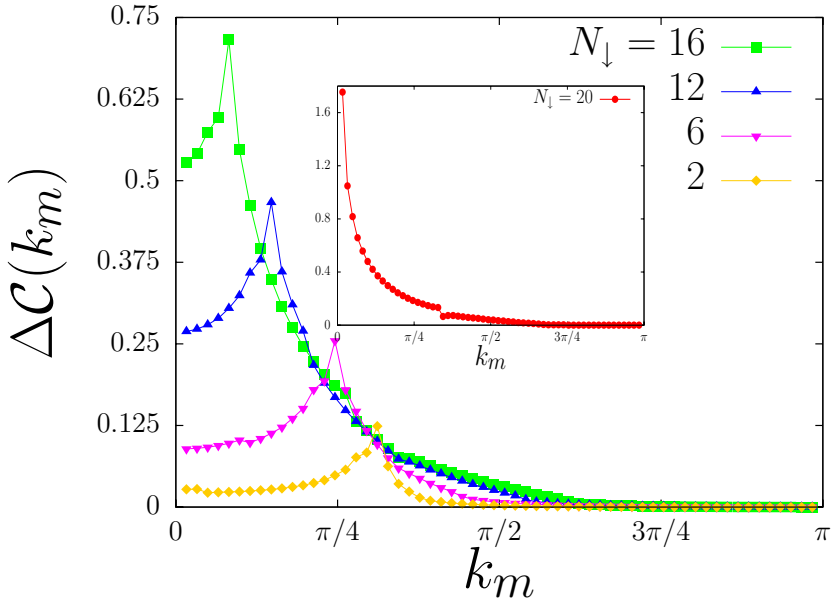

Figure 5.5: Interaction contribution to the momentum-space pairing correlator $\Delta\mathcal{C}(k_m)$ as a function of wave number $k_m = \pi m/(L+1)$ for the same system parameters as in the top panel. Note the well-defined peaks at $q_{\rm FFLO}$. In the inset we show $\Delta\mathcal{C}(k_m)$ for the unpolarized system with $N_\uparrow = N_\downarrow = 20$, which shows a narrow peak at k_1. The thin solid lines are just a guide for the eye.

$k_{{\rm F}\sigma} = \pi N_\sigma/(L+1)$ being the spin-resolved Fermi wave numbers. The peak at $q_{\rm FFLO}$ in the Fourier transform of the Cooper correlator, which is a direct consequence of the simple real-space nodal structure discussed above, is a clear-cut signal of FFLO pairing.

While Fig. 5.5 clearly states the emergence of a peak in the momentum distribution in the position predicted by FFLO, it is now interesting to analyze the dependence of its visibility on the interaction strength U/t. Hence we fix the polarization to be $\delta = 0.25$ (i.e. $N_\uparrow = 20, N_\uparrow = 12$) in a chain with $L = 60$ sites, with the coupling spanning from very weak $U/t = 0.2$ to very strong $U/t = 50$. In Fig. 5.6 we illustrate the dependence of $\Delta\mathcal{C}(k_m)$ on the interaction strength. On decreasing U/t the quasi-long-range FFLO order (*i.e.* the height of the peak at $q_{\rm FFLO}$), which is emphatically strong for large

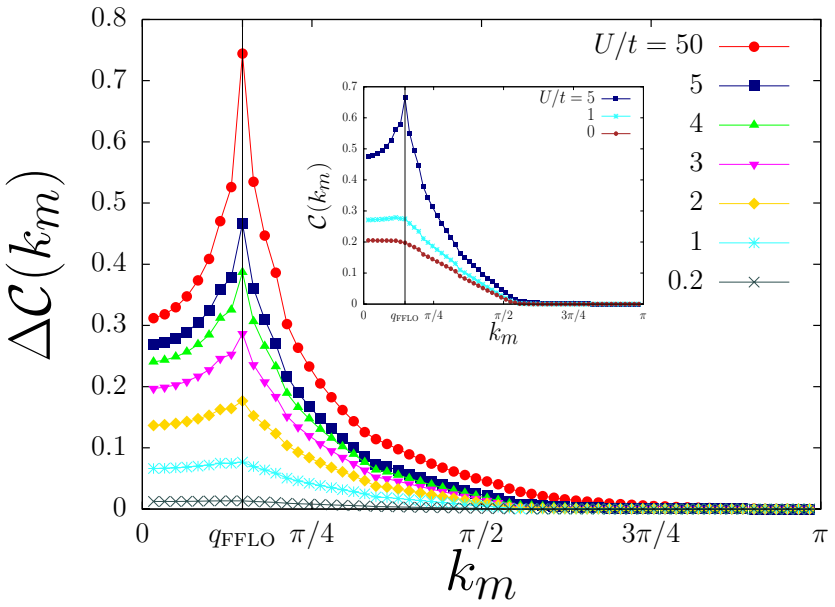

Figure 5.6: Interaction contribution to the momentum-space pairing correlator $\Delta\mathcal{C}(k_m)$ as a function of k_m, for $N_\uparrow = 20$, $N_\downarrow = 12$ ($\delta = 25\%$), and $L = 60$. The interaction strength U/t is decreased from 50 to 0.2. In the inset we show $\mathcal{C}(k_m)$ for $U/t = 5, 1$, and 0.

U/t, survives all the way down to the weak coupling regime. This can be quantified better by analyzing the size of the anomaly at $k_m = q_{\rm FFLO}$, which we quantify by the (discrete) derivative at $q_{\rm FFLO}$

$$\Gamma = \mathcal{C}\left[q_{\rm FFLO} + \delta k\right] - \mathcal{C}\left[q_{\rm FFLO} - \delta k\right] . \tag{5.5}$$

where $\delta k = \pi/(L+1)$. In Fig. 5.7 we plot Γ as a function of $U/t \leq 5$. In this range Γ decreases in a smooth fashion to its noninteracting value as U/t is decreased to zero. In other words, for every finite δ, $\mathcal{C}(k_m)$ tends uniformly and smoothly to its noninteracting value $\mathcal{C}^{(0)}(k_m)$ as U/t is decreased towards zero. For sufficiently large values of U/t the FFLO phase can also be characterized by the peak visibility defined by

$$\nu = \frac{\mathcal{C}(q_{\rm FFLO}) - \mathcal{C}(k_1)}{\mathcal{C}(q_{\rm FFLO}) + \mathcal{C}(k_1)} . \tag{5.6}$$

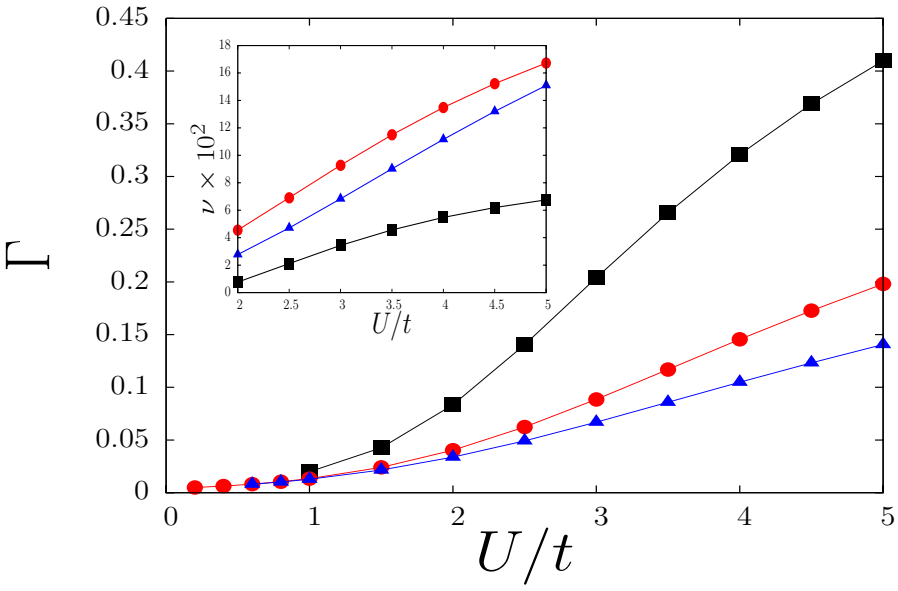

Figure 5.7: The FFLO anomaly Γ in the superfluid correlator [see Eq. (5.5)] as a function of U/t for $N_\uparrow = 20$ and $N_\downarrow = 18$ (squares), $N_\downarrow = 12$ (circles), and $N_\downarrow = 6$ (triangles). Inset: peak visibility ν [see Eq. (5.6)] as a function of $2 \leq U/t \leq 5$ for the same system parameters as in main body of the figure (ν is about 30% at $U/t = 50$). The thin solid lines are just a guide for the eye.

This quantity is plotted in the inset of the bottom panel in Fig. 5.7.

Finally, as usual, we propose here how to confirm the results of the present section by means of some experimentally measurable quantities. As exposed in Sec. 1.1.2, in cold-atom laboratories one can essentially measure the momentum distribution function (MDF) and the density-density correlation functions. By analyzing the expanding density profiles in a time-of-flight experiment one can construct back the original MDF of the system. These should be reminiscent of the double sphere structure, and thus make the expected value of q_{LOFF} measurable. Although momentum distributions carry informations about Fermi spheres and gaps, perhaps the most interesting quantity to observe is given by density-density correlation function:

$$\mathcal{D}_{\ell\sigma,\ell'\sigma'} = \langle \hat{n}_{\ell\sigma}\hat{n}_{\ell'\sigma'}\rangle - \langle \hat{n}_{\ell\sigma}\rangle\langle \hat{n}_{\ell'\sigma'}\rangle \ . \tag{5.7}$$

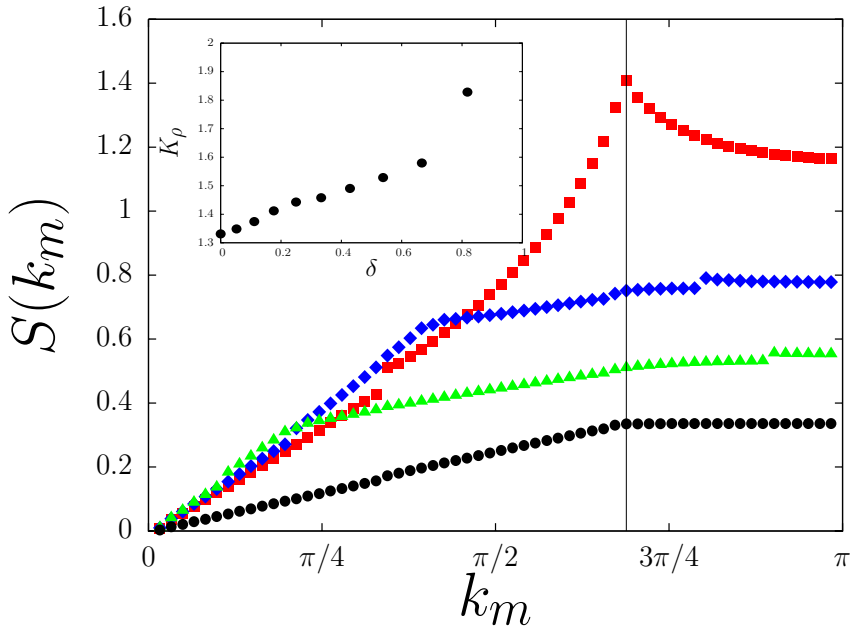

Figure 5.8: The spin-summed structure factor $S(k_m)$ as a function of k_m for $U/t = 5$, $N_\uparrow = 20$ and $N_\downarrow = 20$ (squares), $N_\downarrow = 12$ (diamonds), $N_\downarrow = 6$ (triangles), and $N_\downarrow = 0$ (circles). Inset: K_ρ as a function of δ for the same system parameters as in the main body of the figure.

According to Altman, Demler, and Lukin [49] it could carry signatures of many-body correlation effects that are not detectable through a measurement of $n_\sigma(k_m)$. Indeed, momentum distribution of Cooper pairs $\langle \mathcal{C}(k) \rangle = \int e^{ikx} \langle \Psi_\uparrow^\dagger(x) \Psi_\downarrow^\dagger(x) \Psi_\downarrow(0) \Psi_\uparrow(0) \rangle dx$ can be written as $\langle n_{bf}(k) \rangle = \int \langle n_\downarrow(k-p) n_\uparrow(p) \rangle dp/(2\pi)$. We note that it is different from $\int \langle n_\downarrow(k-p) \rangle \langle n_\uparrow(p) \rangle dp/(2\pi)$, thus the presence of the "pairing" results in nontrivial noise correlations in time-of-flight images.

Before concluding, we would like to illustrate the expected behavior of the spin-summed static structure factor

$$S(k_m) = \sum_{\sigma,\sigma'} \mathrm{diag}\{\mathcal{F}.\mathcal{T}.[\mathcal{D}_{\ell\sigma,\ell'\sigma'}]\}$$

, i.e. the Fourier transform of the spin-resolved real-space density-density

correlations

$$\mathcal{D}_{\ell\sigma,\ell'\sigma'} = \langle \hat{n}_{\ell\sigma}\hat{n}_{\ell'\sigma'}\rangle - \langle \hat{n}_{\ell\sigma}\rangle\langle \hat{n}_{\ell'\sigma'}\rangle$$

. On the other hand, it can be calculated as the sum over all frequencies of the dynamic structure factor that can be measured through Bragg spectroscopy or Fourier sampling of time-of-flight images [183]. In Fig. 5.8 we show the dependence of $S(k_m)$ on the spin-polarization δ. Note that for $\delta = 0$ it has a peak at $k_m = 2k_{\mathrm{F}\uparrow} = 2k_{\mathrm{F}\downarrow}$ that signals real-space atomic-density waves [82, 184]. With increasing spin-polarization this peak disappears. Another important feature in these plots is the linear behavior $S(k_m) \to K_\rho k_m/\pi$ [184] for $k_m \ll k_L$, which is solely controlled by the Luttinger-liquid parameter K_ρ introduced above. This linear behavior persists up to $2k_{\mathrm{F}\downarrow}$ for every δ and is related to the power-law decay of $\sum_{\sigma,\sigma'} \mathcal{D}_{\ell\sigma,\ell'\sigma'}$ at large distances. The spin-polarization dependence of K_ρ is plotted in the inset to Fig. 5.8.

Chapter 6

Bose-Fermi mixtures

Recent developments in the cooling and trapping of atomic gases open exciting opportunities for experimental studies of interacting systems under well-controlled conditions. Using Feshbach resonances[185, 186, 187, 188] and/or optical lattices[15, 17] it is possible to reach strongly interacting regimes, where correlations between atoms play a crucial role. The effect of interactions is most prominent for low dimensional systems, and recent experimental realization[21, 20] of a strongly interacting Tonks-Girardeau (TG) gas of bosons opens new perspectives in experimental studies of strongly interacting systems in 1D. In particular, one can experimentally study the behavior of Bose-Fermi (BF) mixtures[189, 190, 31, 191, 192, 193, 33, 34] in 1D. Due to the lack of candidate systems in traditional solid state experiments, this topic did not attract sufficient theoretical attention until recently. By now, properties of 1D BF mixtures have been investigated using mean-field approximation [194], Luttinger liquid (LL) formalism [195, 196, 197, 198], exact solutions [199, 200, 201, 202], and numerical methods [203, 204, 205, 206, 207, 208]. Mean-field approximation is unreliable in 1D, LL approach describes the phase diagram in terms of universal parameters which are hard to relate to experimentally controlled parameters, and exact solution is restricted only to certain region of parameter space. Most of the numerical work so far considered BF mixtures in optical lattices with fillings of the order of unity. In such regime the analysis of phase diagram is complicated, since the physics of Mott transition plays an important role. In this article,

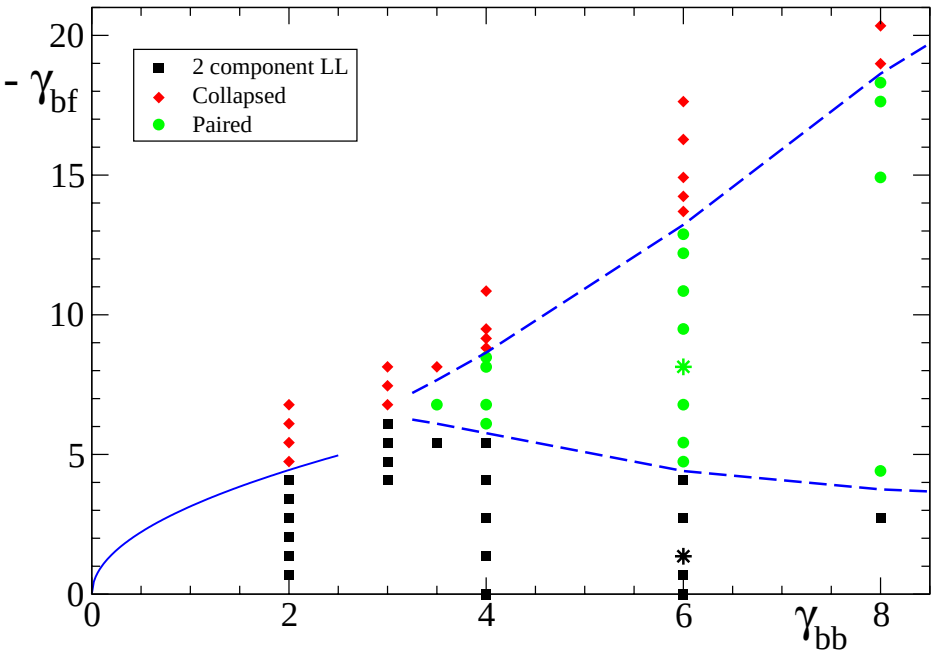

Figure 6.1: Phase diagram for K-Rb mixture with equal density of bosons and fermions. γ_{bb} and γ_{bf} are defined by Eq. (6.2), and we show here the attractive side ($\gamma_{bf} < 0$). Different symbols and colors identify the three different phases involved: squares are in the two-component Luttinger liquid (LL) state, diamonds are in the collapsed state, whereas circles stand for the paired phase we found in between. Sample points, considered in Figs. 6.2, 6.3 and 6.4, are identified by stars. Solid line is the mean-field prediction [194], which should be good for small γ_{bb} and matches well the data for smallest γ_{bb} available. Dashed lines are tentative boundaries between the different phases. Notice the existence of a threshold in γ_{bb} to get the paired phase.

we are mainly interested in the properties of 1D mixtures without optical lattice, for the regime of parameters directly relevant to current K-Rb experiments [209, 210, 211] Our main result is summarized in Fig. 6.1. For K-Rb mixture with equal density of bosons and fermions, we find an evidence for the "pairing" phase, discussed in Ref.[195].

The general Hamiltonian of 1D BF mixture is given by

$$\begin{aligned}\mathcal{H} &= \int_0^L dx(\frac{\hbar^2}{2m_b}\partial_x\Psi_b^\dagger\partial_x\Psi_b + \frac{\hbar^2}{2m_f}\partial_x\Psi_f^\dagger\partial_x\Psi_f) \\ &+ \int_0^L dx(\frac{1}{2}g_{bb}\Psi_b^\dagger\Psi_b^\dagger\Psi_b\Psi_b + g_{bf}\Psi_b^\dagger\Psi_f^\dagger\Psi_f\Psi_b) \ , \end{aligned} \tag{6.1}$$

where Ψ_b, Ψ_f are boson and fermion operators, m_b, m_f are the masses, and g_{bb}, g_{bf} are boson-boson and boson-fermion interaction strengths. Well away from confinement induced resonances[68], 1D interactions are given by $g_{bb} = 2\hbar\omega_{b\perp}a_{bb}, g_{bf} = 2\hbar a_{bf}\omega_{b\perp}\omega_{f\perp}(m_b + m_f)/(\omega_{b\perp}m_b + \omega_{f\perp}m_f)$, where $\omega_{b\perp}, \omega_{f\perp}$ are transverse confinement frequencies, and a_{bb}, a_{bf} are 3D scattering lengths. g_{bb} and g_{bf} can be controlled by changing transverse confining frequencies, or by varying scattering lengths using Feshbach resonances [185, 186, 187, 188]. For K-Rb mixture in the absence of magnetic field, $a_{bb} >$ and $a_{bf} < 0$, so in this article we will study the regime when bosons and fermions attract. Phases of Hamiltonian (6.1) in most general case depend on four dimensionless parameters, which we choose to be $m_b/m_f, n_b/n_f$,

$$\gamma_{bb} = \frac{m_b g_{bb}}{\hbar^2 n_b} \ \text{ and } \ \gamma_{bf} = \frac{\sqrt{m_b m_f}g_{bf}}{\hbar^2\sqrt{n_b n_f}}. \tag{6.2}$$

Here n_f, n_b are fermion and boson densities, and γ_{bb} and γ_{bf} are dimensionless interaction parameters. Similar to Lieb-Liniger model[212], strongly interacting regime corresponds to $\gamma_{bb}, |\gamma_{bf}| \gg 1$. If $\gamma_{bb} < 0$ (attractive bosons), the system is always unstable towards boson collapse. For $\gamma_{bb} > 0$ the system can still collapse for $\gamma_{bf} < 0$, or phase separate for $\gamma_{bf} > 0$ [195]. If these two scenarios are not realized and densities of bosons and fermions are incommensurate, then from LL theory [195, 196, 197] one expects a two-component LL, with power law decay of all correlations. If densities are commensurate, one can expect [195, 198] a nontrivial pairing, resulting in the exponential decay of certain correlation functions and in the opening of the gap. In what follows we will concentrate on the latter case for K-Rb mixture, so we will fix $n_b/n_f = 1, m_b/m_f = 87/40$ and consider negative γ_{bf}.

For numerical purposes we consider the discretized version of Hamiltonian (6.1) to be an open boundary chain with unity lattice constant and L

sites. Similar to Lieb-Liniger model being a low filling fraction limit of Bose-Hubbard model [213, 214], Hamiltonian (6.1) is the low filling fraction limit of the following lattice Hamiltonian

$$\begin{aligned}\mathcal{H}_L &= -t_b \sum_{i=1}^{L-1} \left(b_i^\dagger b_{i+1} + h.c. \right) - t_f \sum_{i=1}^{L-1} \left(f_i^\dagger f_{i+1} + h.c. \right) \\ &+ \sum_{i=1}^{L} \left(\frac{U_{bb}}{2} b_i^\dagger b_i (b_i^\dagger b_i - 1) + U_{bf} b_i^\dagger b_i \; f_i^\dagger f_i \right) \end{aligned} \tag{6.3}$$

We note, that many different lattice Hamiltonians give continuum Hamiltonian (6.1) in low density limit, and the choice of lattice Hamiltonian is not unique. For low fillings ν_b and ν_f, dimensionless interaction parameters are given by

$$\gamma_{bb} \approx \frac{U_{bb}}{2 t_b \nu_b} \;\text{ and }\; \gamma_{bf} \approx \frac{U_{bf}}{2\sqrt{t_b \nu_b t_f \nu_f}}. \tag{6.4}$$

Most of our simulations were performed at densities $\nu \simeq 1/4$, but some of the results were checked for $\nu \simeq 1/8$. To check that the effects that we are observing are not related to commensurability, we also performed some simulations for filling fractions $\nu = 23/96$ and $\nu = 25/96$. The fact that we use finite filling fractions only slightly changes Eqs. (6.4), but doesn't affect the phase diagram qualitatively. The expectation values $\langle \ldots \rangle$ of one- and two-body operators over the ground state of $\mathcal{H}_L$ have been evaluated by means of the DMRG method (App.B, which provides practically exact solution for any value of the couplings and allows to measure correlation functions with both statistics on the equal footing. We used up to $L = 96$ chains, with local dimension $d = 10$ (up to 4 bosons per site) and truncation up to $m = 256$ states. Discarded probabilities amount to less than $\varepsilon = 5 * 10^{-7}$. Small values of γ_{bb} with weak interparticle interactions, however, are not easy to study with this method, since high occupation number for bosons should be taken into account. We thus resorted to mean-field predictions in this area.

Local density profiles were measured and are plotted in Fig.6.2 for two sample points (stars in Fig.6.1). In our simulations we calculated the following correlation functions: bosonic Green function $G_b(i,j) = \langle b_i^\dagger b_j \rangle$, fermionic Green function $G_f(i,j) = \langle f_i^\dagger f_j \rangle$ and "pairing" correlation function $G_{bf}(i,j) =$

$\langle \Delta_i^\dagger \ \Delta_j \rangle = \langle b_i^\dagger f_i^\dagger f_j b_j \rangle$, where "pairing" operator is described by $\Delta_j = f_j b_j$. Their values have been plotted in Fig.6.3 for the same sample points as before. Fourier transforms of bosonic and fermionic Green functions give respective momentum distributions, while Fourier transform of $G_{bf}(i,j)$ is related to momentum distribution of composite particles. Such momentum distributions are shown in Fig.6.4. In order to calculate them, it is crucial to choose the properly defined free-particle eigenmodes due to open boundaries, $\phi_k(j) = \sqrt{2/(L+1)}\ \sin(k\ j)$ with $k = n\frac{\pi}{L+1} (n = 1, ..., L)$. In addition to these correlation functions, density-density correlations $D_{\alpha,\beta} = \langle n_\alpha(i) n_\beta(j) \rangle - \langle n_\alpha(i) \rangle \langle n_\beta(j) \rangle$ were measured as well. Here α and β can take any value from $\{b, f\}$. For finite size simulations, subtraction of the non-connected part is necessary, since open boundary conditions give density profiles with Friedel oscillations. Examining of density correlations without this substraction could lead to misinterpretation of results.

To extract the long-range behavior of correlation functions, we restricted the analysis to the regions far away from the boundaries. In order to check whether a certain correlation function has a power-law or exponential decay, it is sufficient to test the simplest power-law and exponential forms

$$G_*(x) = \left.\begin{array}{c} A_*\ e^{-x/d_*} \\ B_*\ |x|^{-\alpha_*} \end{array}\right\} \ \sin(\omega_* x + \varphi_*), \tag{6.5}$$

where the oscillating term is absent for the pure bosonic Green function. The fermionic oscillation frequency is correctly given by the fermionic density $\omega_f = \pi\nu_f \simeq \pi/4$. The exact value is given by the density in the system bulk, which is slightly larger due to open boundary conditions. For convenience, let us introduce the Luttinger parameters K_b, K_f and K_{bf}, which are related to α_b, α_f and α_{bf} in Eq.(6.5) as $\alpha_b = 1/(2K_b), \alpha_{f(bf)} = (K_{f(bf)} + 1/K_{f(bf)})/2$. Eq. (6.5) gives the asymptotic form of the correlation functions in the thermodynamic limit far from the boundaries. To quantitatively extract the Luttinger parameters K_* for finite L, one has to take into account carefully the effects of open boundary conditions (OBCs). We refer the reader to the detailed analysis of Ref.[215] and recall here that $G_*(i,j)$ will depend on chord functions $d_L(x) = d(x|2(L+1)) = (2(L+1)/\pi)\ \sin(\pi x/2(L+1))$ of all $2i, 2j, i-j, i+j$. The form of the correlation function which needs to be

fitted to extract Luttinger parameters are given by (G_{bf} is modified in the same way as G_f)

$$G_b(i,j) \propto (d_L(2i)d_L(2j))^{\frac{1}{4K_b}} \ (d_L(i+j)d_L(i-j))^{-\frac{1}{2K_b}}, \tag{6.6}$$

$$\begin{aligned} G_f(i,j) \propto & (d_L(2i)d_L(2j))^{-\frac{1}{4}(K_f-\frac{1}{K_f})} \ (d_L(i+j)d_L(i-j))^{-\frac{1}{2}(K_f+\frac{1}{K_f})} \\ & \big[d_L(i+j)^{K_f}(-1)^{sign(i-j)}A_0\sin(\pi\omega(i-j)+\varphi_0) \\ & +d_L(i-j)^{K_f}A_1\sin(\pi\omega(i+j)+\varphi_1)\big]. \end{aligned} \tag{6.7}$$

We start our tour around the phase diagram by looking at small attractions between bosons and fermions. The sample point $\gamma_{bb} = 6.0$ and $\gamma_{bf} = -1.36$ is considered in the first panels of Figs. 6.2-6.3. Looking at density profiles in Fig. 6.2, one can notice that both the atomic species spread out around the whole lattice, exhibiting Friedel oscillations due to hard walls at the boundaries. Wings are cut off for the sake of plot clearness. Due to attraction between bosons and fermions such oscillations are in-phase, but the values of the two densities differ on the order of the second digit. Coming to correlation functions (illustrated in Fig.6.3, 1st panel), one can easily recognize a power-law decay for both the bosonic Green function $G_b(i,j)$ (black circles) and the (oscillating) fermionic Green function $G_f(i,j)$ (red squares). "Pairing" correlation function $G_{bf}(i,j)$ exhibits power-law behavior as well. Thus this phase is a two-component Luttinger liquid. Such phase has two gapless sound modes, and all correlation functions have algebraic decay.

Increasing the interspecies attraction for small γ_{bb} will lead to a collapse . More precisely, bosons form a small region with high density where fermions will be attracted up to Pauli allowed density $\nu = 1$. Existence of such maximal density is an artifact of our lattice discretization, and is not expected in the absence of a lattice. According to mean-field theory [194], the first order phase transition between the two component LL and the collapsed phase should take place as boson-fermion attraction is increased for any value of the boson-boson interaction. Within mean-field theory transition line is given by $\gamma_{bf}^2 = \gamma_{bb}\pi^2$, and it is shown in Fig. 6.1 as a solid line. The result of mean field calculation agrees well with the data set for smallest γ_{bb} considered. For large γ_{bb}, mean-field calculation is not expected to give an adequate description of the system, and for sufficiently large γ_{bb} and attractive fermion-

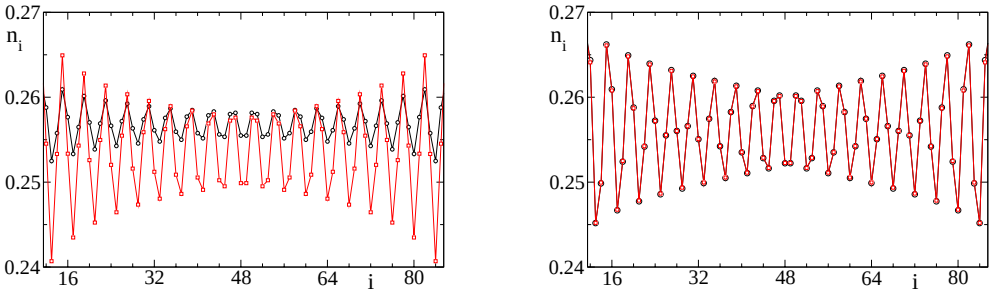

Figure 6.2: Density profiles: black circles are bosons, red squares fermions. In the first panel we show results for a typical point in the usual mixed phase ($\gamma_{bb} = 6.0, \gamma_{bf} = -1.36$). Both the species are spread around the chain and no pinning is evident between densities. In the second panel, the "locking" of densities for the paired phase is evident. Right panel corresponds to the values $\gamma_{bb} = 6.0, \gamma_{bf} = -8.14$. Friedel oscillation frequency is in both cases given, as expected, by $\omega_* = \pi\nu_*$ with $\nu_* \simeq 1/4$ being the species' density in the bulk of the system.

boson term $\gamma_{bf} < 0$ the system belongs to a third intermediate phase, see Fig.6.1 for a sketch. The population distributions and the correlations for a sample point in this intermediate region of parameters are plotted in the second panels of Figs. 6.2-6.3. A strong locking of one density profile on top of the other is the most striking feature in Fig. 6.2B. Indeed, not only the Friedel oscillations are in phase like it was in Fig. 6.2A, but the difference between boson and fermion local densities is bounded to be less than 10^{-4} in the bulk, which is two orders of magnitude smaller than in the case of two-component LL. Furthermore, the strong locking of the two densities suggest that a composite particle made by a boson and a fermion, polaron, could be the new elementary object to look at. In the second panel of Fig.6.3 all three types of correlation functions are plotted: G_b (black circles), G_f (red squares) and G_{bf} (green diamonds). In contrast to two-component LL, single species Green functions clearly exhibit an exponential decay with a correlation length of few sites. But the "pairing" correlations G_{bf} still decay slowly as a power-law. Taking the open boundary conditions into account as described before, we get a Luttinger parameter $K_{bf} = 0.95 \pm 0.02$. As shown in Fig. 6.4, such a dramatic change in the decay properties of correlation

functions is witnessed by momentum distributions of the two species (and the composite one). Indeed, the Fermi step of individual fermionic atoms is no more there as it is in the case of two-component LL, and also the once peaked Bose distribution is considerably spread out now. In contrast, we highlight that momentum distribution of paired composite particles clearly exhibit a Fermi step around $k_{bf} = \pi/4$ consistently with the filling. Thus, this phase can be understood as the "paired" phase of bosons and fermions. Existence of such "paired" phase has been predicted in Ref. [195] based on LL theory arguments for mixture with equal masses for large γ_{bb}. Indications of the existence of such phases have also been briefly presented in Ref. [208], but the phase diagram hasn't been studied in detail. Fig. 6.1 presents the phase diagram for the K-Rb mixture, and shows that "paired" phase can be realized for moderately strong Bose-Bose interactions. Boundaries between different phases were determined comparing algebraic and exponential fits of single species correlation functions, and by observing the "locking" of one density profile on the top of the other.

Looking at density-density correlations, one can address another distinctive feature of "paired" phase. As predicted in Ref. [195], oscillating part of all three density correlation functions $D_{\alpha,\beta}(x)$ ($b-b$, $f-f$, $b-f$) decay with distance with the same algebraic exponent:

$$D_*(x)|_{2\pi\nu} \sim |x|^{-r} \sin(\omega x + \varphi). \tag{6.8}$$

The frequency of oscillations is twice the particle density $\omega \simeq 2\pi\nu \simeq \pi/2$. As pointed out by Ref. [195], exponent r should be intimately related to the Luttinger parameter for paired particles K_{bf}, i.e. $r = 2K_{bf}$ (we note that $K_{bf} = K_+/2$, where K_+ in defined in Ref. [195]). Thus parameter K_{bf} can be extracted independently from $D_{\alpha,\beta}$, using the fitting procedure which takes OBC into account. We checked that all density-density correlations decay with the same exponent, and extracted value of K_{bf} equals 0.97 ± 0.02. This is in good agreement with the pairing correlation fits (see before) which give the value 0.95 ± 0.02. Based on all evidence, we can unambiguously state that we have shown the existence of the "paired" phase predicted by Cazalilla and Ho [195], even with unequal masses of the two atomic species.

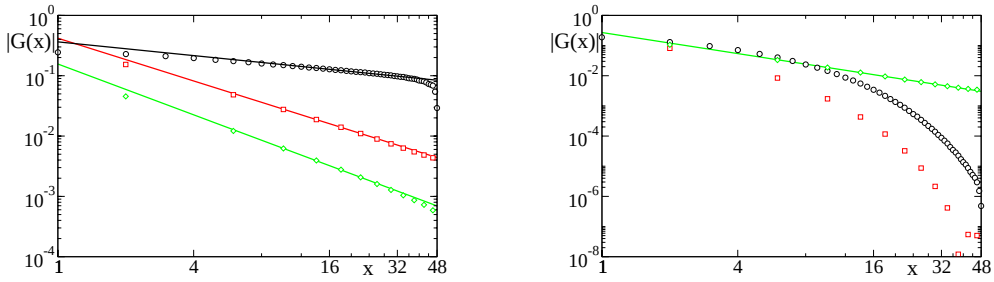

Figure 6.3: Correlation functions: same sample points as in Fig.6.2, same color code. For clarity, oscillations are not shown and only the decay of the envelope functions is presented. $G(x)$ means here $G(L/2, L/2+x)$. Green diamonds stand for composite particles created by $\Delta^\dagger = b^\dagger f^\dagger$. In the first panel (two-component Luttinger liquid state) all the three types of correlation functions exhibit an algebraic decay. For bosons $G_b(x) \propto x^{-1/(2K_b)}$ with $K_b = 1.45 \pm 0.05$, whereas for fermions $G_f(x) \propto x^{-1/(2K_f)-K_f/2}$ with $K_f = 0.98 \pm 0.02$. On the other hand, for "paired" phase (second panel) only G_{bf} shows an algebraic decay $\simeq x^{-1/(2K_{bf})-K_{bf}/2}$ with the Luttinger parameter $K_{bf} = 0.95 \pm 0.02$, while G_b and G_f decay exponentially with distance.

The stability of such a paired phase against the population unbalance between the two species was also studied (see Fig.6.5). It turns out that for small enough differences, the locking of the densities survives in the sides of the box, whereas in the middle a peak or a hole arises in the bosonic profile. A subsequent curvature in the fermionic profile is also visible. With respect to the single particle Green function, the power-law decay in composite correlations is preserved, whereas individual species still exhibit exponential suppression. For larger unbalance, the system become unstable against collapse, as expected, and the paired phase is washed out.

Let us now concentrate on possible experimental techniques to detect the "paired" phase. One notable feature, which distinguishes "paired" phase from two-component LL phase, is the presence of the gap for out-of-phase density modes. Deep in the "paired" phase, the energy scale for the gap is set by Fermi energy $\sim \pi^2\hbar^2 n^2/(2m)$. The presence and the size of the gap can be measured using RF spectroscopy [158, 29]. Energies of sound

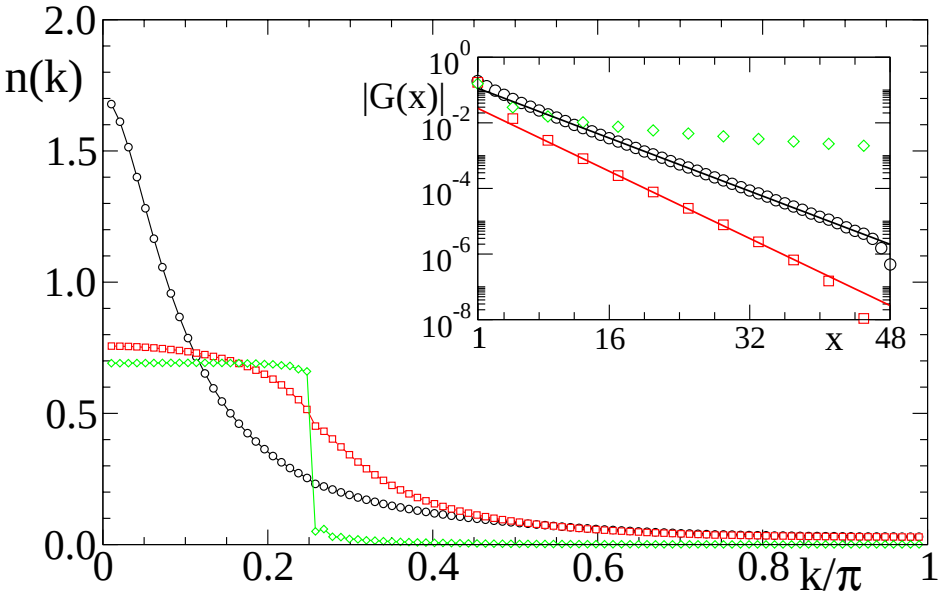

Figure 6.4: Momentum distributions in the "paired" phase. Same color code of correlations as in Fig.6.3. We highlight the washing out of the Fermi surface for individual ^{40}K and the wide broadening of the bosonic ^{87}Rb distribution. On the contrary, a sharp step-like feature in the composite particles' mode occupation is present around $\pi/4$, indicating the algebraic decay of "pairing" correlation function $G_{bf}(x)$. Bosonic and fermionic particle correlations decay exponentially (see the inset, which is the same data as in the second panel of Fig.6.3, but in log-linear scale).

modes can be measured using Bragg scattering [216], and "paired" phase has only one sound mode, as opposed to two-component LL phase, which has two modes. Disappearance of the out-of-phase sound mode also affects qualitatively the response of the system to the variations of the external potential, since out-of-phase collective mode in external trap is much higher in energy compared to in-phase mode. Fourier transforms of bosonic and fermionic correlation functions, $\langle n_b(k)\rangle = \int e^{ikx} G_b(x)dx$ and $\langle n_f(k)\rangle = \int e^{ikx} G_f(x)dx$, are given by momentum distributions, shown in Fig. 6.4. They can be measured using ballistic time-of-flight experiments, since during ballistic expansion momentum distributions get mapped into real space

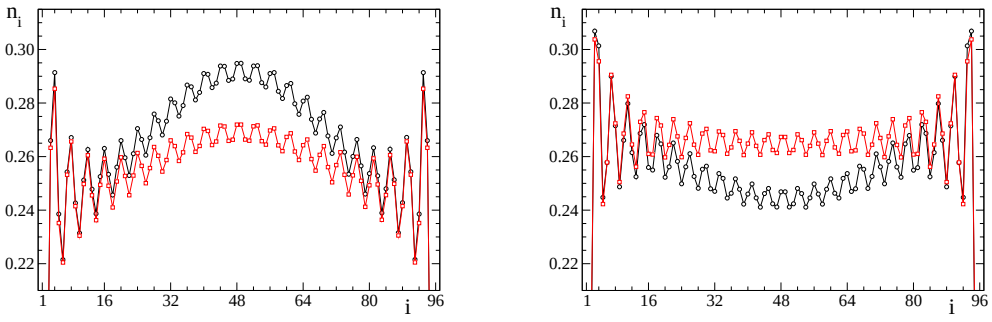

Figure 6.5: Density profiles in the presence of an extra Boson (first panel) or Fermion (second one). The two species profiles retain their pairing in the wings and exhibit a peak or a hole in the bosonic density in the center of the box. A consequent curvature of the fermionic profile is also addressable.

densities [20]. Momentum distribution of composite particles $\langle n_{bf}(k)\rangle = \int e^{ikx}\langle\Psi_b^\dagger(x)\Psi_f^\dagger(x)\Psi_f(0)\Psi_b(0)\rangle dx$ has a strong Fermi step, and can be written as $\langle n_{bf}(k)\rangle = \int\langle n_b(k-p)n_f(p)\rangle dp/(2\pi)$. We note that it is different from $\int\langle n_b(k-p)\rangle\langle n_f(p)\rangle dp/(2\pi)$, thus the presence of the "pairing" results in nontrivial noise correlations in time-of-flight images [49]. Finally, we would also like to point out the method to measure the correlation functions based on interference of two independent 1D clouds [217, 218]. For bosons (fermions) average of the square of interference signal $\langle|A_{b(f)}(L)|^2\rangle$ of two segments of length L is related to an integral of the Green's function as $\langle|A_{b(f)}(L)|^2\rangle = \int_0^L\int_0^L dxdyG_{b(f)}(x-y)^2$. Interference signal appears at wave vectors $Q_{b(f)}$, which depend on masses of interfering particles. If one measures $\langle|A_{b(f)}(L)|^2\rangle$ as a function of L, then in principle dependence of $G_{b(f)}(x)$ on distance x can be extracted, since $G_{b(f)}(L)^2 = \frac{1}{2}\frac{\partial^2\langle|A_{b(f)}(L)|^2\rangle}{\partial L^2}$. Same technique can be used also to measure $G_{bf}(x)$, but in this case the information will be contained in the oscillations of the product of Bose and Fermi densities at wave vector Q_b+Q_f. Since in "paired" phase $G_{bf}(x)$ decays much slower with distance than $G_b(x)G_f(x)$, "paired" phase will be characterized by strong correlations in the fluctuations of bosonic and fermionic interference fringes.

To summarize, we have considered one dimensional Bose-Fermi mixture

with equal densities and unequal masses using DMRG. For the mass ratio of $K - Rb$ mixture and attraction between bosons and fermions, we determined the phase diagram, which is shown in Fig. 6.1. For weak boson-boson interactions, there is a direct transition between two-component Luttinger liquid and collapsed phases as the boson-fermion attraction is increased. For strong enough boson-boson interactions, we find an intermediate "paired" phase of Ref. [195], which is a single-component Luttinger liquid of composite particles. We investigated correlation function of such "paired" phase, and discussed various experimental techniques which can be used to detect it.

Appendix A

Quantum MonteCarlo simulations

We give here some of the technical details of the mapping from the QPM to a $(2+1)D-XY$ model exploited in Chapters 2 - 3. The latter one is particularly easy to be simulated numerically: the state of the system and the effective action are both expressed in terms of phases on a $3D$ lattice. Being n and φ canonically conjugated, it is possible to represent n as $-\imath\frac{\partial}{\partial\varphi}$ and get the so-called quantum rotor Hamiltonian. For the sake of simplicity we consider a diagonal capacitance matrix.

$$\begin{aligned} \mathcal{H} &= \mathcal{H}_t + \mathcal{H}_U \\ \mathcal{H}_U &= -\frac{U}{2}\sum_{\mathbf{r}}\frac{\partial^2}{\partial\varphi_{\mathbf{r}}^2} \\ \mathcal{H}_t &= -t\sum_{\langle i,j\rangle}\cos(\varphi_i-\varphi_j-A_{i,j}) \end{aligned} \tag{A.1}$$

The partition function can be rewritten in a more convenient way using the Trotter approximation:

$$\begin{aligned} \mathcal{Z} &= \mathrm{Tr}\left\{(e^{-\frac{\beta}{L_\tau}(\mathcal{H}_t+\mathcal{H}_U)})^{L_\tau}\right\} \\ &= \lim_{L_\tau\to\infty}\mathrm{Tr}\left\{(e^{-\Delta\tau\mathcal{H}_U}e^{-\Delta\tau\mathcal{H}_t}+o(\Delta\tau^2))^{L_\tau}\right\} \end{aligned} \tag{A.2}$$

where $\hbar\tau$ is imaginary time and $\Delta\tau=\beta/L_\tau$ is the width of a time slice. The limit $\Delta\tau\to 0$ must be taken to recover the underlying quantum problem.

Introducing complete sets of states $|\overrightarrow{\varphi(\tau_k)}\rangle$ with periodic boundary conditions on times ($\tau_0 = 0 \equiv \tau_{L_\tau} = \beta$) the trace can be written as

$$\mathcal{Z} = \int \mathcal{D}\varphi \prod_{k=0}^{L_\tau} \langle\overrightarrow{\varphi(\tau_{k+1})}|e^{-\Delta\tau \widehat{\mathcal{H}_U e^{-\Delta\tau \mathcal{H}_t}}}|\overrightarrow{\varphi(\tau_k)}\rangle \tag{A.3}$$

Since the states $|\overrightarrow{\varphi(\tau_k)}\rangle$ are eigenstates of $\mathcal{H}_t$, the calculation is reduced to the evaluation of the matrix elements

$$\langle\overrightarrow{\varphi(\tau_{k+1})}|\widehat{e^{-\Delta\tau \mathcal{H}_U}}|\overrightarrow{\varphi(\tau_k)}\rangle. \tag{A.4}$$

the matrix elements can be furtherly simplified going back to the charge representation (or angular momentum, since n is the generator of $U(1)$ for the XY spin of a site):

$$\sum_{\overrightarrow{J^\tau}} \prod_i e^{-\frac{U\,\Delta\tau}{2}[J_i^\tau]^2} e^{\imath\, J_i^\tau\,[\varphi_i(\tau_k)-\varphi_i(\tau_{k+1})]}. \tag{A.5}$$

Using the Poisson summation formula, the sum over angular momentum configurations becomes a periodic sequence of narrow gaussians around multiples of 2π

$$\prod_i \sum_{m=-\infty}^{+\infty} \sqrt{\frac{2\pi}{U\,\Delta\tau}}\, e^{-\frac{1}{2\,\Delta\tau\,U}[\varphi_i(\tau_k)-\varphi_i(\tau_{k+1})-2\pi m]^2} \tag{A.6}$$

that is the Villain approximation to

$$\mathcal{T}_k \approx \prod_i e^{-\frac{1}{U\,\Delta\tau}\cos[\varphi_i(\tau_k)-\varphi_i(\tau_{k+1})]} \tag{A.7}$$

with dropped irrelevant prefactors.

What we get by means of this procedure is a mapping of the QPM into a *anisotropic* classical $(2+1)DXY$ model, with effective action $\mathcal{S}$

$$\begin{aligned} \mathcal{S} &= K_{sp} \sum_{\langle i,\,j\rangle,k} [1 - \cos(\varphi_{i,k} - \varphi_{j,k} - A_{i,\,j})] \\ &+ K_\tau \sum_{i,\langle k,\,k'\rangle} [1 - \cos(\varphi_{i,k} - \varphi_{i,k'})] \end{aligned} \tag{A.8}$$

$$K_{sp} = t\,\Delta\tau \qquad K_\tau = \frac{1}{U\,\Delta\tau} \tag{A.9}$$

where we used a symmetric notation for space and time lattice sites. Since critical properties are not expected to depend on the asymmetry of such model, and since for $\Delta\tau \longrightarrow 0$ we have $K_{sp} \longrightarrow 0$, $K_\tau \longrightarrow \infty$ with $K_{sp}\, K_\tau =$ const., one can fix $\Delta\tau = 1/\sqrt{tU}$. It then follows that the coupling in the space and time directions are equal $K_{sp} = K_\tau = K$. The isotropic model is the one which is used in in the Monte Carlo simulations.

MC simulations were then performed discretizing the values that the site phase can assume (typically 14400 values, i.e. $\mathrm{d}\varphi = 0.025°$). The MC elementary steps were done by means of a standard Metropolis algorithm, i.e. a new configuration is generated by a random local move and it is accepted or refused according to Boltzmann exponential weights [9].

Appendix B

Density Matrix Renormalization Group

The Density Matrix Renormalization Group (DMRG) in its first formulation given by White [26, 27] is a numerical technique for finding accurate approximations to the ground state and the low-lying excited states of strongly interacting one-dimensional quantum lattice systems, such as the Heisenberg model or Bose-Hubbard models.

The simulation of a quantum mechanical system is in general a very hard task; one of the reasons is related to the number of parameters required to represent a quantum state, which usually grows exponentially with the number of constituents of the system (for details, see Sec. B.1 and references therein). However if one is interested in the ground state properties of a one-dimensional system, the number of parameters is limited for non critical systems, or grows polynomially for a critical one [219]. This means that it is possible to simulate them by considering only a relevant smaller portion of the entire Hilbert space. This is the key idea on which all the numerical renormalization algorithms rely. Starting from some microscopic Hamiltonian in a Hilbert space of dimension d, degrees of freedom are iteratively integrated out and accounted for by modifying the original Hamiltonian. The new Hamiltonian will thus exhibit modified, as well as new couplings; renormalization group approximations typically consist in physically motivated truncations

of the set of couplings newly generated by the elimination of degrees of freedom. In this way one obtains a simplified effective Hamiltonian that should catch the essential physics of the system under study.

The key for the success of these techniques rests on scale separation: in continuous phase transitions, for example, the diverging correlation length sets a natural low-energy scale which dominates the physical properties; fluctuations on shorter length scales may be integrated out and summed up into quantitative modifications of the long-wavelength behavior [220].

This chapter will be entirely devoted to give a brief introduction of the DMRG method (for a more comprehensive exposition, see e.g. [71]). In Sec. B.1 we present the basic ideas of Wilson's numerical Renormalization Group, while in Sec. B.2 we describe the key algorithmic ideas of the DMRG. This includes an overview of the infinite-system DMRG, the finite-system DMRG and a discussion about the problem of boundary conditions. In Sec. B.3 we discuss how to measure static quantities, like local observables or correlation functions. Sec. B.4 is devoted to the extension of the DMRG method to the simulation of time dependent quantum systems. In Sec. B.5 some technical issues regarding the implementation of a DMRG program are presented. We also give simple numerical examples and provide a schematic flow chart, in order to better clarify the working principles of the DMRG algorithm.

B.1 Numerical Renormalization Group

DMRG traces his roots to Wilson's numerical Renormalization Group [220] (RG), which represents the simplest way to perform a real-space renormalization of Hamiltonians. The RG starts with a numerical representation of the system Hamiltonian in a particular basis, then iteratively adds degrees of freedom typically by increasing the size of the finite system, and numerically transforming the representation of the new Hamiltonian to a reduced basis.

Let us consider in more detail how the RG approach works in the simplest possible context, a real-space blocking approach for a one-dimensional

strongly interacting quantum lattice system, with nearest neighbor interactions. The approach is relevant for zero temperature, and is used to find the ground state and some low-lying states.

1. Isolate a portion B of the system (the so called "block") containing L sites. L is chosen to be small enough so that the block Hamiltonian $\hat{H}_B$, which acts on an m-dimensional Hilbert space, can be diagonalized exactly;

2. Form a compound block BB of length $2L$ and Hamiltonian $\hat{H}_{BB}$, consisting of two block Hamiltonians and inter-block interactions. $\hat{H}_{BB}$ has dimensions m^2.

3. Project $\hat{H}_{BB}$ onto the truncated space spanned by the m lowest-lying eigenstates: $\hat{H}_{BB} \to \hat{H}_{BB}^{\text{trunc}}$;

4. Restart from step (2) with doubled block size: $2L \to L'$, $BB \to B'$, $\hat{H}_{BB}^{\text{trunc}} \to \hat{H'}_B$. Repeat this procedure until the total system size is reached.

The key point of the whole scheme consists in the decimation procedure of the Hilbert space, which is performed by retaining the lowest-lying eigenstates of the compound block BB. This amounts to the assumption that the ground state of the entire system will essentially be composed of energetically low-lying states living on smaller subsystems (the forming blocks B_j).

Unfortunately this procedure has an evident breakdown: consider indeed the toy model of a single non-interacting particle hopping on a discrete one-dimensional lattice. For a box of size L the Hilbert space has dimension $m = L$ (the basis state $|i\rangle$ corresponds to have the particle on site i). Assume for simplicity that the block size is sufficiently large to avoid discretization. The lowest-lying states of B all have nodes at the lattice ends, so all product states of BB have nodes at the compound block center. Instead, the true ground state of BB has its maximum right there, so there is no way to properly approximate it by using a restricted number of block states.

A convenient strategy to solve this breakdown is the following: to analyze which states have to be retained for a finite-size block B, B must be embedded in some environment, that mimics the thermodynamic limit system in which the block is ultimately embedded in.

B.2 Density Matrix Renormalization Group

Instead of the exponentially fast growth Wilson's procedure depicted in the previous section, consider the following linear growth prescription [26, 27].

Assume we have a system S of length L (which is called "block") in an $m^{(S)}$-dimensional Hilbert space, described by the Hamiltonian $\hat{H}_L$. Let $\{|n_L^{(S)}\rangle\}$ be a basis in this space. An "enlarged block" Hamiltonian $\hat{H}_{L+1}$ is then constructed, by adding a site to the block Hamiltonian $\hat{H}_L$. A basis in this new space can be written in the product form: $\{|n_L^{(S)}\,\sigma^{(S)}\rangle\} \equiv \{|n_L^{(S)}\rangle \otimes |\sigma^{(S)}\rangle\}$, where $|\sigma^{(S)}\rangle$ are the d local states of the new added site.

The thermodynamic limit is now mimicked by embedding the system in an environment E of the same size, assumed to have been constructed in analogy to the system; we thus arrive at a "superblock" of length $2L+2$. The best approximation to the ground state at the thermodynamic limit is the ground state of the superblock, which is obtained by numerical diagonalization:

$$|\psi\rangle = \sum_{n^{(S)}=1}^{m^{(S)}} \sum_{\sigma^{(S)}=1}^{d} \sum_{\sigma^{(E)}=1}^{d} \sum_{n^{(E)}=1}^{m^{(E)}} \psi_{n^{(S)}\sigma^{(S)}\sigma^{(E)}n^{(e)}} |n^{(S)}\sigma^{(S)}\rangle \otimes |n^{(E)}\sigma^{(E)}\rangle \quad \text{(B.1)}$$

where $\{|n^{(S)}\sigma^{(S)}\rangle\}$ and $\{|n^{(E)}\sigma^{(E)}\rangle\}$ are the orthonormal product bases of system S and environment E respectively, with dimensions $N^{(S)} = m^{(S)} \times d$ and $N^{(E)} = m^{(E)} \times d$. A truncation procedure from $N^{(S)}$ to $m^{(S)} < N^{(S)}$ states is required; in White's DMRG the density matrix is used in order to choose the 'most important' states (the ones that must be kept).

In [26, 27] it is shown that keeping the $m^{(S)}$ most probable eigenstates of the reduced density matrix of the enlarged block with respect to the superblock gives its most accurate representation, in a $m^{(S)}$-dimensional Hilbert space. Here we just report a qualitative argument in support of this method.

Consider an isolated block B at finite temperature β; the probability to find it in an eigenstate $|\alpha\rangle$ of the block Hamiltonian is proportional to its Boltzmann weight $\exp(-\beta E_\alpha)$. The Boltzmann weight is an eigenvalue of the density matrix $\rho_B = \exp(\beta H_B)$, and an eigenstate of the Hamiltonian is also an eigenstate of the density matrix. Since lowest energy corresponds to highest probability in the Boltzmann weight, given the assumption that the block is isolated, we can choose the m most probable eigenstates to represent the block. In reality the block is not isolated, so it is much more appropriate to use the eigenstates of the density matrix with respect to the environment, rather than the eigenstates of the system's Hamiltonian, to describe the system.

B.2.1 Infinite-system DMRG

Keeping in mind the main ideas of the DMRG depicted above, we now formulate the basis structure of the so called *Infinite-system DMRG* for one-dimensional lattice systems (for a pedagogical introduction, see [221]).

1. Consider a lattice of size L, forming the system block $B^{(S)}$. $B^{(S)}$ lives on a Hilbert space of size d^L with basis states $\{|n_L^{(S)}\rangle\}$. The Hamiltonian $\hat{H}_L^{(S)}$ and the operators acting on the block are assumed to be known in this basis (at initialization L must be chosen such that $d^L \leq m^{(S)}$). Similarly form an environment block $B^{(E)}$; if the system is globally reflection-symmetric, the environment block can be taken equal to the system block.

2. Starting from $B^{(S)}$ and adding one site to it, form a tentative new system block: $B^{(S)}\bullet$, which is called the enlarged block (here $\bullet$ represents the added free site). The enlarged block lives on a Hilbert space of size $N^{(S)} = m^{(S)} \times d$, with a basis of product states $\{|n_L^{(S)}\,\sigma\rangle\} \equiv \{|n_L^{(S)}\rangle \otimes |\sigma\rangle\}$. The new Hamiltonian $\hat{H}_{L+1}^{(S\bullet)}$ can now be expressed in this basis. A new environment $B^{(E)}\bullet$ is built from $B^{(E)}$ in same way.

3. Build the superblock of length $2L+2$ from the two enlarged blocks $B^{(S)}\bullet$ and $B^{(E)}\bullet$. To perform calculations with open boundary condi-

tions they are linked through the two added sites: $B^{(S)} \bullet \bullet B^{(E)}$. The new Hilbert space is of size $N^{(S)} \times N^{(E)} = (m^{(S)} \times d) \times (d \times m^{(E)})$, and the $\hat{H}_{2L+2}$ Hamiltonian can be explicitly constructed.
Notice that, in the case of a globally reflection-symmetric system, we have $B^{(S)} = B^{(E)}$ and thus the size of the superblock Hilbert space is: $N^2 = (m \times d)^2$ (where $m = m^{(S)} = m^{(E)}$).

4. Diagonalize $\hat{H}_{2L+2}$ and find its ground state $|\psi\rangle$.

5. Form the reduced density matrix of the enlarged system block: $\rho^{(S)} = \mathrm{Tr}_{(E)}|\psi\rangle\langle\psi|$, and determine its eigenbasis $|w_\alpha\rangle$ ordered by descending eigenvalues w_α. Form a new approximate basis for the enlarged block $B^{(S)}\bullet$ by taking the $m^{(S)}$ eigenstates with the largest weights. Their matrix elements $\langle n_L^{(S)}\sigma|m_{L+1}^{(S)}\rangle$ taken as column vectors form a $N^{(S)} \times m^{(S)}$ rectangular matrix $\hat{O}^{(S)}$. Proceed in the same way for the environment.

6. Perform the reduced basis transformation: $\hat{H}_{L+1}^{\mathrm{tr}} = \hat{O}^{(S)\dagger}\hat{H}_{L+1}^{(S\bullet)}\hat{O}^{(S)}$ onto the new $m^{(S)}$-state basis and take $\hat{H}_{L+1}^{\mathrm{tr}} \to \hat{H}_{L+1}^{(S)}$ for the system. Do the same for the environment E and restart with step 2 until the desired final length is reached. Operators representation also have to be updated.

7. Calculate desired ground state properties from $|\psi\rangle$.

B.2.2 Finite-system DMRG

For many problems, infinite-system DMRG does not yield satisfactory answers: the idea of simulating the final system size cannot be implemented well by a small environment block in the early DMRG steps. For example, the strong physical effects of impurities or randomness in the Hamiltonian cannot be accounted for properly by infinite-system DMRG, as the total Hamiltonian is not yet known at intermediate steps. In systems with strong magnetic fields, or close to a first order transition one may be trapped in a metastable state favoured for small sizes (e.g. by edge effects).

Finite-system DMRG manages to eliminate such effects to a very large degree, and to reduce the error almost to the truncation error. The idea of the finite-system DMRG algorithm is to stop the infinite-system algorithm at some preselected superblock length $L_{\max}$, which is subsequently kept fixed. In subsequent DMRG steps one applies the steps of infinite-system DMRG, but instead of simultaneous growth of both blocks, growth of one block is accompanied by shrinkage of the other. Reduced basis transformations are carried out only for the growing block.

Let the system block $B^{(S)}$ grow at the expense of the environment block $B^{(E)}$; to describe it, environment blocks of all sizes and operators acting on this block, expressed in the basis of that block, must have been previously stored (during the infinite-system stage or previous applications of finite-system DMRG). When the environment block reaches some minimum size and becomes exact, growth direction is reversed. The system block now shrinks, while the environment grows. A complete growth and shrinkage for both blocks is called a *sweep*.

B.2.3 Boundary conditions

From a physical point of view periodic boundary conditions are normally high preferable to the open boundary conditions, as surface effects are eliminated and finite-size extrapolation works for much smaller system sizes. However it has been observed that in the DMRG algorithm, ground state energies for a given m are much less precise in the case of periodic boundary conditions than for open boundary conditions This is reflected in the spectrum of the reduced density matrix, that decays much more slowly [222].

To implement periodic boundary conditions it is most convenient to use the superblock configuration $B^{(S)} \bullet B^{(E)} \bullet$. This configuration is preferred over $B^{(S)} \bullet \bullet B^{(E)}$ because it does not have the two big blocks as neighbors.

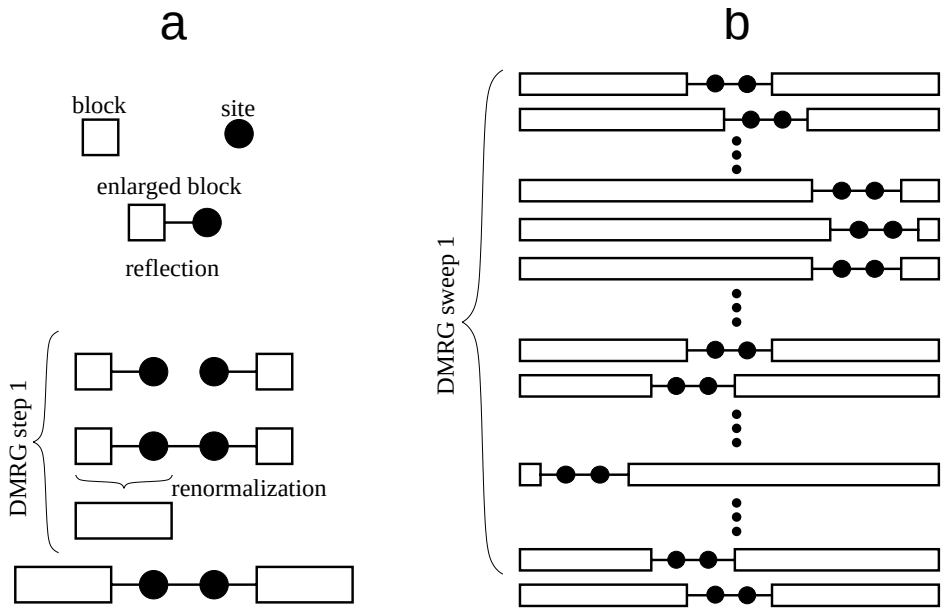

Figure B.1: Schematic procedure for the DMRG algorithm. On the left part (a) one iteration of the infinite-system DMRG algorithm is shown: starting from the system block $B^{(S)}$ and adding one free site to it, the enlarged block $B^{(S)}\bullet$ is formed. Here for simplicity we assume that the system is reflection-symmetric, thus the environment block is taken equal to the block. Then, after having created the superblock $B^{(S)}\bullet\bullet B^{(E)}$, a renormalization procedure is applied in order to get the new block for the next iteration.
On the right part (b) the scheme of a complete finite-system DMRG sweep is depicted.

B.3 Measurement of observables

Properties of the L-site system can be obtained from the wave functions $|\psi\rangle$ of any of the superblock configurations, although the symmetric configuration (with free sites at the center of the chain) usually gives the most accurate results. The procedure is to use the wave function $|\psi\rangle$ resulting from the diagonalization of the superblock for the L-site system to evaluate expectation values of the form $\langle\psi|\hat{A}|\psi\rangle$.

Let us start by considering measures of local observables $\hat{A}_j$, living on

one single site j. If one is performing the finite-system DMRG algorithm, it is possible to evaluate the measurement of $\hat{A}_j$ at the particular step inside a sweep in which i is one of the two free sites. The measure then is a simple average:

$$\langle\psi|A_j|\psi\rangle = \sum_{n^{(S)}\,\sigma^{(S)}\,\sigma^{(E)}\,n^{(E)}\,\tau^{(S)}} \psi^*_{n^{(S)}\sigma^{(S)}\sigma^{(E)}n^{(E)}}\,[A_j]_{\sigma^{(S)}\tau^{(S)}}\,\psi_{n^{(S)}\tau^{(S)}\sigma^{(E)}n^{(E)}}$$

Instead, if one is performing the infinite-system DMRG, there are two possibilities: either i is one of the two central free sites or not. In the first case the measurement proceeds as before, in the last case the operator matrix for the components of A in the truncated DMRG basis of the blocks is required. At each DMRG iteration the operator $\hat{A}_j$ must be updated in the new basis using the $\hat{O}$ matrix: $\hat{A}_j \to \hat{O}^\dagger \hat{A}_j \hat{O}$ (see step (6) of the infinite-system DMRG).

For non local observables, like a correlation function $\hat{A}_j\hat{A}_k$, the evaluation depends on whether j and k are on the same block or not. During the finite-system DMRG it is always possible to have them on different blocks (just wait for an appropriate step during the sweep). In this case the average can be computed as above. For example, if $j \in S$ and k is the right free site, one has:

$$\langle\psi|A_jA_k|\psi\rangle =$$

$$= \sum_{n^{(S)}\,\sigma^{(S)}\,\sigma^{(E)}\,n^{(E)}\,p^{(S)}\,\tau^{(E)}} \psi^*_{n^{(S)}\sigma^{(S)}\sigma^{(E)}n^{(E)}}\,[A_j]_{n^{(S)}p^{(S)}}\,[A_k]_{\sigma^{(E)}\tau^{(E)}}\,\psi_{p^{(S)}\sigma^{(S)}\tau^{(E)}n^{(E)}}$$

In the infinite-system DMRG instead it is also possible to have j and k on the same block. Then one needs to have kept track of the matrix $\hat{A}_j\hat{A}_k$ in the basis of the block throughout the calculation, then evaluates it as a local operator on the block:

$$\langle\psi|A_jA_k|\psi\rangle = \sum_{n^{(S)}\,\sigma^{(S)}\,\sigma^{(E)}\,n^{(E)}\,p^{(S)}} \psi^*_{n^{(S)}\sigma^{(S)}\sigma^{(E)}n^{(E)}}\,[A_jA_k]_{n^{(S)}p^{(S)}}\,\psi_{p^{(S)}\sigma^{(S)}\sigma^{(E)}n^{(E)}}$$

Usually the convergence of measurements is slower than that of energy, in the sense that in order to have reliable measurement results many finite-system DMRG sweeps are required (nonetheless, typically a number ≤ 5

is sufficient); instead the energy generally converges just after one or two sweeps.

B.4 Time dependent DMRG

In this section we briefly describe an extension to the DMRG method which incorporates real time evolution into the algorithm. Various different time-dependent simulation methods based on the DMRG have been recently proposed [223, 224, 225, 219], but here we restrict our attention to the algorithm introduced by White and Feiguin [225].

The aim of the Time-dependent DMRG method (T-DMRG) is to simulate the evolution of the ground state of a nearest-neighbor one dimensional system described by certain Hamiltonian $\hat{H}_0$, following the dynamics of a different Hamiltonian $\hat{H}$. Typically the algorithm starts with a Finite-system DMRG, in order to find an accurate approximation of the ground state $|\psi_0\rangle$ of $\hat{H}_0$. Then, the T-DMRG is applied. The crucial idea of this method is to use a Suzuki-Trotter decomposition for the time evolution operator $\hat{U} = e^{-i\hat{H}t}$. The second order expansion in time dt is given by the formula:

$$e^{-i\hat{H}t} = \left(e^{-i\hat{F}\frac{dt}{2}}\, e^{-i\hat{G}dt}\, e^{-i\hat{F}\frac{dt}{2}}\right)^n + O(dt^3), \tag{B.2}$$

where $n = t/dt$ gives the discretization of time t in small intervals dt. The Hamiltonian $\hat{H}$ has been divided in two parts: $\hat{F} = \sum_{i\,\mathrm{even}} \hat{H}_{i,i+1}$ contains the terms corresponding to even bonds, while $\hat{G} = \sum_{i\,\mathrm{odd}} \hat{H}_{i,i+1}$ contains only odd bonds ($\hat{H}_{i,i+1}$ is the interaction Hamiltonian between sites i and $i+1$, plus the local term on i). Since the terms inside $\hat{F}$ and $\hat{G}$ commute, Eq. (B.2) can be rewritten as:

$$e^{-i\hat{H}t} = \left(\prod_{i\,\mathrm{even}} e^{-i\hat{H}_{i,i+1}\frac{dt}{2}} \prod_{i\,\mathrm{odd}} e^{-i\hat{H}_{i,i+1}dt} \prod_{i\,\mathrm{even}} e^{-i\hat{H}_{i,i+1}\frac{dt}{2}}\right)^n + O(dt^3) \tag{B.3}$$

without any further approximation.

The formula in Eq. (B.3) is very useful, since it expresses the evolution operator $\hat{U}$ as a product in terms of matrices which can be applied directly and efficiently to the DMRG wavefunction, Eq. (B.1). Indeed each of the

matrices $\hat{H}_{i,i+1}$ acts on the two sites i, $i+1$, which correspond to the two free sites on each finite-system DMRG step j. If $\hat{H}_{i,i+1}$ included terms for other sites, it would have been necessary to adapt it onto a basis of the block.

The T-DMRG algorithm proceeds as follows: a slightly modified finite-system DMRG half-sweep is performed in order to apply each of the operators $e^{-i\hat{F}\frac{dt}{2}}$ and $e^{-i\hat{G}dt}$. We need a step-to-step wavefunction transformation, such that, at each DMRG iteration, the representation of the system wavefunction $|\psi\rangle$ passes from the basis for the configuration with block $B^{(S)}$ of size L to the basis in which $B^{(S)}$ is of size $L+1$. Assuming this transformation is implemented, the real-time algorithm introduces only a very minor modification: at each step j, instead of diagonalizing the superblock Hamiltonian (step (4) in Subsec. B.2.1), one evolves the transformed wavefunction by applying and operator of the form $e^{-i\hat{H}_{i,i+1}dt}$.

Thus, to evolve the system of each Trotter interval dt, we need 3/2 finite-system DMRG sweeps:in the first half we apply $e^{-i\hat{F}\frac{dt}{2}}$, in the second $e^{-i\hat{G}dt}$ and in the third $e^{-i\hat{F}\frac{dt}{2}}$.

Notice that a T-DMRG step is typically much faster that a finite/infinite one, since the superblock diagonalization is no longer required. Measurement of observables proceeds exactly in the same way as in the finite-system algorithm.

To further reduce the Trotter error it is also possible to expand the evolution operator $\hat{U}$ to the fourth order in dt [226]:

$$e^{-i\hat{H}t} = \prod_{i=1}^{5} \left(e^{-ip_i\,\hat{F}\,\frac{dt}{2}}\, e^{-ip_i\,\hat{G}\,dt}\, e^{-i\,p_i\,\hat{F}\,\frac{dt}{2}} \right)^n + O(dt^5), \tag{B.4}$$

where all $p_i = 1/(4-4^{1/3})$, except $p_3 = 1-4p_1 < 0$, corresponding to evolution backward in time. The price we have to pay is that the implementation of expansion in Eq. (B.4) requires $5\cdot\frac{3}{2}$ sweeps; this means a computational time 5 times greater than the one needed for Eq. (B.2).

B.5 Technical issues and examples

In this section we explain some technicalities regarding the implementation of DMRG. We wrote the program code in FORTRAN 90. An important feature of this programming language is the possibility to use dynamical allocation of memory, essential in every DMRG program, in which matrices dimensions change at each iteration.

The most time consuming part of a typical DMRG step is the diagonalization of the superblock Hamiltonian $\hat{H}_{SB}$, a $(m\,d)^2 \times (m\,d)^2$ matrix (hereafter we will assume $m^{(S)} \sim m^{(E)} \sim m$). Since we are only interested in the ground state properties (at most in low-energy eigenstates), we used the Davidson diagonalization method. This is much more faster than usual diagonalization algorithms, since it gives only a small number ($\lesssim 10$) of eigenstates close to a previously chosen target energy; moreover it is optimized for large sparse matrices, that is the case of typical superblock Hamiltonians.

Another great advantage with respect to standard diagonalization techniques, is that the full superblock Hamiltonian $\hat{H}_{SB}$ is never written. We only require to express the effect of it on a generic state $|\psi\rangle$ which lives in a $(md)^2$ dimensional Hilbert space. Since $\hat{H}_{SB}$ can be written as

$$\hat{H} = \sum_p \hat{A}^p \otimes \hat{B}^p \,, \tag{B.5}$$

where $\hat{A}^p$ and $\hat{B}^p$ act respectively on the left $B^{(S)} \bullet$ and on the right enlarged block $\bullet\, B^{(E)}$. Thus we just need to implement the matrix multiplication:

$$\psi^{\rm out}_{ij} = \sum_{p,i'j'} A^p_{ii'}\, B^p_{jj'}\, \psi^{\rm in}_{i'j'},$$

where i, i' and j, j' are indexes for the left and the right enlarged blocks. In this way it is possible to save a great amount of memory and number of operations, since the dimensions of $\hat{A}^p$ and $\hat{B}^p$ are $(m\,d) \times (m\,d)$, and not $(m\,d)^2 \times (m\,d)^2$. As an example, the typical m value for simulating the evolution of a $L_{\rm max} = 50$ spin 1/2 chain ($d = 2$) is $m \sim 50$. This means that, in order to store all the $\sim 10^8$ complex numbers of $\hat{H}_{SB}$ in double precision,

$\sim$ 1.6 Gigabytes of memory is needed. Instead, each of the two matrices $\hat{A}$ and $\hat{B}$ requires less than 200 kilobytes of memory.

The step-to-step wavefunction transformation required for the T-DMRG algorithm, which has been described in the previous paragraph, can also be used in the finite-system DMRG to speed up the superblock diagonalization [227]. Indeed the Davidson diagonalization method is an iterative algorithm which starts from a generic wave function, and then recursively modifies it, until the eigenstate closest to the target eigenvalue is reached (up to some tolerance value, fixed from the user). If a very good initial guess is available for the Davidson, the number of steps required to converge to the solution can be substantially reduced. During the finite-system DMRG the physical system is no longer changing, so an ideal initial guess could be the final wave function from the previous DMRG step, after it has been written in the new basis for the current step. This procedure can reduce the computational time even by an order of magnitude. It is possible to speed up the diagonalization even in the infinite-system algorithm, but here the question is complicated by the fact that the physical system changes from step to step (for information, see [226] and references therein).

The DMRG requires to store a great number of operators: the block Hamiltonian, the updating matrices $\hat{O}$, and if necessary the observables for each possible block length (see the procedure for the finite-system algorithm in Subsec. B.2.2). The best way to handle all these operators is to group each of them in a register in which one index represents the length of the block. Since typically these operators are large sparse matrices, a huge amount of memory can be saved by storing only the non zero elements; in particular what we did is to introduce for each matrix a list of positions (row and column) of all the non zero elements, and an array containing such values. The list procedure allowed us to save up to a factor 100 of memory, thus to simulate systems of considerably bigger size. The most memory consuming problem we have studied is the spin 1 Bose-Hubbard model with $d = 20\,,\ m = 120\,,\ L = 112$ (or $d = 3\,,\ m = 350\,,\ L = 80$), which requires

$\sim$ 1.5 Gigabytes of RAM.

If the system is globally reflection-symmetric, it is possible to take the environment block equal to the system block. The only thing to do is a relabelling of sites, as shown in Fig. B.2.

If other symmetries hold (as conservation of total particle number, or an-

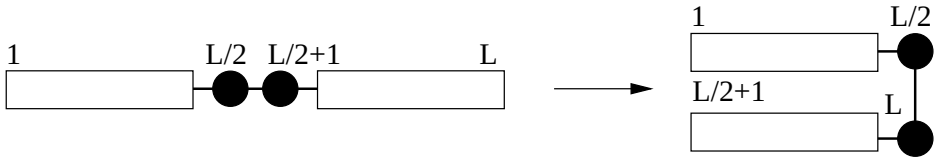

Figure B.2: Alternative labelling of sites to be used in the environment reflection procedure (in case of globally reflection-symmetric systems).

gular momentum) we can take advantage of these properties, such to considerably reduce the CPU time for simulation. The key idea is to write the Hamiltonian in a block diagonal form, and then diagonalize each of them; if we are interested in the ground state, we compare the lowest energies inside each block in order to find the global lowest eigenstate. There are situations in which we are interested in the ground state with certain quantum numbers (for example in the Bose-Hubbard model we need to fix the number of particles); in these cases we just diagonalize the block Hamiltonian corresponding to the wanted quantum numbers. In order to write the Hamiltonian in block form we need to label the eigenstates of the reduced density matrix according to the various quantum numbers. We implemented the DMRG truncation in such a way to retain whole blocks of eigenstates that have the same weight and quantum numbers, in order to avoid an unwanted artificial symmetry breaking.

Most of out DMRG calculations have been performed onto an IBM eServer Blade Center JS20 with 7 blades [228]. Each blade has two 1.6 GHz PowerPC 970 processors and 2.4 Gb DDR EEC RAM memory.

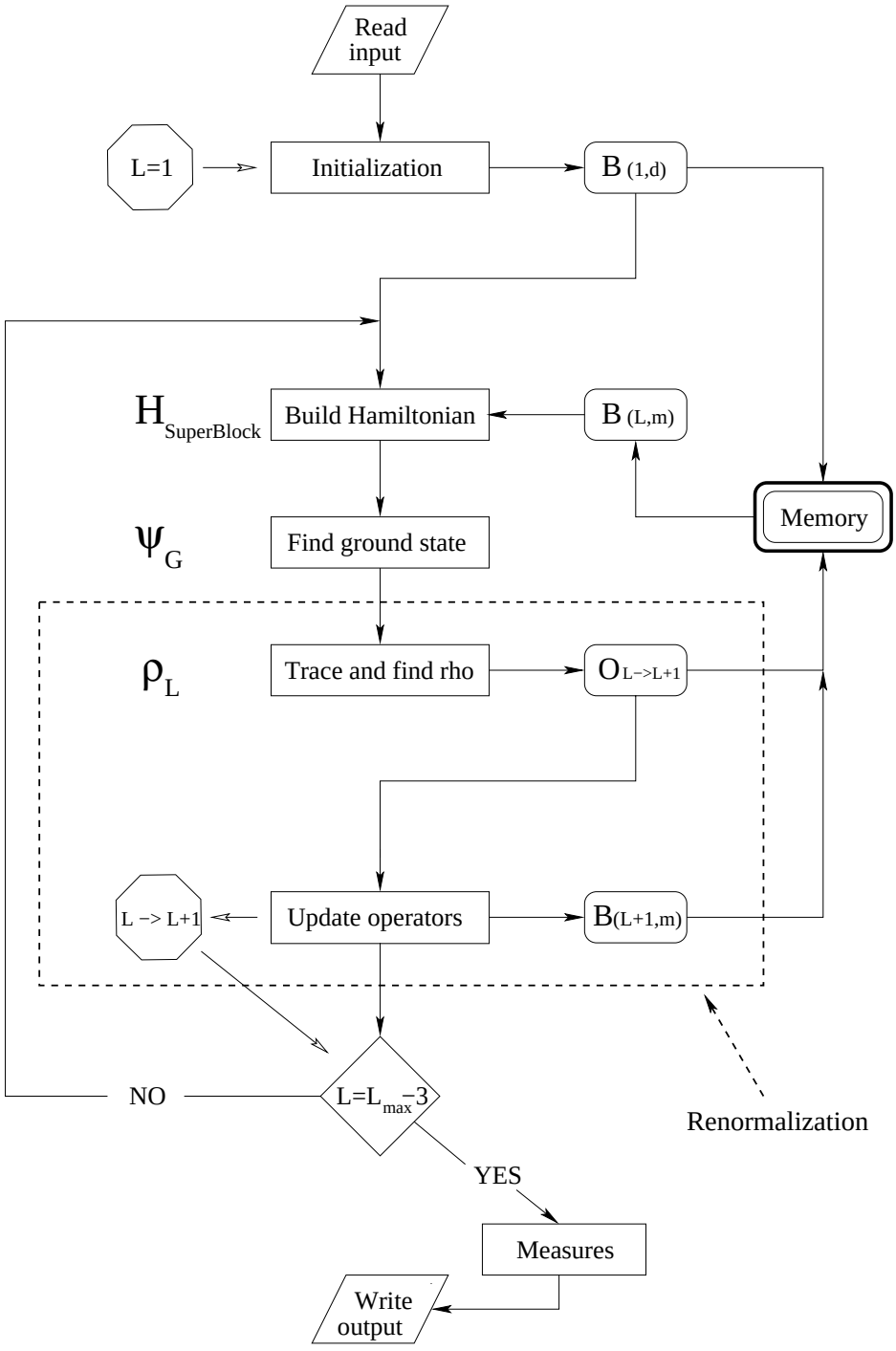

Figure B.3: Basic scheme of the infinite/finite system DMRG algorithm. Here we have supposed, for simplicity, that the system is globally reflection symmetric (thus the environment block is taken equal to the system block).

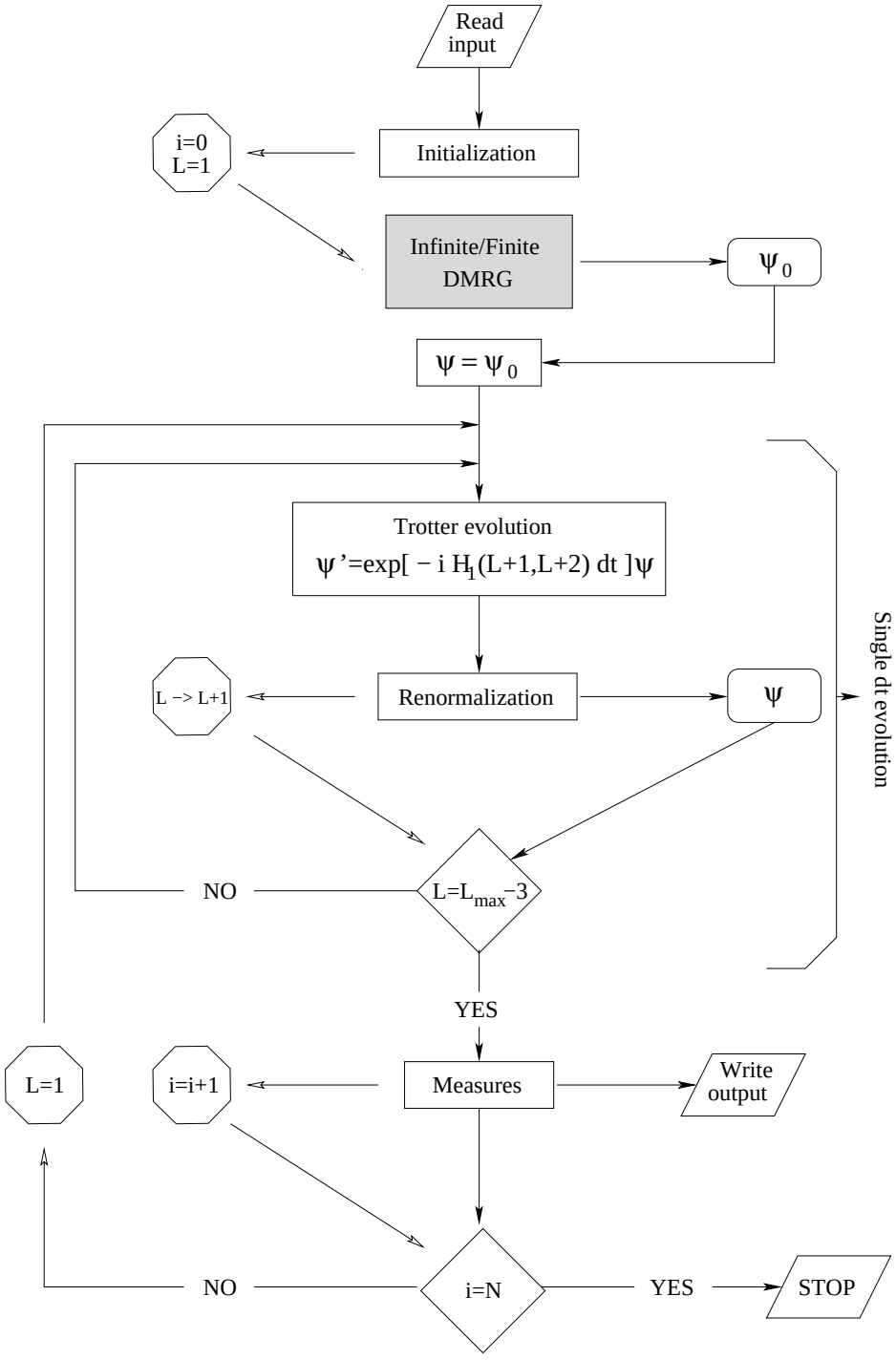

Figure B.4: Basic scheme of the time-dependent DMRG algorithm.

Appendix C

Momentum distributions in Open Boundary chains

The aim of this short Chapter is to highlight the proper definition of the particle's momentum distributions in the open boundary chain we are working on.

Single particle's eigenstates have definite absolute value of momentum and fixed relative phase between counterpropagating waves. Thus, exploiting them as a basis for the expansion of operators, the result will be different from a standard Fourier transform. That would be the case for periodic boundary conditions.

C.0.1 Solving the single particle problem

The free particle model, i.e. atoms hopping on a lattice of L sites with o.b.c., consists on the following Hamiltonian:

$$\mathcal{H}_L = -t_s \sum_{i=1}^{L-1} \left(s_i^\dagger s_{i+1} + h.c. \right) \tag{C.1}$$

where $s = b, f$ according to the species considered. It is totally irrelevant for our purposes now distinguish these two cases. The single particle wavefunction can be written as $|\phi\rangle = \sum_{j=1}^{L} \phi_j s_j^\dagger |0\rangle$ and should satisfy the recursive

relations given by the secular problem

$$\begin{aligned} -t\ (\phi_{j-1} + \phi_{j+1}) &= E\ \phi_j \\ \phi_0 &= 0 \\ \phi_{L+1} &= 0 \end{aligned} \tag{C.2}$$

Last two equations correspond to the open boundary request.

A trial solution can be written as $\phi_j = a_+ e^{\mathbf{i}kj} + a_- e^{-\mathbf{i}kj}$, which turns out to give the simplified equations

$$\begin{aligned} -2t\ \cos k &= E \\ a_+ + a_- &= 0 \\ 2\,\mathbf{i}\,a\ \sin k(L+1) &= 0 \end{aligned} \tag{C.3}$$

which results in the vinculum $k = n\frac{\pi}{L+1}$ with n non-null integer.

So, the one body eigenstates on the o.b. chain have energies $E_k = -2\,t\ \cos k$ and wave functions

$$|\widetilde{\phi}_n\rangle = \frac{1}{\sqrt{(L+1)/2}} \sum_{j=1}^{L} \sin\left(n\frac{\pi}{L+1}j\right) s_j^\dagger |0\rangle \tag{C.4}$$

The normalization is fixed by $\langle\widetilde{\phi}_n|\widetilde{\phi}_n\rangle = 1$ and is equal for every n, since $\sum_{j=1}^{L}\left(\sin(n\frac{\pi}{L+1}j)\right)^2 = \frac{L+1}{2} \quad \forall n$. Such a normalization will give the correct number of particles also in the transformed basis.

C.0.2 Defining momentum distributions properly

Exploiting the results of the previous section, one can define

$$\widetilde{s_n}^\dagger = \frac{1}{\sqrt{(L+1)/2}} \sum_{j=1}^{L} \sin\left(n\frac{\pi}{L+1}j\right) s_j^\dagger \tag{C.5}$$

The definition of the momentum distribution follows straightforward:

$$\widetilde{n}_s(k\frac{\pi}{L+1}) \;=\; \frac{2}{L+1} \sum_{i,j=1}^{L} \sin\left(k\frac{\pi}{L+1}i\right) \sin\left(k\frac{\pi}{L+1}j\right) \langle s_i^\dagger\ s_j\rangle$$

We stress that the momenta spectrum in an OBC tends correctly to the usual free particle's one in the thermodynamic limit. Nonetheless, some feature introduced by boundary conditions can not be neglected, e.g. the quasi-condensation of superfluid bosons happens at a finite momentum $\pi/(L+1)$.

Appendix D

Related publications

1. M. Rizzi, D. Rossini, G. De Chiara, S. Montangero, and R. Fazio, *Phase diagram of spin-1 bosons on one-dimensional lattices*, Phys. Rev. Lett. **95**, 240404 (2005).

2. M. Rizzi, V. Cataudella, and R. Fazio, *Phase Diagram of the Bose-Hubbard Model with T_3 symmetry*, Phys. Rev. B **73**, 144511 (2006).

3. M. Rizzi, V. Cataudella, and R. Fazio, *4e-condensation in a fully frustrated Josephson junction diamond chain*, Phys. Rev. B **73**, 100502 (2006).

4. G. De Chiara, M. Rizzi, D. Rossini, and S. Montangero, *Density Matrix Renormalization Group for Dummies*, cond-mat/0603842, accepted by Journal of Computational and Theoretical Nanoscience.

5. D. Rossini, M. Rizzi, G. De Chiara, S. Montangero, and R. Fazio, *Anti-ferromagnetic spinor BECs in optical lattices*, J. Phys. B: At. Mol. Opt. Phys. **39**, S163-S175 (2006) Proceedings of the Third International Workshop "Theory of Quantum Gases and Quantum Coherence", Cortona (Italy) 2005.

6. G. Xianlong, M. Rizzi, M.Polini, R. Fazio, M.P. Tosi, V.L. Campo Jr, K. Capelle,
Luther-Emery Phase and Atomic-Density Waves in Trapped Fermi Gas,
Phys. Rev. Lett. **98**, 030404 (2007).

7. S.H. Abedinpour, M.R. Bakhtiari, G. Xianlong, M. Polini, M. Rizzi, and M.P. Tosi,
Phase Behaviors of Strongly Correlated Fermi Gases in One-Dimensional Confinements,
Las. Phys. **17**-2, 162-168 (2007).

8. M. Rizzi, and S. Montangero,
Quantum Entanglement Renormalization Simulator,
arXiv:0706.0868v1 [quant-ph].

9. M. Rizzi, and A. Imambekov,
Pairing of 1D Bose-Fermi mixtures with unequal masses,
arXiv:0706.4434v1 [cond-mat.str-el].

10. M. Rizzi, M.R. Bakhtiari, M. Polini, R. Fazio, M.P. Tosi,
LOFF state of a Polarized Fermionic Gas in 1D Optical Lattices,
in preparation.

Bibliography

[1] R. Fazio and H. van der Zant, Phys. Rep. **355**, 235 (2001).

[2] J. E. Mooij and G. Schön, Phys. B **152**, 1 (1988).

[3] H. A. Cerdeira and S. R. Shenoy, Phys. B **222**, 253 (1996).

[4] D. J. Resnick, J. C. Garland, J. T. Boyd, S. Shoemaker, and R. S. Newrock, Phys. Rev. Lett. **47**, 1542 (1981).

[5] C. L. P. Martinoli, Ph. Lerch and H. Beck, Jap. Jour. Appl. Phys. **26**, 1999 (1987), proc. 18th Int. Conf. Low Temperature Physics, Kyoto, 1987.

[6] V. Berezinski, Zh. Eksp. Teor. Fiz. **59**, 907 (1970).

[7] J. M. Kosterlitz and D. J. Thouless, J. Phys. C **6**, 1181 (1973).

[8] J. Vidal, R. Mosseri, and B. Douçot, Phys. Rev. Lett. **81**, 5888 (1998).

[9] D. Landau and K. Binder, *A Guide to Monte Carlo Simulations in Statistical Physics* (Cambridge University Press, New York, NY, USA, 2005).

[10] M. H. Anderson, J. R. Ensher, M. R. Matthews, C. E. Wieman, and E. A. Cornell, Science **269**, 198 (1995).

[11] K. B. Davis, M. O. Mewes, M. R. Andrews, N. J. van Druten, D. S. Durfee, D. M. Kurn, and W. Ketterle, Phys. Rev. Lett. **75**, 3969 (1995).

[12] A. Minguzzi, S. Succi, F. Toschi, M. P. Tosi, and P. Vignolo, Phys. Rep. **395**, 223 (2004).

[13] D. Jaksch and P. Zoller, Ann. Phys. **315**, 52 (2005).

[14] D. M. Stamper-Kurn and W. Ketterle, in *Coherent atomic matter waves, Les Houches Summer School Session LXXII*, edited by R. Kaiser, C. Westbrook, and F. David (2001), pp. 137–+, cond-mat/0005001.

[15] D. Jaksch, C. Bruder, J. I. Cirac, C. W. Gardiner, and P. Zoller, Phys. Rev. Lett. **81**, 3108 (1998).

[16] M. Greiner, I. Bloch, O. Mandel, T. W. Hänsch, and T. Esslinger, Phys. Rev. Lett. **87**, 160405 (2001).

[17] M. Greiner, O. Mandel, T. Esslinger, T. W. Hänsch, and I. Bloch, Nature **415**, 39 (2002).

[18] C. Orzel, A. K. Tuchman, M. L. Fenselau, M. Yasuda, and M. A. Kasevich, Science **291**, 2386 (2001).

[19] J. R. Anglin and W. Ketterle, Nature **416**, 211 (2002).

[20] B. Paredes, A. Widera, V. Murg, O. Mandel, S. Fölling, I. Cirac, G. V. Shlyapnikov, T. W. Hänsch, and I. Bloch, Nature **429**, 277 (2004).

[21] T. Kinoshita, T. Wenger, and D. S. Weiss, Science **305**, 1125 (2004).

[22] J. I. Cirac and P. Zoller, Science **301**, 176 (2003).

[23] I. Bloch, Physics World **17**, 25 (2004).

[24] W. Hofstetter, Philosophical Magazine **86**, 1891 (2006).

[25] M. Lewenstein, A. Sanpera, V. Ahufinger, B. Damski, A. S. De, and U. Sen, cond-mat/0606771 (2006), accepted for Advances in Physics.

[26] S. R. White, Phys. Rev. Lett. **69**, 2863 (1992).

[27] S. R. White, Phys. Rev. B **48**, 10345 (1993).

[28] T. Stoferle, H. Moritz, K. Gunter, M. Kohl, and T. Esslinger, Phys. Rev. Lett. **96**, 030401 (2006).

[29] H. Moritz, T. Stoferle, K. Gunter, M. Kohl, and T. Esslinger, Phys. Rev. Lett. **94**, 210401 (2005).

[30] T. Giamarchi, *Quantum Physics in One Dimension* (Clarendon Press, Oxford UK, 2004).

[31] A. G. Truscott, K. E. Strecker, W. I. McAlexander, G. B. Partridge, and R. G. Hulet, Science **291**, 2570 (2001).

[32] Z. Hadzibabic, S. Gupta, C. A. Stan, C. H. Schunck, M. W. Zwierlein, K. Dieckmann, and W. Ketterle, Phys. Rev. Lett. **91**, 160401 (2003).

[33] G. Roati, F. Riboli, G. Modugno, and M. Inguscio, Phys. Rev. Lett. **89**, 150403 (2002).

[34] C. Silber, S. Gunther, C. Marzok, B. Deh, P. W. Courteille, and C. Zimmermann, Phys. Rev. Lett. **95**, 170408 (2005).

[35] D. Jaksch, H.-J. Briegel, J. I. Cirac, C. W. Gardiner, and P. Zoller, Phys. Rev. Lett. **82**, 1975 (1999).

[36] M. P. A. Fisher, P. B. Weichman, G. Grinstein, and D. S. Fisher, Phys. Rev. B **40**, 546 (1989).

[37] S. L. Sondhi, S. M. Girvin, J. P. Carini, and D. Shahar, Rev. Mod. Phys. **69**, 315 (1997).

[38] R. F. Voss and R. A. Webb, Phys. Rev. B **25**, 3446 (1982).

[39] R. A. Webb, R. F. Voss, G. Grinstein, and P. M. Horn, Phys. Rev. Lett. **51**, 690 (1983).

[40] J. E. Mooij, B. J. van Wees, L. J. Geerligs, M. Peters, R. Fazio, and G. Schön, Phys. Rev. Lett. **65**, 645 (1990).

[41] B. P. Anderson and M. A. Kasevich, Science **282**, 1686 (1998).

[42] F. S. Cataliotti, S. Burger, C. Fort, P. Maddaloni, F. Minardi, A. Trombettoni, A. Smerzi, and M. Inguscio, Science **293**, 843 (2001).

[43] S. Burger, F. S. Cataliotti, C. Fort, F. Minardi, M. Inguscio, M. L. Chiofalo, and M. P. Tosi, Phys. Rev. Lett. **86**, 4447 (2001).

[44] O. Morsch, J. H. Müller, M. Cristiani, D. Ciampini, and E. Arimondo, Phys. Rev. Lett. **87**, 140402 (2001).

[45] A. Albus, F. Illuminati, and J. Eisert, Phys. Rev. A **68**, 023606 (2003).

[46] T. Stoferle, H. Moritz, C. Schori, M. Kohl, and T. Esslinger, Phys. Rev. Lett. **92**, 130403 (2004).

[47] K. M. O'Hara, S. L. Hemmer, M. E. Gehm, S. R. Granade, and J. E. Thomas, Science **298**, 2179 (2002).

[48] R. Roth and K. Burnett, Phys. Rev. A **67**, 031602 (2003).

[49] E. Altman, E. Demler, and M. D. Lukin, Phys. Rev. A **70**, 013603 (2004).

[50] S. Fölling, F. Gerbier, A. Widera, O. Mandel, T. Gericke, and I. Bloch, Nature **434**, 481 (2005).

[51] I. B. Spielman, W. D. Phillips, and J. V. Porto, Phys. Rev. Lett. **98**, 080404 (2007).

[52] M. Greiner, C. A. Regal, J. T. Stewart, and D. S. Jin, Phys. Rev. Lett. **94**, 110401 (2005).

[53] T. Rom, T. Best, D. van Oosten, U. Schneider, S. Fölling, B. Paredes, and I. Bloch, Nature **444**, 733 (2006).

[54] J. Villain, J. Phys. C **10**, 1717 (1977).

[55] W. Y. Shih and D. Stroud, Phys. Rev. B **30**, 6774 (1984).

[56] D. H. Lee, J. D. Joannopoulos, J. W. Negele, and D. P. Landau, Phys. Rev. Lett. **52**, 433 (1984).

[57] H. Kawamura, J. Phys. Soc. Jap. **53**, 2452 (1984).

[58] M. Y. Choi and S. Doniach, Phys. Rev. B **31**, 4516 (1985).

[59] T. C. Halsey, Phys. Rev. B **31**, 5728 (1985).

[60] S. E. Korshunov, J. Phys. C **19**, 5927 (1986).

[61] D. Jaksch and P. Zoller, New J. Phys. **5**, 56 (2003).

[62] A. S. Sorensen, E. Demler, and M. D. Lukin, Phys. Rev. Lett. **94**, 086803 (2005).

[63] M. Polini, R. Fazio, A. H. MacDonald, and M. P. Tosi, Phys. Rev. Lett. **95**, 010401 (2005).

[64] K. Osterloh, M. Baig, L. Santos, P. Zoller, and M. Lewenstein, Phys. Rev. Lett. **95**, 010403 (2005).

[65] B. Douçot and J. Vidal, Phys. Rev. Lett. **88**, 227005 (2002).

[66] C. Bruder, R. Fazio, and G. Schön, Phys. Rev. B **47**, 342 (1993).

[67] D. M. Stamper-Kurn, M. R. Andrews, A. P. Chikkatur, S. Inouye, H.-J. Miesner, J. Stenger, and W. Ketterle, Phys. Rev. Lett. **80**, 2027 (1998).

[68] M. Olshanii, Phys. Rev. Lett. **81**, 938 (1998).

[69] E. H. Lieb and F. Y. Wu, Phys. Rev. Lett. **20**, 1445 (1968).

[70] H. Shiba, Phys. Rev. B **6**, 930 (1972).

[71] U. Schollwock, Reviews of Modern Physics **77**, 259 (2005).

[72] J. V. L. Campo and K. Capelle, Phys. Rev. A **72**, 061602 (2005).

[73] G. Xianlong, M. Polini, M. P. Tosi, J. Vivaldo L. Campo, K. Capelle, and M. Rigol, Phys. Rev. B **73**, 165120 (2006).

[74] N. A. Lima, M. F. Silva, L. N. Oliveira, and K. Capelle, Phys. Rev. Lett. **90**, 146402 (2003).

[75] R. J. Magyar and K. Burke, Phys. Rev. A **70**, 032508 (2004).

[76] Y. E. Kim and A. L. Zubarev, Phys. Rev. A **70**, 033612 (2004).

[77] M. F. Silva, N. A. Lima, A. L. Malvezzi, and K. Capelle, Phys. Rev. B **71**, 125130 (2005).

[78] G. Xianlong, M. Polini, B. Tanatar, and M. P. Tosi, Phys. Rev. B **73**, 161103 (2006).

[79] A. Luther and V. J. Emery, Phys. Rev. Lett. **33**, 589 (1974).

[80] Fulde, Peter and Ferrell, Richard A., Phys. Rev. **135**, A550 (1964).

[81] A. Larkin and Y. Ovchinnikov, Zh. Eksp. Teor. Fiz. **47**, 1136 (1964), sov. Phys. JEPT 20, 762 (1965).

[82] G. Xianlong, M. Rizzi, M. Polini, R. Fazio, M. P. Tosi, J. V. L. Campo, and K. Capelle, Phys. Rev. Lett. **98**, 030404 (2007).

[83] K. Rajagopal and F. Wilczek, in *Frontier of Particle Physics* (World Scientific, Singapore, 2002), Chap. 35.

[84] R. Casalbuoni and G. Nardulli, Reviews of Modern Physics **76**, 263 (2004).

[85] K. Yang, in *Pairing in Fermionic Systems: Basic Concepts and Modern Applications*, edited by M. Alford, J. Clark, and A. Sedrakian (World Scienticic, Singapore, 2006), pp. 253–268, cond-mat/0603190.

[86] M. W. Zwierlein, A. Schirotzek, C. H. Schunck, and W. Ketterle, Science **311**, 492 (2006).

[87] G. B. Partridge, W. Li, R. I. Kamar, Y.-a. Liao, and R. G. Hulet, Science **311**, 503 (2006).

[88] M. W. Zwierlein, C. H. Schunck, A. Schirotzek, and W. Ketterle, Nature **442**, 54 (2006).

[89] Y. Shin, M. W. Zwierlein, C. H. Schunck, A. Schirotzek, and W. Ketterle, Phys. Rev. Lett. **97**, 030401 (2006).

[90] G. B. Partridge, W. Li, Y. A. Liao, R. G. Hulet, M. Haque, and H. T. C. Stoof, Phys. Rev. Lett. **97**, 190407 (2006).

[91] T. Pruschke and H. Shiba, Phys. Rev. B **46**, 356 (1992).

[92] K. Yang, Phys. Rev. B **63**, 140511 (2001).

[93] K. Yang, Phys. Rev. Lett. **95**, 218903 (2005).

[94] C. C. Abilio, P. Butaud, T. Fournier, B. Pannetier, J. Vidal, S. Tedesco, and B. Dalzotto, Phys. Rev. Lett. **83**, 5102 (1999).

[95] E. Serret, P. Butaud, and B. Pannetier, Europhysics Letters (EPL) **59**, 225 (2002).

[96] M. Tesei, R. Théron, and P. Martinoli, Physica C **437**, 328 (2006).

[97] S. E. Korshunov, Phys. Rev. B **63**, 134503 (2001).

[98] V. Cataudella and R. Fazio, Europhysics Letters (EPL) **61**, 341 (2003).

[99] S. E. Korshunov and B. Doucot, Phys. Rev. Lett. **93**, 097003 (2004).

[100] M. Rizzi, V. Cataudella, and R. Fazio, Phys. Rev. B **73**, 144511 (2006).

[101] I. V. Protopopov and M. V. Feigel'man, Phys. Rev. B **70**, 184519 (2004).

[102] I. V. Protopopov and M. V. Feigel'man, Phys. Rev. B **74**, 064516 (2006).

[103] D. Bercioux, M. Governale, V. Cataudella, and V. M. Ramaglia, Phys. Rev. Lett. **93**, 056802 (2004).

[104] D. Bercioux, M. Governale, V. Cataudella, and V. M. Ramaglia, Phys. Rev. B **72**, 075305 (2005).

[105] M. Rizzi, V. Cataudella, and R. Fazio, Phys. Rev. B **73**, 100502 (2006).

[106] L. Jacobs, J. V. José, M. A. Novotny, and A. M. Goldman, Phys. Rev. B **38**, 4562 (1988).

[107] M. Wallin, E. S. So/rensen, S. M. Girvin, and A. P. Young, Phys. Rev. B **49**, 12115 (1994).

[108] T. Ohta and D. Jasnow, Phys. Rev. B **20**, 139 (1979).

[109] H. Weber and P. Minnhagen, Phys. Rev. B **37**, 5986 (1988).

[110] P. Olsson, Phys. Rev. B **55**, 3585 (1997).

[111] B. Sutherland, Phys. Rev. B **34**, 5208 (1986).

[112] D. S. Rokhsar and B. G. Kotliar, Phys. Rev. B **44**, 10328 (1991).

[113] J. K. Freericks and H. Monien, Phys. Rev. B **53**, 2691 (1996).

[114] M. Niemeyer, J. K. Freericks, and H. Monien, Phys. Rev. B **60**, 2357 (1999).

[115] B. J. Kim, G. S. Jeon, M.-S. Choi, and M. Y. Choi, Phys. Rev. B **58**, 14524 (1998).

[116] P. Buonsante, V. Penna, and A. Vezzani, Phys. Rev. B **70**, 184520 (2004).

[117] C. K. Law, H. Pu, and N. P. Bigelow, Phys. Rev. Lett. **81**, 5257 (1998).

[118] T. Ohmi and K. Machida, J. Phys. Soc. Jap. **67**, 1822 (1998).

[119] T.-L. Ho, Phys. Rev. Lett. **81**, 742 (1998).

[120] Y. Castin and C. Herzog, in *Lecture Notes of the Cargese School on Bose-Einstein condensates (2000), tome 2, serie IV* (Comptes Rendus de l'Academie des Sciences de Paris, France, 2000), pp. 419–443.

[121] T.-L. Ho and S. K. Yip, Phys. Rev. Lett. **84**, 4031 (2000).

[122] W. V. Liu and X. G. Wen, cond-mat/0201187 (2002).

[123] E. Demler and F. Zhou, Phys. Rev. Lett. **88**, 163001 (2002).

[124] S. K. Yip, Phys. Rev. Lett. **90**, 250402 (2003).

[125] A. Imambekov, M. Lukin, and E. Demler, Phys. Rev. A **68**, 063602 (2003).

[126] F. Zhou and M. Snoek, Ann. Phys. **308**, 692 (2003).

[127] L.-M. Duan, E. Demler, and M. D. Lukin, Phys. Rev. Lett. **91**, 090402 (2003).

[128] A. A. Svidzinsky and S. T. Chui, Phys. Rev. A **68**, 043612 (2003).

[129] A. Imambekov, M. Lukin, and E. Demler, Phys. Rev. Lett. **93**, 120405 (2004).

[130] M. Snoek and F. Zhou, Phys. Rev. B **69**, 094410 (2004).

[131] A. V. Chubukov, Phys. Rev. B **43**, 3337 (1991).

[132] Y. Xian, J. Phys.: Cond. Mat. **5**, 7489 (1993).

[133] G. Fáth and J. Sólyom, Phys. Rev. B **51**, 3620 (1995).

[134] N. Kawashima, Progress of Theoretical Physics Supplement **145**, 138 (2002).

[135] S. Tsuchiya, S. Kurihara, and T. Kimura, Phys. Rev. A **70**, 043628 (2004).

[136] D. Porras, F. Verstraete, and J. I. Cirac, Phys. Rev. B **73**, 014410 (2006).

[137] A. Lauchli, G. Schmid, and S. Trebst, Phys. Rev. B **74**, 144426 (2006).

[138] J. J. Garcia-Ripoll, M. A. Martin-Delgado, and J. I. Cirac, Phys. Rev. Lett. **93**, 250405 (2004).

[139] M. Rizzi, D. Rossini, G. D. Chiara, S. Montangero, and R. Fazio, Phys. Rev. Lett. **95**, 240404 (2005).

[140] D. Rossini, M. Rizzi, G. D. Chiara, S. Montangero, and R. Fazio, J. Phys. B **39**, S163 (2006).

[141] T. D. Kühner, S. R. White, and H. Monien, Phys. Rev. B **61**, 12474 (2000).

[142] T. D. Kühner and H. Monien, Phys. Rev. B **58**, R14741 (1998).

[143] K. Buchta, G. Fath, O. Legeza, and J. Solyom, Phys. Rev. B **72**, 054433 (2005).

[144] F. D. M. Haldane, Phys. Rev. Lett. **47**, 1840 (1981).

[145] G. Giuliani and G. Vignale, *Quantum Theory of the Electron Liquid* (Cambridge University Press, Cambridge UK, 2005).

[146] I. V. Tokatly, Phys. Rev. Lett. **93**, 090405 (2004).

[147] J. N. Fuchs, A. Recati, and W. Zwerger, Phys. Rev. Lett. **93**, 090408 (2004).

[148] A. Recati, J. N. Fuchs, and W. Zwerger, Phys. Rev. A **71**, 033630 (2005).

[149] R. Citro and E. Orignac, Phys. Rev. Lett. **95**, 130402 (2005).

[150] A. Seidel and D.-H. Lee, Phys. Rev. Lett. **93**, 046401 (2004).

[151] A. Seidel and D.-H. Lee, Phys. Rev. B **71**, 045113 (2005).

[152] G. G. Batrouni, V. Rousseau, R. T. Scalettar, M. Rigol, A. Muramatsu, P. J. H. Denteneer, and M. Troyer, Phys. Rev. Lett. **89**, 117203 (2002).

[153] M. Rigol, A. Muramatsu, G. G. Batrouni, and R. T. Scalettar, Phys. Rev. Lett. **91**, 130403 (2003).

[154] M. Rigol and A. Muramatsu, Phys. Rev. A **69**, 053612 (2004).

[155] X.-J. Liu, P. D. Drummond, and H. Hu, Phys. Rev. Lett. **94**, 136406 (2005).

[156] F. Marsiglio, Phys. Rev. B **55**, 575 (1997).

[157] K. Damle, T. Senthil, S. N. Majumdar, and S. Sachdev, Europhysics Letters (EPL) **36**, 7 (1996).

[158] C. Chin, M. Bartenstein, A. Altmeyer, S. Riedl, S. Jochim, J. H. Denschlag, and R. Grimm, Science **305**, 1128 (2004).

[159] J. Kinnunen, M. Rodríguez, and P. Törmä, Science **305**, 1131 (2004).

[160] R. Combescot, Europhysics Letters (EPL) **55**, 150 (2001).

[161] P. F. Bedaque, H. Caldas, and G. Rupak, Phys. Rev. Lett. **91**, 247002 (2003).

[162] H. Caldas, Phys. Rev. A **69**, 063602 (2004).

[163] M. M. Forbes, E. Gubankova, W. V. Liu, and F. Wilczek, Phys. Rev. Lett. **94**, 017001 (2005).

[164] T. Mizushima, K. Machida, and M. Ichioka, Phys. Rev. Lett. **94**, 060404 (2005).

[165] J. Carlson and S. Reddy, Phys. Rev. Lett. **95**, 060401 (2005).

[166] D. E. Sheehy and L. Radzihovsky, Phys. Rev. Lett. **96**, 060401 (2006).

[167] J. Kinnunen, L. M. Jensen, and P. Torma, Phys. Rev. Lett. **96**, 110403 (2006).

[168] C.-C. Chien, Q. Chen, Y. He, and K. Levin, Phys. Rev. Lett. **97**, 090402 (2006).

[169] K. Machida, T. Mizushima, and M. Ichioka, Phys. Rev. Lett. **97**, 120407 (2006).

[170] T. N. D. Silva and E. J. Mueller, Phys. Rev. Lett. **97**, 070402 (2006).

[171] M. Rizzi, M. Polini, M. R. Bakhtiari, R. Fazio, and M. Tosi, , in preparation.

[172] S. Abedinpour, M. R. Bakhtiari, G. Xianlong, M. Polini, M. Rizzi, and M. Tosi, Laser Physics **17**, 162 (2007).

[173] W. V. Liu and F. Wilczek, Phys. Rev. Lett. **90**, 047002 (2003).

[174] H. Caldas, cond-mat/0605005 (2006).

[175] H. Caldas, cond-mat/0601148 (2006).

[176] K. Yang and D. F. Agterberg, Phys. Rev. Lett. **84**, 4970 (2000).

[177] M. Houzet, A. Buzdin, L. Bulaevskii, and M. Maley, Phys. Rev. Lett. **88**, 227001 (2002).

[178] V. Barzykin and L. P. Gor'kov, Phys. Rev. Lett. **89**, 227002 (2002).

[179] L. Bulaevskii, A. Buzdin, and M. Maley, Phys. Rev. Lett. **90**, 067003 (2003).

[180] K. Yang and A. H. MacDonald, Phys. Rev. B **70**, 094512 (2004).

[181] G. Orso, Phys. Rev. Lett. **98**, 070402 (2007).

[182] H. Hu, X.-J. Liu, and P. D. Drummond, Phys. Rev. Lett. **98**, 070403 (2007).

[183] L.-M. Duan, Phys. Rev. Lett. **96**, 103201 (2006).

[184] F. K. Pour, M. Rigol, S. Wessel, and A. Muramatsu, Phys. Rev. B **75**, 161104 (2007).

[185] S. L. Cornish, N. R. Claussen, J. L. Roberts, E. A. Cornell, and C. E. Wieman, Phys. Rev. Lett. **85**, 1795 (2000).

[186] S. Inouye, J. Goldwin, M. L. Olsen, C. Ticknor, J. L. Bohn, and D. S. Jin, Phys. Rev. Lett. **93**, 183201 (2004).

[187] F. Ferlaino, C. D'Errico, G. Roati, M. Zaccanti, M. Inguscio, G. Modugno, and A. Simoni, Phys. Rev. A **73**, 040702 (2006).

[188] C. A. Stan, M. W. Zwierlein, C. H. Schunck, S. M. F. Raupach, and W. Ketterle, Phys. Rev. Lett. **93**, 143001 (2004).

[189] B. DeMarco and D. S. Jin, Science **285**, 1703 (1999).

[190] F. Schreck, L. Khaykovich, K. L. Corwin, G. Ferrari, T. Bourdel, J. Cubizolles, and C. Salomon, Phys. Rev. Lett. **87**, 080403 (2001).

[191] G. Modugno, G. Roati, F. Riboli, F. Ferlaino, R. J. Brecha, and M. Inguscio, Science **297**, 2240 (2002).

[192] Z. Hadzibabic, C. A. Stan, K. Dieckmann, S. Gupta, M. W. Zwierlein, A. Görlitz, and W. Ketterle, Phys. Rev. Lett. **88**, 160401 (2002).

[193] J. Goldwin, S. Inouye, M. L. Olsen, B. Newman, B. D. DePaola, and D. S. Jin, Phys. Rev. A **70**, 021601 (2004).

[194] K. K. Das, Phys. Rev. Lett. **90**, 170403 (2003).

[195] M. A. Cazalilla and A. F. Ho, Phys. Rev. Lett. **91**, 150403 (2003).

[196] L. Mathey, D.-W. Wang, W. Hofstetter, M. D. Lukin, and E. Demler, Phys. Rev. Lett. **93**, 120404 (2004).

[197] L. Mathey and D.-W. Wang, Phys. Rev. A **75**, 013612 (2007).

[198] L. Mathey, Phys. Rev. B **75**, 144510 (2007).

[199] A. Imambekov and E. Demler, Ann. Phys. **321**, 2390 (2006).

[200] A. Imambekov and E. Demler, Phys. Rev. A **73**, 021602 (2006).

[201] M. T. Batchelor, M. Bortz, X. W. Guan, and N. Oelkers, Phys. Rev. A **72**, 061603 (2005).

[202] H. Frahm and G. Palacios, Phys. Rev. A **72**, 061604 (2005).

[203] Y. Takeuchi and H. Mori, Int. Jour. Mod. Phys. B **20**, 617 (2006).

[204] Y. Takeuchi and H. Mori, J. Phys. Soc. Jap. **74**, 3391 (2005).

[205] Y. Takeuchi and H. Mori, Phys. Rev. A **72**, 063617 (2005).

[206] P. Sengupta and L. P. Pryadko, Phys. Rev. B **75**, 132507 (2007).

[207] L. Pollet, M. Troyer, K. V. Houcke, and S. M. A. Rombouts, Phys. Rev. Lett. **96**, 190402 (2006).

[208] L. Pollet, C. Kollath, U. Schollwoeck, and M. Troyer, cond-mat/0609604 (2006).

[209] K. Günter, T. Stöferle, H. Moritz, M. Köhl, and T. Esslinger, Phys. Rev. Lett. **96**, 180402 (2006).

[210] S. Ospelkaus, C. Ospelkaus, O. Wille, M. Succo, P. Ernst, K. Sengstock, and K. Bongs, Phys. Rev. Lett. **96**, 180403 (2006).

[211] D. B. M. Dickerscheid, D. van Oosten, E. J. Tillema, and H. T. C. Stoof, Phys. Rev. Lett. **94**, 230404 (2005).

[212] E. H. Lieb and W. Liniger, Phys. Rev. **130**, 1605 (1963).

[213] M. A. Cazalilla, Phys. Rev. A **67**, 053606 (2003).

[214] B. Schmidt, L. I. Plimak, and M. Fleischhauer, Phys. Rev. A **71**, 041601 (2005).

[215] M. A. Cazalilla, J. Phys. B **37**, S1 (2004).

[216] D. M. Stamper-Kurn, A. P. Chikkatur, A. Görlitz, S. Inouye, S. Gupta, D. E. Pritchard, and W. Ketterle, Phys. Rev. Lett. **83**, 2876 (1999).

[217] A. Polkovnikov, E. Altman, and E. Demler, Proc. Nat. Acad. Sc. **103**, 6125 (2006).

[218] A. Imambekov, V. Gritsev, and E. Demler, cond-mat/0703766 (2007).

[219] G. Vidal, J. I. Latorre, E. Rico, and A. Kitaev, Phys. Rev. Lett. **90**, 227902 (2003).

[220] K. G. Wilson, Rev. Mod. Phys. **47**, 773 (1975).

[221] A. L. Malvezzi, Brazilian Journal of Physics **33**, 55 (2003).

[222] M.-C. Chung and I. Peschel, Phys. Rev. B **62**, 4191 (2000).

[223] M. A. Cazalilla and J. B. Marston, Phys. Rev. Lett. **88**, 256403 (2002).

[224] A. J. Daley, C. Kollath, U. Schollwöck, and G. Vidal, J. Stat. Mech. **2004**, P04005 (2004).

[225] S. R. White and A. E. Feiguin, Phys. Rev. Lett. **93**, 076401 (2004).

[226] U. Schollwoeck, J. Phys. Soc. Jap. **53**, 2452 (1984).

[227] S. R. White, Phys. Rev. Lett. **77**, 3633 (1996).

[228] http://www-03.ibm.com/servers/eserver/bladecenter/.